UiT The Arctic University of Norway

Faculty of Science and Technology
Department of Geosciences

An investigation into the causal factors of the Kråknes landslide

Torgrim Sandnes
Master's thesis in Geology (GEO-39100), May 2021

Abstract

On the 3rd of June 2020, a landslide measuring 600 meters long and 160 meters wide initiated along the shoreline at Kråknes, in Alta municipality in Troms and Finnmark County. The landslide was comprised of a series of smaller slides, which destroyed eight houses and a caravan in the process. Fortunately, no human lives were lost in the event. Due to the widespread presence of sensitive clays along the Norwegian coast, numerous areas are at the potential risk of landslides. As these landslides pose a risk to human life and infrastructure, a better understanding of what promotes instability and triggers these types of landslides is necessary.

The goal of this thesis is to determine the causal factors responsible for the slope failure at Kråknes. To do this, hydrometeorology, ground conditions and human activity were analyzed in combination with slope stability modeling. The array of data used in this thesis comprises meteorological reports and models, field observations, unmanned aerial vehicle surveys, LiDAR- and bathymetry data, and a consultant geotechnical survey. The results indicate that the initial stability at Kråknes was low. Signs of quick- and sensitive clay were observed during fieldwork, and were also detected during the geotechnical survey. The layered stratigraphy of the ground conditions, with permeable- and non-permeable layers are interpreted to have intensified the leaching process of the marine clay and promoted the development of excess pore pressure. With the added load of the cabin building in 2015, it is suspected that the average stability at Kråknes was lowered enough to be triggered by an abrupt snowmelt event in the second half of May. As a result, the formation of a tension crack on the 2nd of June is interpreted to be the initiation of a progressive flake-type failure that spread north overnight to where the slide initiated below Kråknesveien 416 on the 3rd of June. The slope stability modeling supported the expected negative effects higher groundwater levels, excess pore pressure and external loading from the cabin building might have had. However, some model results regarding the dimension of the failure surface and factor of safety did not reflect reality.

Acknowledgments

This thesis marks the final work of my Masters of Science (M.Sc.) in Geology at the Department of Geosciences at The Arctic University of Norway (UiT), and hence, a final end to my long-lasting occupation as a student.

Firstly, I would like to thank my supervisor Louise Mary Vick (UiT), for guiding me through this process during the last year. Thank you for all the valuable feedback you have given me, and for always taking the time to answer my many emails. I would also like to thank my co-student, Stina Mari Pettersen, for the week of fieldwork we had together. Who would have known that mosquito repellant would be such a vital tool for our work.

A thanks must be given to all my fellow master students with whom I have shared this last year with. Thank you for two fantastic years in Tromsø! A special thanks must be given to Sondre and Johan for all the skiing, coffee and good times we have had over the last two years, it will be missed.

I would also like to show my gratitude to my girlfriend Kjersti, for proofreading and supporting me through this last year. Finally, I would like to thank my mother and father for supporting me through my education. This would not have been possible without you. A special thanks to my mother for spending countless hours helping me with homework during my younger years, your efforts will never be forgotten.

Tromsø, May 2021

Torgrim Sandnes

Table of Contents

1 Introduction

The widespread presence of marine- and glaciomarine sediments in Norway predisposes numerous areas to the risk of landslides, especially concerning sensitive clays (Eilertsen et al., 2008). Landslides in sensitive clay can happen with little or no warning and can have detrimental consequences to human life- and infrastructure (Wiig et al., 2019). Sensitive clay landslides, often referred to as quick clay landslides, have been recorded as early as the year 1254 in Norway, although most have transpired during the last 150 years. The largest and most destructive of these landslides are Verdal (1893), Sokkelvik (1959), and Rissa (1978) (NGI, 2021). Increasing urbanization in landslide-prone areas requires a better understanding of the processes involved, especially regarding slope stability and the timing of future events. As a result, the Norwegian Geotechnical Institute (NGI) instituted a nationwide project after the Rissa landslide in 1978, mapping zones of potential sensitive clay (Høydal & Haugland, 2011). Since then, sensitive clay has been identified at multiple localites over the whole country, although it is predominately concentrated in Østfold, Trøndelag and parts of northern Norway.

For northern Norway, and in particular Alta, the last regional quick clay mapping survey took place in 2009 and 2010. The survey report covered 46 zones, of which nine were interpreted as high risk (Høydal & Haugland, 2011). Despite the report being thorough for the areas included, large parts of the Alta region are still unmapped today, increasing the risk of quick clay related disasters. Unfortunately, this was manifested at Kråknes, on the 3rd of June, 2020 (Figure 1).
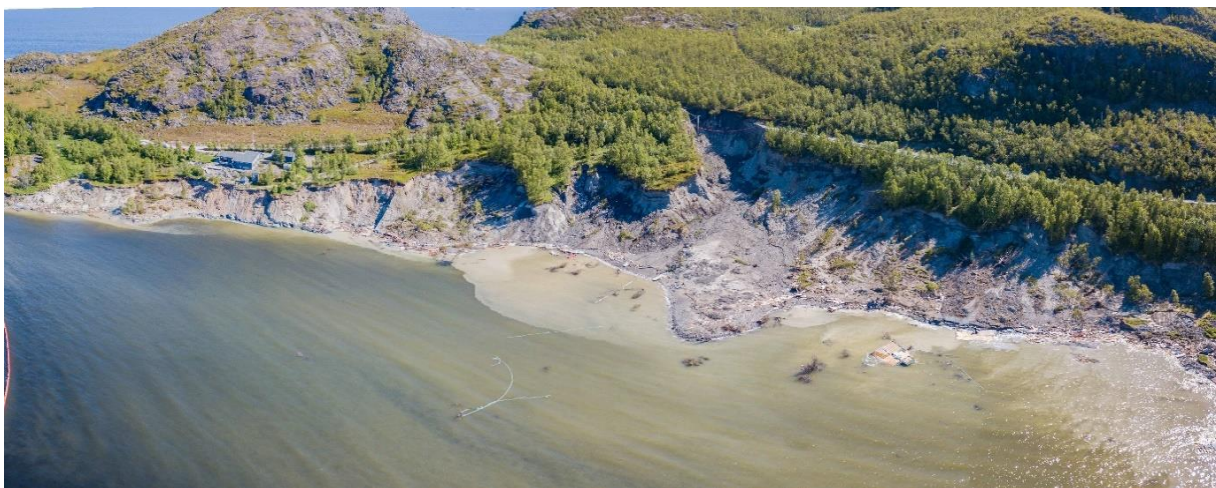

Figure 1: Photo of the Kråknes landslide, looking towards the north (Photo: Raymond Eilertsen 03.06.2020).

The Kråknes landslide was a shoreline landslide that consisted of series of destructive soil slope failures which occurred at the Kråknes beach, near Alta, Norway. The slide was approximately 650 meters long and 160 meters wide, destroying eight houses and a caravan in the process. The main slide event transpired between June 3rd and 6th 2020, although reports from locals indicate sliding activity commenced on the 29th of May (Regobs, 2020). No human lives were lost in the landslide, despite a high potential for human casualties, had it occurred during a time of higher occupancy.

Immediately after the events, a task force was formed to investigate the event. As part of this work, ground investigations were carried out by Multiconsult and NVE in the days following the event. The data from their investigation, combined with original work from this thesis, provided an excellent basis for an in-depth study of the conditions that lead to slope failure on June 3rd.

1.1 Objectives of the study

The principal objective for this Master thesis has been to link hydrometeorology, ground conditions and human activities together to determine the causal factors for the landslide. In doing so, this thesis will analyze geotechnical-, and meteorological data in combination with slope stability modeling to determine what caused the slope to fail. As such, the main research questions addressed are:

- Can failure be linked to a specific hydrometeorological event preceding the slope failure?
- How have the ground conditions at Kråknes facilitated instability?
- Can human activity be linked to the destabilization of the slope?

The tasks undertaken to address the research questions are:

- Compile and analyze meteorological- and hydrological data preceding the slope failure.
- Analyze and interpret field observations and geotechnical- and spatial data to establish destabilizing factors linked to the slope failure.

- Compile evidence of human activity possibly connected to the destabilization of the slope.
- Back analysis of instability-promoting factors through the use of a simplistic model

1.2 Available data

The results presented in this thesis are based on data collected by the author and concurrent master student Stina Mari Pettersen from The Arctic University of Norway (UiT), during one week of fieldwork in the summer of 2020. In addition, Light Detection and Radar (LiDAR) data, swath bathymetry and preliminary reports were made available by NVE. A summary of the external spatial data sources is listed in Table 1.

Table 1: Overview of external spatial data sources employed in this thesis.

DATA	SOURCE	RESOLUTION
Digital elevation model	*Kartverket*	1 m
Orthophoto imagery (2015 and 2018)	*Kartverket*	0.1 m
Bathymetry (2004)	*NVE*	1 m
Bathymetry (1998)	*NVE*	5 m
LiDAR (2018)	*NVE*	1 m
LiDAR (2020)	*NVE*	1 m
Quarternary map	*NGU (Riiber, 2000)*	1:250 000
InSAR displacement data	*NGU (https://insar.ngu.no)*	
UAV data	*Anders Bjordal (NVE)*	

1.3 Setting of the study area

Kråknes is located on the western end of the Kråkneset peninsula, in Troms and Finnmark County, northern Norway (Figure 2A). The peninsula is situated on the western flank of Altafjorden, a small fjord system stretching 35 km from north to south (Figure 2B). The region is characterized by an alpine topography formed by multiple glaciations (Vorren & Mangerud, 2007). On the peninsula, a small mountain ridge trends north to south, with gentle sloping mountains reaching elevations close to 400 masl. Kråknes is located along the shoreline and is characterized by northwest-facing slope, with an average slope angle of 10° (Figure 2C). The area exhibits a lower mean elevation than its surroundings, as well as abundant vegetation and soft-sediment deposits (Figure 2C). With its arctic location and proximity to the ocean, Kråknes experiences a unique climate, which will be explained in more detail in the following section.
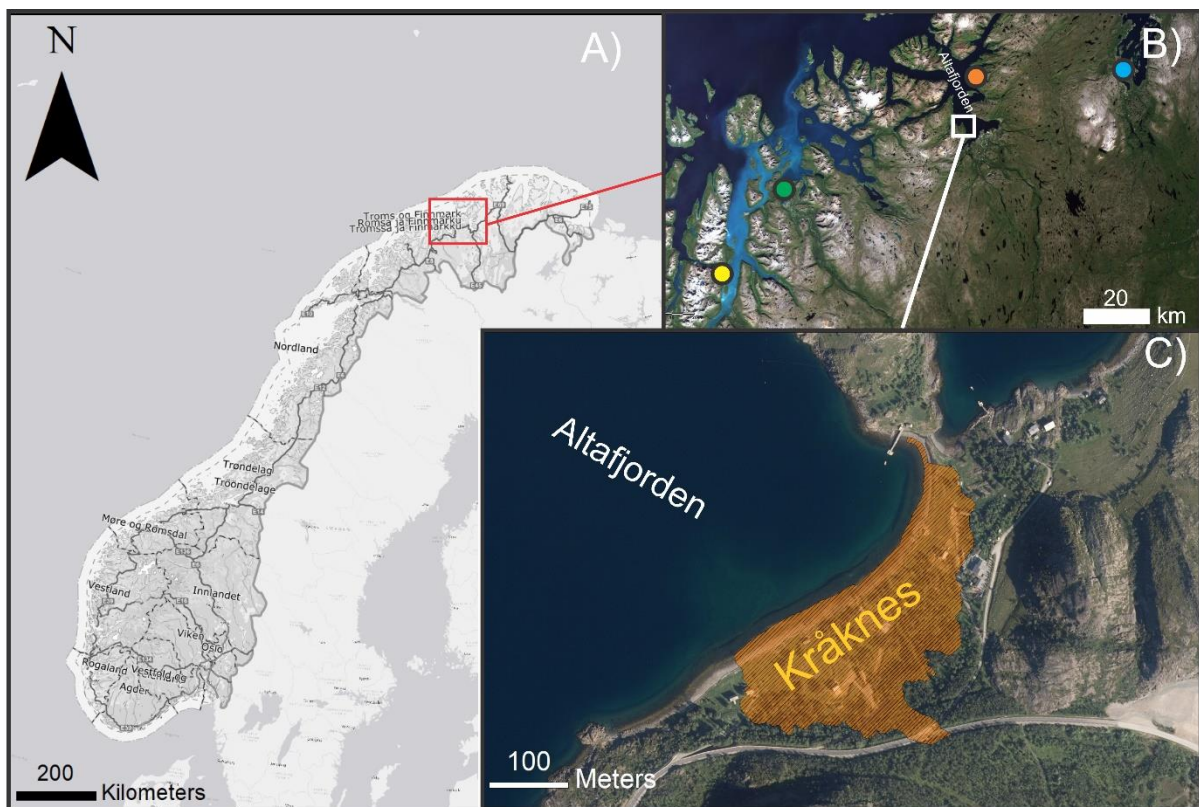
Figure 2: Overview and detailed maps of the study area. A) Topographic overview map of Norway with the location of the study area (red) (Kartverket, 2020). B) Medium-scale map: Aerial photo of the surrounding area and studied sites. The ellipses mark the Lakselv monitoring station (blue), Store Lerresfjord (orange), Sokkelvik (green), Lyngseidet (yellow) and Kråknes (white), adapted from: Norgeibilder.no. C) Aerial photo of the study area, the red color illustrates the area affected by the slope failure (Kartverket, 2018).

4

1.3.1 Climate

Situated at 70 °N, Kråknes experiences a cold temperate climate, with short cool and summers (average temperature July 13.4 °C) and long cold winters (Aune, 1993; Mamen, 2020). The proximity to open water creates a more humid coastal climate, although coastal regions in northern Norway generally are less humid than further south (Meteorologisk Institutt, 2020). Meteorological data from 1971-2000 shows a mean annual temperature of 1.6 °C and precipitation of 390 mm/yr for the weather station at Alta, 10 km SE of Kråknes (Norsk Klimserviceasenter, 2016). Annual rainfall and temperature records show an upward trend over time for the region (Figure 3).
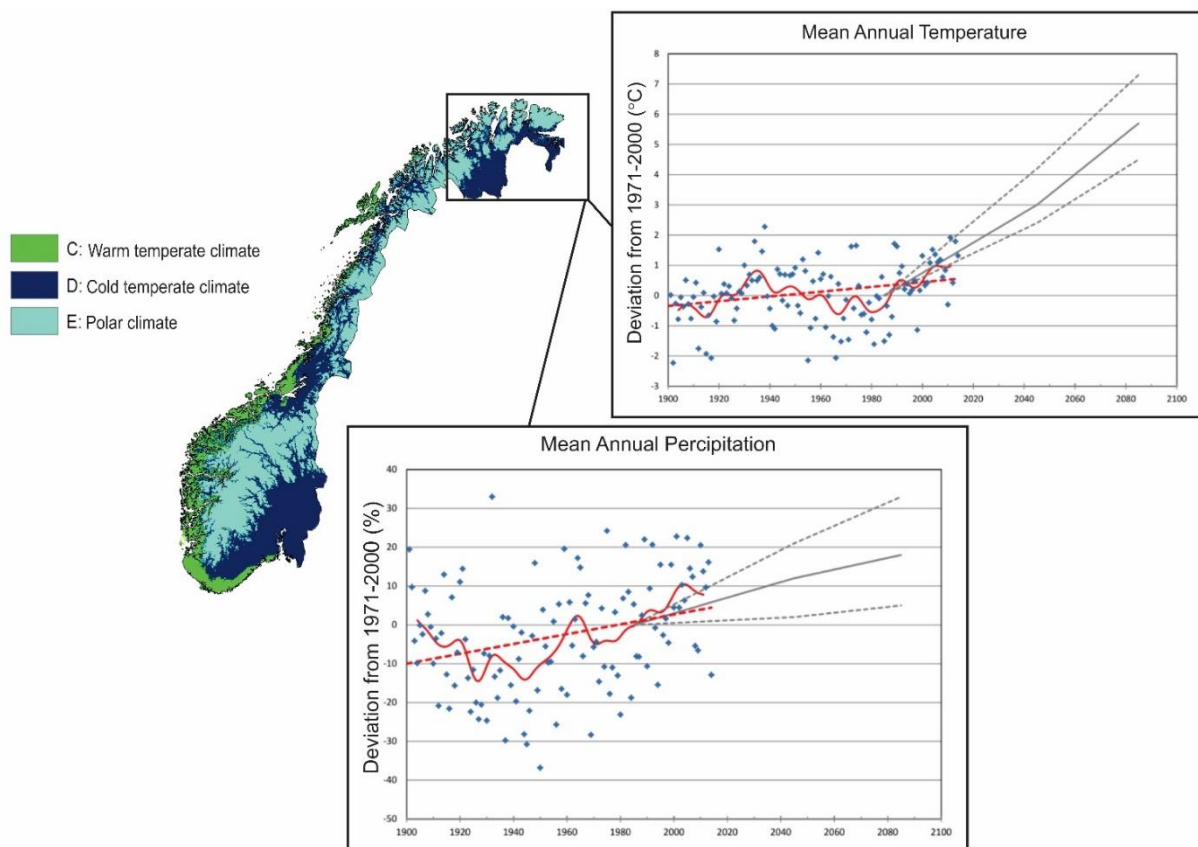
Figure 3: Map of Norway with affiliated climate zones. The two graphs illustrate the mean annual temperature and precipitation calculated from the average values between 1971-2000 for Troms and Finnmark. Blue dots represent the observed single-year anomalies in the period 1900-2014. The red dotted line is the observed trend of the dataset, while the solid red line is the smoothed 10-year variation. The solid and dotted grey line is the modeled development for the future, with medium, high, and low greenhouse gas emissions. Adapted from (Norsk Klimserviceasenter, 2016; Mamen, 2020).

1.3.2 Bedrock geology

The bedrock on the west coast of Finnmark is affected by several sets of faults and tectonic lineaments (Figure 4A) (Bergh et al., 2007). ENE-WSW- and NNE-SSW- striking faults are common in the region, where they create fault complexes with distinguished zigzag patterns. For Kråknes, the bedrock geology is presented a digitalized in a 1:250 000 digitalized map based on Roberts (1973) and Zwaan (1988), and is currently the highest resolution available (Figure 4B). According to the map, the study area is primarily composed of greenstone and metagabbro with smaller shale and limestone layers (Roberts, 1973; KB Zwaan, 1988). The bedrock belongs to the Raipais Group and is a part of the Alta-Kvænangen tectonic window, forming the northern part of the Baltic Shield (Bergh & Torske, 1988). Basement rocks in the Alta-Kvænangen tectonic window are affected by large-scale NW-plunging folds (Koehl et al., 2019; Zwaan & Gautier, 1980). After the landslide, the bedrock was mapped on a more local scale by LiDAR (Figure 4C). Results showed that the bedrock had bedding oriented NNW-SSE, dipping 60° WSW and faults striking ENE-WSW (Indrevær, 2020).
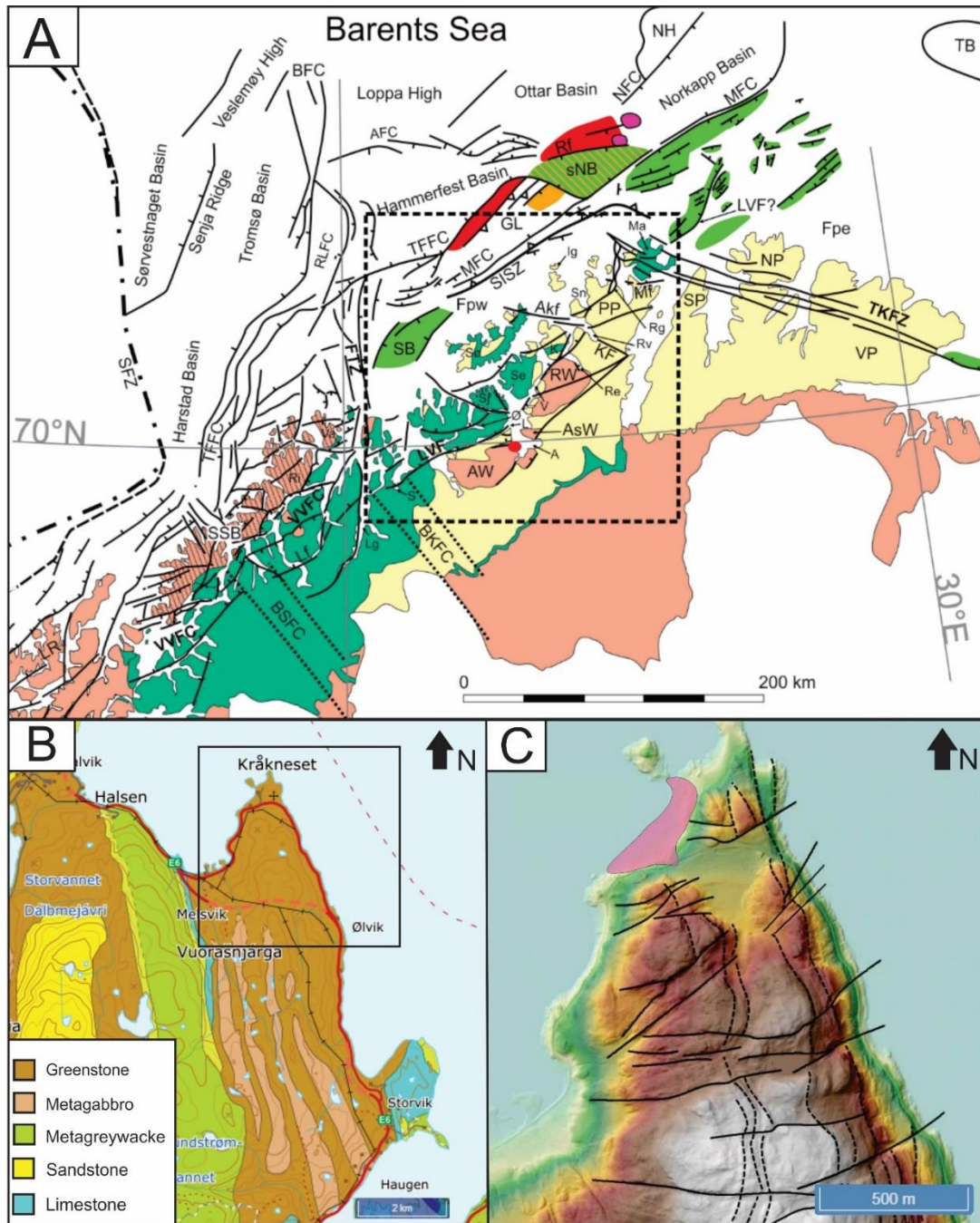
Figure 4:A) Regional tectonic map of Northern Norway and the Barents Sea. Black lines illustrate fault complexes. Abbreviations: A- Altafjorden, AsW –Altenes tectonic window, AW – Alta-Kvænange tectonic window. The red dot illustrates the location of Kråknes. Adapted from (Koehl et al., 2019) B) 1:250 000 bedrock map of Kråknes and the surrounding area. Adapted from (NGU,2020). C) Lidar data from Kråknes and the surrounding area. Stapled lines are interpreted as bedrock boundaries, and continuous lines are interpreted as faults. The area affected by the landslide is illustrated in red. Adapted from (Indrevær, 2020).

1.3.3 Quarternary geology

The Quaternary geological setting is crucial for understanding and interpreting the circumstances that lead to the slope failure at Kråknes. As a resource, Quaternary geology maps and previous studies are particularly valuable. Prior to the slope failure, little work regarding the Quarternary geology of the study area had been produced. Large-scale maps are available but involve great uncertainty as they are based on aerial photography and roadside observations. As an example, the Quaternary map of Kråknes only includes thin beach sediment and exposed bedrock, with relatively crude boundaries (Figure 5A). Due to the scale and uncertainty of the previous mapping, a new map was produced by the Geological Survey of Norway after the event (Figure 5B). This map is based on morphological interpretations from a high-resolution terrain model (LiDAR) and fieldwork (Hansen, 2020). Due to the scope of this thesis, an in-depth sedimentary analysis has not been undertaken for Kråknes. As a result, the quaternary map and interpretations by Hansen (2020), have been valuable. From the map, it can be observed that the deposits at Kråknes mainly consist of thick- and thin beach sediment, with the addition of till in the neighboring Kråkvikdalen (Figure 5B). Structures interpreted as raised beaches have been mapped at several localities across the study area, indicating processes connected to crustal uplift. Furthermore, the boundary for the marine limit (ML) has been estimated at 70 masl., marking the high point of the oceanic advance during the Quaternary glaciations (Eronen et al., 2001). To better understand the sediments deposited at Kråknes, it is necessary to examine the processes that created them.
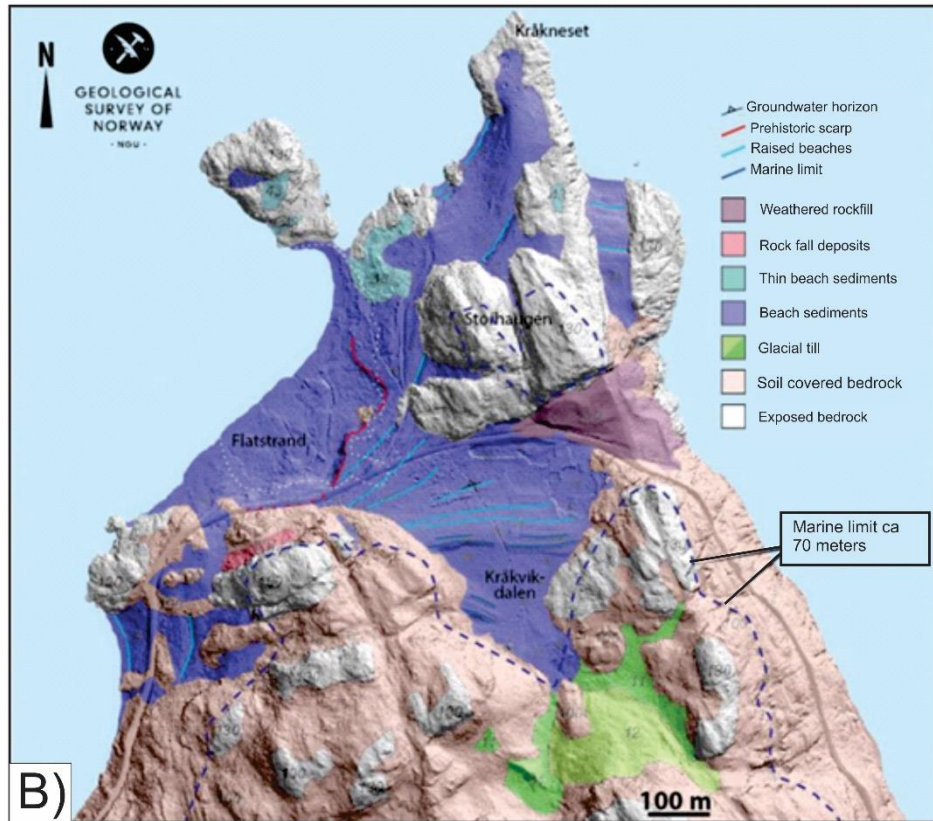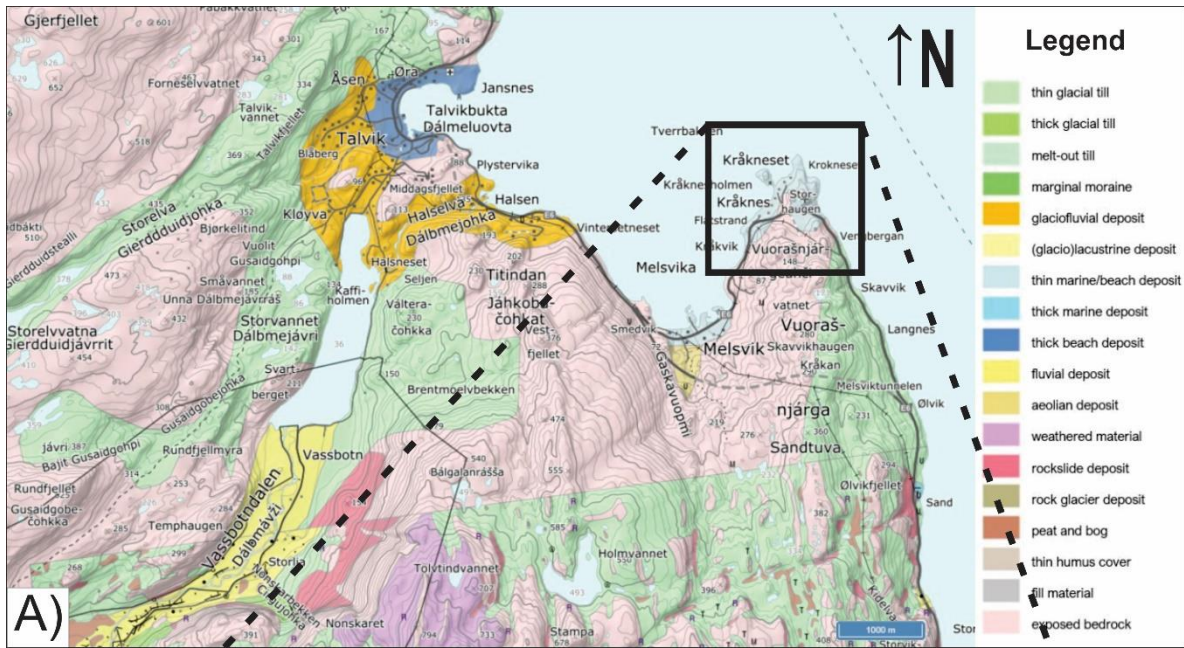
Figure 5:A) 1:250 000 map of the quaternary deposits surrounding Kråknes (NGU, 2020c). B) Quarternary geology map produced by NVE following the slope failure at Kråknes (Hansen, 2020).

1.3.4 Glaciation and deglaciation of northern Norway

The Quaternary period defines the last 2.5 million years of the Earth's history. During this time, dramatic climate changes caused glaciers to expand and retreat, influencing the Eurasian continent. In response to the advancing and retreating glaciers, sea level periodically rose and fell, exposing new land in the process (Andersen & Borns, 1994; Fredin et al., 2013). Over the last million years, 40 glacial cycles have carved and polished the continent (Fredin et al., 2013). Various names have been used to describe the complex ice sheets and glacial cycles that have transpired during this time, although most of the features and depositional landforms observed in Norway today are originate from the most recent Weichselian glaciation.

Depositional landforms such as moraines and till deposits have given us the maximum extent of the Eurasian ice sheet for the last 40 ka. This ultimate extent is often referred to as the Last Glacial Maximum (LGM). The LGM timing varies geographically, although the period has been confined to 23-21 ka (Böse et al., 2012; Hughes et al., 2016). At this time, the Fennoscandian- and Barents Sea ice sheet coalesced outside the coast of Finnmark, while the inland was entirely covered by ice (Romundset et al., 2011).

After the LGM, the ice margin started to retreat, and the coast of Finnmark became ice-free around 14.6 ka, although some studies suggest it happened as early as 18 ka in places (Romundset et al., 2011; Hughes et al., 2016; Patton et al., 2017). In general, this period was influenced by a large retreat of the ice margin, despite a cold period during the Older Dryas, resulting in a readvance of the ice margin by a few kilometers (Olsen et al., 2013). This is supported by Stokes et al. (2014), who compiled a chronology of the ice margin from eight major outlet glaciers from the Fennoscandian Ice Sheet. The studies show that the retreat was largest from 15 ka to 14 ka, and 14 ka to 13 ka. As an example, Altafjorden was deglaciated 13.5 ka prior to the readvancement of the Older Dryas. Based on these compiled dates, Kråknes became ice-free between 14.2 and 11.4 ka (Figure 6B) (Stokes et al., 2014). However, Romundset et al. (2011) suggest that the YD end moraine is south of Kråknes, indicating that the readvance did not reach this area (Figure 6C). Regardless, the ice retreated from Kråknes sometime near the end of Younger Dryas, or the start of the Preboreal (Stokes et al., 2014).
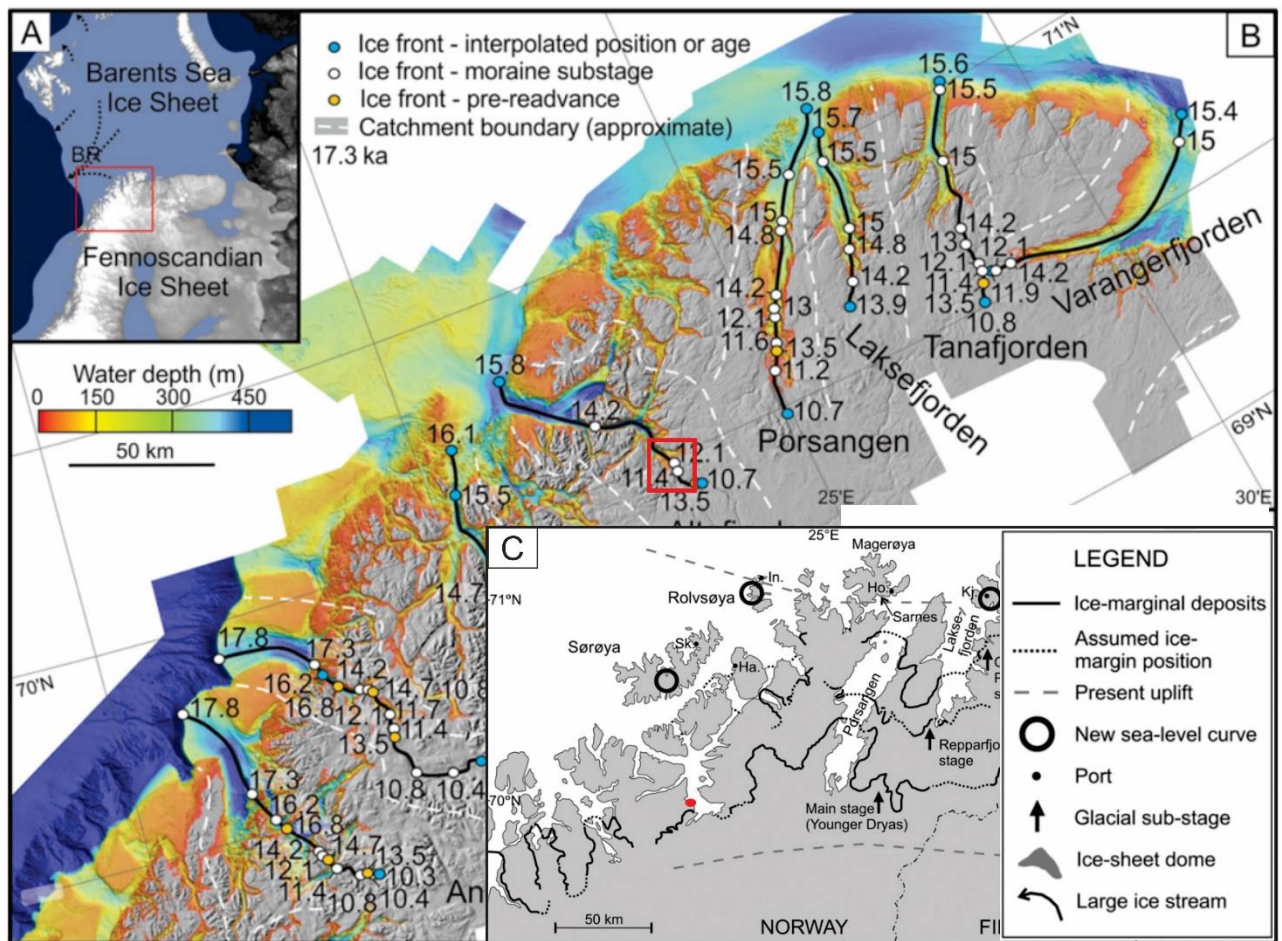
Figure 6: A) Map of the Fennoscandian Ice Sheet at LGM, showing the position of Troms and Finnmark (red box). B) Topography map illustrating the ice margin chronology for eight fjord systems in Troms and Finnmark. Location of Kråknes illustrated by red box. Adapted from: (Stokes et al., 2014). C) Map of Younger Dryas-, Repparfjord and Outer Porsanger stage, based on mapped and assumed ice-marginal deposits. Kråknes located by red dot (Romundset et al., 2011).

1.3.5 Isostatic uplift

As glaciers started to waste away during the Late Weichselian, their weight was reduced, leading to readjustment in the form of crustal uplift. As the crust rebounded, the forces were split into two components: elastic- and plastic deformation (Jørgensen, 1995). The elastic deformation is more rapid and accounts for the uplift during the first 3000 years. In comparison, the plastic deformation is much slower due to changes in mineral composition and mass movements at greater depth (Jørgensen, 1995). As a result, isostatic uplift continues today with rates up to 9 mm/year in the areas affected by the thickest ice (Eronen et al., 2001). Compared to northern Norway, where the uplift varies between 1-2.5 mm/year from the coast to the inland (Eronen et al., 2001).

11

Generally, the uplift by far surpassed the sea level rise in Norway. Depending on the area, the ML will vary. In Trøndelag and Oslo, the ML exceeds 200 meters, while in Troms and Finnmark, it ranges from 40 to 90 meters depending on the location (Laurits Bjerrum, 1954; Høydal & Haugland, 2011; NVE, 2014). As relative sea levels dropped, marine sediments were uncovered and exposed to the surface environment. The reaction to surface conditions, especially for marine clay, has shown to be detrimental to its stability.

1.4 Previous events in Troms and Finnmark

There are many examples of landslides occurring along the Norwegian shoreline, often with severe consequences. Since much of the shoreline is inhabited, landslides can have a devastating effect on both human life and infrastructure. These types of slides can become especially unpredictable and dangerous when sensitive marine clay is involved (Hansen et al., 2013). For Troms and Finnmark, the Sokkelvik landslide in 1959, Store Lerresfjord in 1975 and Lyngseidet in 2010 are the most destructive landslides of the region. For that reason, a brief description of these landslides will be presented next.

1.4.1 Sokkelvik 1959

On May 7th 1959, a sensitive clay landslide involving more than 1 million m^3 soil was initiated along the shoreline in Sokkelvik (Figure 7A). The slide was a combination of the material above and below the water surface, creating a tsunami in the process. Seventeen of the 29 inhabitants in Sokkelvik were taken by the slide, resulting in nine casualties. Although investigations were carried out following the event, the causes for the landslide were poorly documented at the time (L'Heureux et al., 2017).

A newer study re-investigated the main causes of the slide by implementing swath bathymetry data and numerical analysis software. The study concluded that the slide was likely triggered by heavy rainfall and snowmelt on May 7th, but that the main cause was linked to an embankment fill placed on the shoreline prior to the event (L'Heureux et al., 2017).

1.4.2 Store Lerresfjord 1975

On March 14th 1975, a sensitive clay landslide commenced on a small fishing settlement in Store Lerresfjord (Figure 7B). The slide swept several houses and a pier with it, killing three people in total. A report following the slide concluded that there was no human activity responsible for the slope failure. However, 30-50 mm of rain was measured prior to the event

in addition to a temperature increase following a cold period, suggesting a possible connection. (Sokalska et al., 2015).

1.4.3 Lyngseidet 2010

On September 3rd 2010, a sensitive clay landslide instigated at the shoreline at Lyngseidet (Figure 7C). The initial slide swept away the road, two houses, garages, cars and construction equipment. As the slide continued to evolve, one more house and a couple of cars were taken as well. Luckily, no human lives were lost. The following report, concluded that the area consisted of sensitive- and quick clay, and had likely been triggered by the construction work at the shoreline (Hoseth et al., 2014).

Figure 7: A) Photo of the landslide scar at Sokkelvik in 1959, (Photo: L'Heureux et al., (2017). B) Photo of the fishing settlement that was swept away at Store Lerresfjord in 1975. (Photo: Facsimile from Altaposten, March 15th 1975. Overview photo taken at Lyngseidet shortly after the landslide in 2010 (Photo: Andrea Taurisano/NVE).

2 Theoretical background

2.1 Sensitive clay landslides at the shoreline

The shoreline we observe today is the result of numerous geological processes over time. One of the more unpredictable and spectacular geological processes, are landslides. Shoreline landslides, are landslides that impact both land- and marine settings, making them unique in this area of interest. As with all landslides, the type of shoreline landslide is determined by the geology of the area. For areas involving fine-grained marine-, deltaic and fluvial sediments, shorelines landslides involving sensitive clay is common (Hansen et al., 2013). Continuing forward, literature specific to sensitive clay- and shoreline landslides will be presented.

Sensitive clay, sometimes referred to as brittle clay, is clay that displays a sensitivity (S_t) $\geq$ 15 and remolded shear strength $\leq$ 2.0 kPa (Wiig et al., 2019). In cases where the remolded shear strength is less than 0.5 kPa and sensitivity (S_t) greater than 30, the clay is referred to as "quick clay" (L'Heureux et al., 2017; Statens vegvesen, 2005). Sensitive clays usually stem from fine-grained glaciofluvial sediments that have been deposited in a low-energy marine environment. During deposition, as the clay settles on the seafloor, positive ions cause an attraction between the clay particles, creating a "house of cards"- structure by the flocculation (Figure 8A) (Giles, 2020). The flocculation creates a larger void space than usual, giving rise to higher water content in the clay (Rankka et al., 2004; Giles, 2020). During this early phase, the clay has a stable structure due to the chemistry of the pore water. The natural concentration of salt (sodium chloride) in the pore water is equal to that of the sea (35 g/l) when deposited in a marine environment, subsequently providing a high cationic strength between the particles (Laurits Bjerrum, 1954).
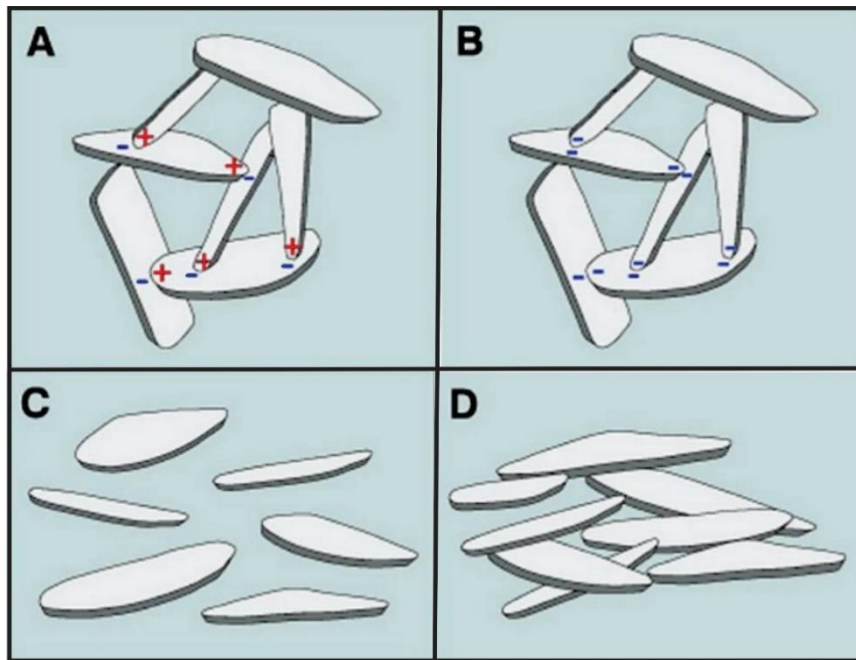
Figure 8: A) Clay with salt-rich porewater. B) Quick clay before failure. C) Quick clay at failure. D) Quick clay after failure. Adapted from (Reite et al., 1999).

As isostatic uplift exposes the marine environment to surface conditions, freshwater starts to percolate through the clay, initiating a leaching process where the salt concentration is reduced to around 1-2 g/l. The resultant loss of chemical bonds has proved to generate highly sensitive clays that can exist in a metastable state (Figure 8B) (Rosenqvist, 1953). The leaching can occur both from the surface through rain, or through groundwater flow within more permeable layers (Rankka et al., 2004; Giles, 2020). As the clay operates in a meta-stable state, landslides can happen with little warning, making them hard to predict in advance. This meta-stable is also expressed through the strain-softening behavior of sensitive clays.

As with any geomaterial, sensitive clays follow a strength and deformation curve when exposed to loading. However, due to the "house of cards" structure of sensitive clay, failure is sudden when loading goes beyond a specific limit, called the peak strength of the clay. Figure 9 shows an idealized graph of the strength-deformation relationship for sensitive clays. Here, the strength of the clay is visualized in its original (in-situ) state at first. Subsequently, if loading or another strength-reducing factor is applied, the clay reaches its peak strength. If loading continues beyond this point, the internal structure of the clay will collapse, resulting in an abrupt loss of strength before reaching its residual strength level (Figure 9) (Skempton, 1964). This behavior is what makes sensitive clay so unpredictable and dangerous in regards to landslides.

15

Areas previously perceived as stable can suddenly fail if the peak strength of the clay is surpassed. Hence, the next section will go into more detail about the main failure mechanims and morphologies associated with sensitive clay landslides along the shoreline.
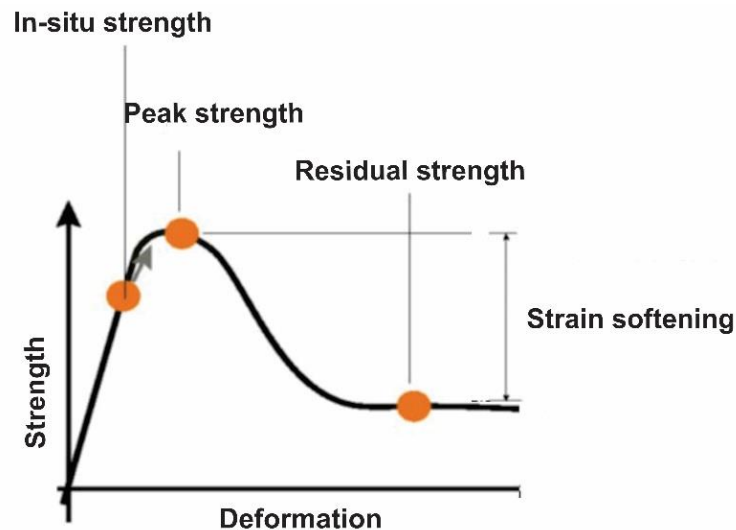

Figure 9: Schematic of an idealized strength-deformation curve for sensitive clay. The graph illustrates how the strength changes from its original (in-situ) strength to peak strength by loading. As the loading continues beyond the peak strength, an abrupt loss of strength takes place. Adapted from (Wiig et al., 2019).

2.1.1 Failure mechanisms and landslide morphology

Various studies have examined the failure mechanisms of sensitive clay landslides (Gregersen, 1981; Leroueil, 2001; Thakur et al., 2006). After the Rissa landslide in 1978, Gregersen (1981), observed that sensitive clay landslides developed by two distinctive mechanisms, described as retrogressive- and "flake-type"- failures. The retrogressive mechanism was first proposed by Bjerrum (1955), who described it as a series of smaller slides developing from the areas behind an initial slide (Figure 10A). The initial slide can be triggered by erosion, digging or the placement of a filling. Retrogressive slides are often characterized by a pear/bottleneck shape, due to the slide advancing backwards and sideways (Figure 10B) (Wiig et al., 2019). As the smaller slides are released from the scarp, the material is completely liquefied, resembling a river of clay (Gregersen, 1981). Although relevant, the retrogressive failure mechanisms is not the most dominant process for larger quick clay slides. This is, according to Gregersen (1981), the flake-type failure mechanism.
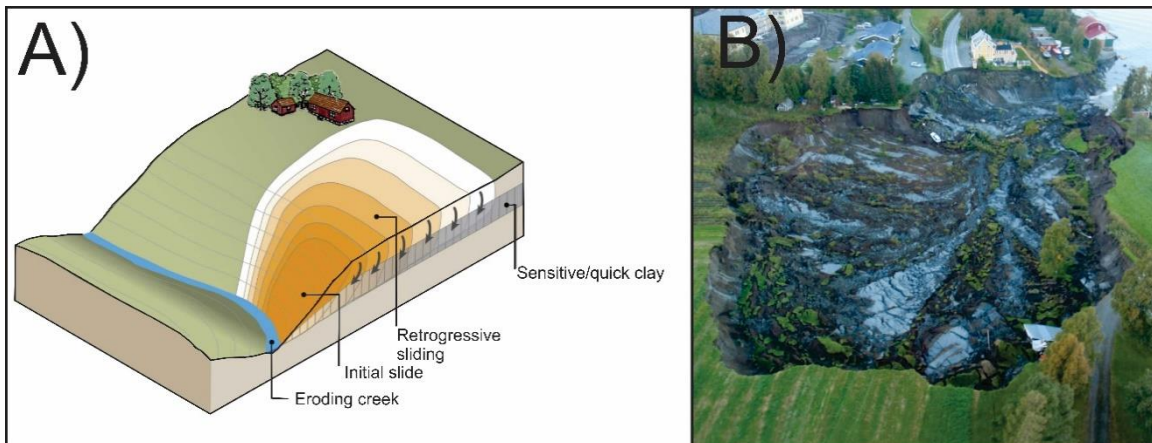
Figure 10: A) Schematic illustrating the initiation and advancement of a retrogressive slide. Adapted from (Wiig et al., 2019). B) Quick clay slide in Lyngen from 2010. The slide displays the typical "pear-shape" associated with retrogressive slides. Photo: Andrea Taurisano, NVE.

The flake-type failure mechanism is characterized by detached flakes, up to tens of thousands of square meters, floating upon a thin layer of liquidized clay (Gregersen, 1981; Giles, 2020). The slides often initiate at relatively low slope angles, where surface-parallel layers with quick or sensitive clay are found (Figure 11). The size of the slide is determined by the height and length of the slope, where large and elongated slopes can result in slides of considerable size (Wiig et al., 2019). Flake-type failure can be either progressive or retrogressive, depending on where the slide initiates. For retrogressive flake-type failures, the slide is initiated at the toe of the slope moving backward, often caused by loading or erosion. Consequently, progressive flake-type failures initiate at the top of the slope, propagating forward, often as a result of an increased load at the top of the slope (Wiig et al., 2019). Although different, retrogressive and flake-type failure mechanisms can operate simultaneously on quick clay landslides. This was observed at the famous Rissa landslide in 1978, where the slide initially developed retrogressively before developing into a flake-type failure (Gregersen, 1981). Although retrogressive-, and flake-type failure are the main failure mechanism for sensitive clay landslides, one more category is usually included in landslide literature, namely rotational slides.
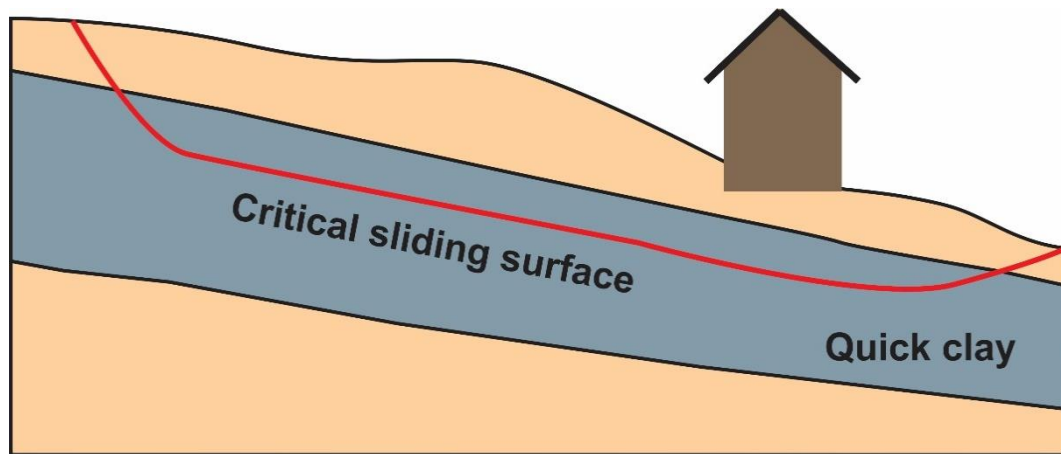
Figure 11: Illustration of flake-type slide. Red line indicates the critical sliding surface, where the quick clay has liquidized. Adapted from NVE (2019).

Rotational slides can occur in all types of soil, including sensitive clay. Typical for these types of slides, is that the slide moves in one piece and shows clear signs of rotation. Rotational slides can be both small and large, but are usually limited by the height and geometry of the slope (Wiig et al., 2019). Depending on the failure mechanism of the landslide, different morphological characteristics are left behind (Figure 12A).

Understanding how the morphology of landslides develops, is a central part in determining the failure mechanics of the landslide. For shoreline landslides, the morphology on the surface share many similarities with the morphology under water. However, due to the density of water, the transport of sediments will vary from the surface to under water. Depending of the gradient of the seafloor and size of the sediment, the morphology of the landslide will vary greatly. Rotational landslide morphology will have a concave- or circular failure (rupture) surface, where the material is not necessarily transported a long distance. On the other hand, translational slides often follow weak layers in the sediments (e.g flake-type mechanism), where sediment can be transported far away. If the landslide is composed of mostly fine-grained material, such as sensitive clay, underwater channels might form (Hansen et al., 2013).
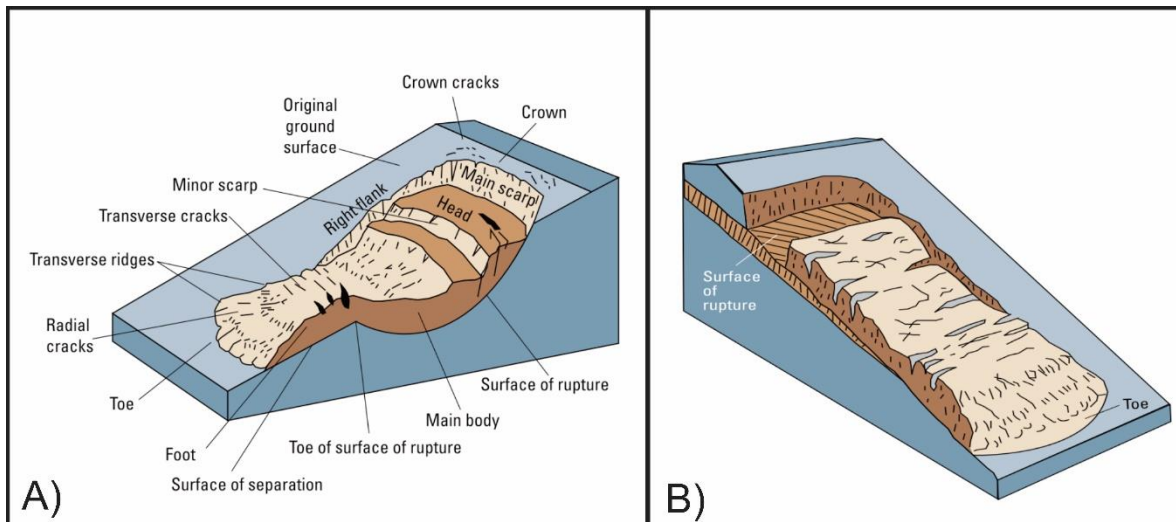
Figure 12: Examples of landslide morphologies left behind after A) Rotational slide. B) Translational slide. Figure retrieved from (Highland & Bobrowsky, 2008) after (Varnes, 1978).

2.2 Causal factors

For a slope to become unstable and fail, there are usually several conditions and processes involved. These are often labeled under the term "causal factors" (Popescu, 2002). Generally, these are divided into two categories, natural and human-induced. This is due to the fact that human activity has been linked to be one of the most effective triggers for landslides (L'Heureux et al., 2011). Due to the complexity of causal factors, a short summary of the most relevant causal factors for will be presented next.

Figure 13: A) Schematic illustration of pre-failure and failure conditions that influence the stability at the shoreline. B) Conceptual representation of the different processes and stages in the development of the landslide (L'Heureux et al., 2010).
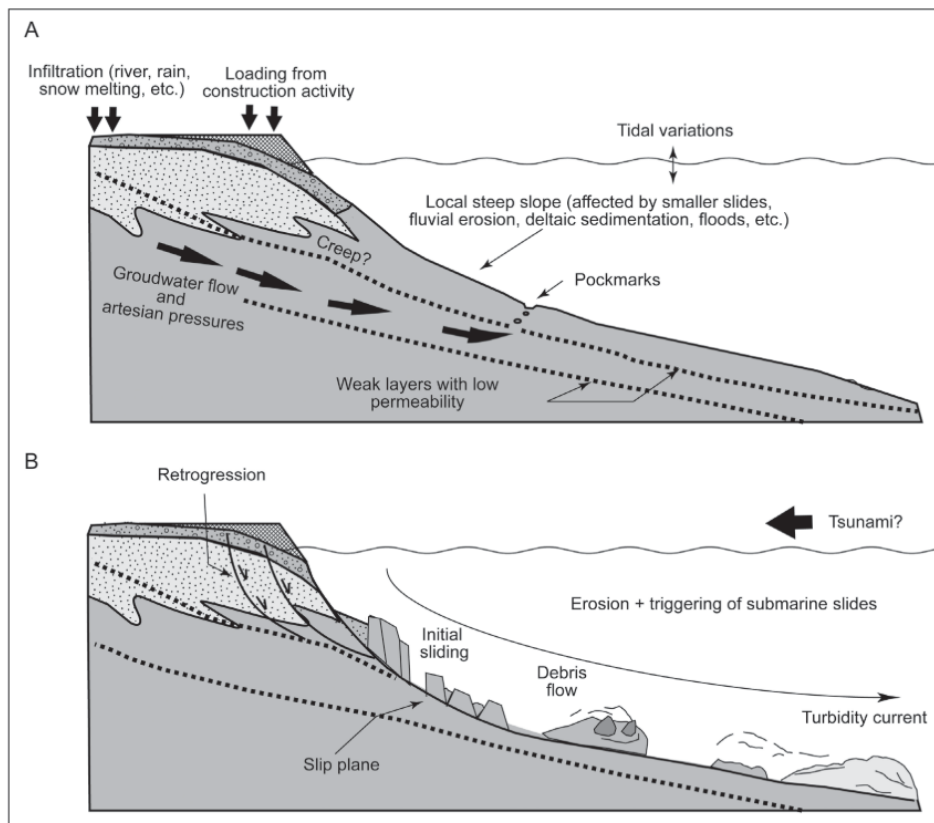
2.2.1 Hydrology and climate

Hydrology and climate are physical processes that affect the stability of shoreline slopes. Intense and prolonged periods of rainfall or rapid meltdown of snow are examples of causal factors associated with hydrology and climate (Popescu, 2002). Rainfall and snowmelt can influence the stability of the slopes both chemically through leaching, and mechanically through the development of pore pressure. In Norway, several studies have linked landslides directly to these types of causal factors, making them highly relevant to consider, especially in areas with sensitive clay (L'Heureux et al., 2010). Particularly the effect of excess pore pressure has proved to be relevant for the stability of slopes, and will therefore be discussed in greater detail in chapter 2.3.

 In addition to rainfall and snowmelt, Kramer (1988), demonstrated a trend of shoreline landslides occurring during low tide. Changes in shear stress related to the drawdown of water

may be sufficient to trigger liquefaction of sediment in zones with high initial stress (Kramer, 1988).

2.2.2 Erosion and sedimentation

Erosion is one of the most crucial destabilizing factors for slopes, and has consequently been examined in many landslide related studies (L'Heureux et al., 2010; Hansen et al., 2011;L'Heureux et al., 2017). Erosion can happen both at the surface and on the seafloor, making it an important factor to consider. Rivers, creeks and ocean currents are all possible sources of erosion (Figure 13A). Undercutting of a slope by a river or ocean current removes material at the toe of the slope, reducing the stability of the slope (Duncan et al., 2014). Studies by Hansen et al. (2013) showed that over half (55%) of the investigated landslides in the study had initiated at the mouth of the river/creek, indicating a strong correlation to the effects of erosion. Although rivers and creeks possess the ability to erode, they also contribute to the opposite action, namely sedimentation.

For marine environments, sedimentation and erosion are continuous processes that affect the sediment thickness and slope angle of the shoreline and seafloor. Quick sedimentation can cause a build-up of excess pore pressure in submarine sediments that are being buried, subsequently lowering the stability. However, this requires an ample and steady supply of sediment, which is usually only found at the mouth of larger rivers or deltas (Hansen et al., 2013). Similarly, the slope angle can also be affected by erosion and sedimentation, where higher rates of sedimentation can lead to an increase in slope angle. Studies has shown that landslides along the shoreline are partially controlled by the angle of the slope, with most slides occurring between 12-21° (L'Heureux, 2013).

2.2.3 Weak layers

Studies from Norwegian fjords have shown that mechanically weak layers in the sediment often are necessary to facilitate slope failure (Hansen et al., 2011; Heureux et al., 2012). Such layers, often attributed to sensitive clays, are recognized by their geotechnical properties, distinguishing them from the surrounding sediment. High water content and low plasticity are typical, in addition to high sensitivity (S_t) and low undrained- (C_u) and remolded shear strength (Heureux et al., 2012).

2.2.4 Gas release and seismic activity

Due to the decomposition of organic matter, seafloor sediments are often influenced by gas. Gas is often recognized as gas bubbles in core samples, or as pockmarks or gas hydrates on seismic data (Figure 13A). The presence of gas changes the geotechnical properties of the sediments, by lowering the undrained shear strength or increasing the pore pressure, consequently reducing the stability (Hampton et al., 1996). Additionally, seismic activity also has the potential to trigger landslides. Vibrations from an earthquake can cause a collapse in the sediment structure, leading to increased pore pressure and liquefaction of the sediment (Hampton et al., 1996). However, very few landslides in Norwegian fjords have been linked directly to earthquakes (L'Heureux et al., 2011).

2.2.5 Human activity

Human activity has shown to be one of the more effective causal factors for landslides. According to a study by L'Heureux et al. (2013), 60% of the landslides investigated were linked to human activity. This activity usually involves loading from placement of rock and fill material, undercutting (debuttressing) of the slope, construction work or blasting. The resulting vibrations from loading and digging are in many cases sufficient to cause failure, especially if the slope is partially unstable from before. As a result, many landslides have been linked to road- and railway construction (Hansen et al., 2013). The following loading and vibrations associated with human activity, destabilize the slope by increasing the driving forces and pore pressure, consequentlty reducing the shear strength of the soil.

Evaluating the described causal factors, a common denominator becomes obvious, namely pore pressure. As pore pressure directly influences the shear strength of soil, and thereby the stability of slopes, the next section will describe this relationship in greater detail.

2.3 Shear strength

The evaluation of slope stability is considered as one of the more challenging and complex problems within geotechnical engineering and soil mechanics. Over the past decades, continued research and development of new technology have improved our understanding of the strength and limitations of soils, thereby refining the assessment of slope stability (Duncan et al., 2014). In spite of the recent advances, evaluating slope stability remains a challenge to this day, and involves many uncertainties.

In general, slope stability is defined in terms of shear stress and shear strength (Van Den Eeckhaut et al., 2013). For a slope to be stable, the shear strength of the soil must be greater than the shear stress. The shear strength is defined as the maximum value of shear stress a soil can tolerate before failing, and is regarded as one of the most important parameters for slope stability. For soils, the shear strength is controlled by the effective stress (σ') experienced by the soil (Duncan et al., 2014). This is again dependent on the total stress (σ) and pore pressure (u), as shown in equation (3.1).

$$\sigma' = \sigma - u \tag{3.1}$$

Total stress is the sum of all forces experienced by the soil, including the interparticle contact forces (σ'), and the forces transmitted through the water (u), divided by the total area. This means that the value of total stress is based on equilibrium, and that it will be the same regardless of the pore pressure (Duncan et al., 2014). Although pore pressure does not affect the total stress of the soil, it has an immediate effect on the strength of the soil. This leads us in to an important topic when evaluating slope stability, namely drained and undrained conditions.

The difference between drained and undrained conditions for soils depends on the soils ability to drain out water when subjected to a load. Again, this will rely upon the properties of the soil and the rate of loading (Holtz et al., 2010). For coarse-grained soils, such as sands and gravel, the situation is almost always regarded as drained. This is due to the large permeability of the material, where pore water quickly drains out under loading. On the contrary, soils with low permeability, such as silt and clay, will in most cases be regarded as undrained if the load is applied within a short timeframe (Holtz et al., 2010; Duncan et al., 2014). From Figure 14, the forces acting on a fully saturated soil can be observed. Due to the soil being fully saturated, all the voids are filled with water. If a load is applied faster than the soil can drain the water away, the forces of the load are carried by the increased pore pressure. For a soil in an undrained state, an increase in pore pressure will result in a decrease in effective stress, and a lower shear strength (Duncan et al., 2014). This is especially relevant for clayey soils, such as sensitive clay, where the permeability is low and undrained conditions are likely to arise. For that reason, water and consequently pore pressure, can be detrimental to the stability of slopes with sensitive clay. As a result, slope stability software is often used to model the effects of undrained- and drained conditions on a slope.
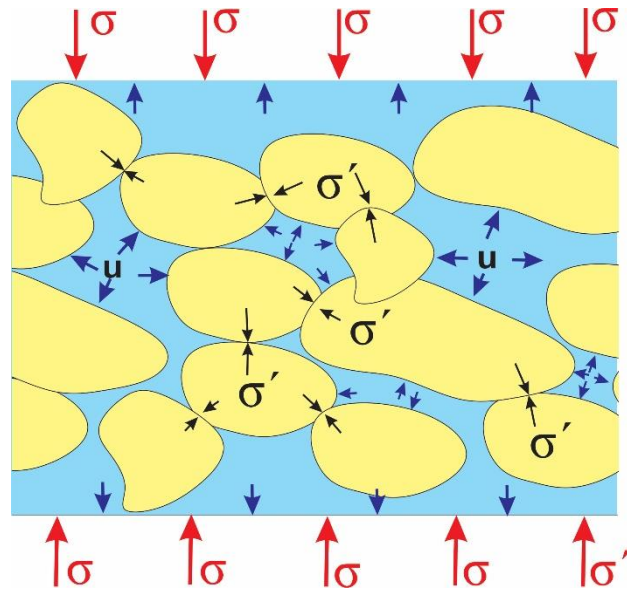
Figure 14: Figure illustrating the forces acting on particles in a saturated soil. As the water fills the void in the soil, pore pressure (u) will reduce the grain-to-grain contact between the particles, decreasing the effective stress (σ´).

2.4 Slope stability modeling

Slope stability modeling can be a beneficial method of evaluating the stability of a given slope. As with all models, it is important to be aware that the model is a simplification of reality, and evaluate the results with this in mind. The challenging part to any modeling is to recognize the weakness and limitations of the model, as well as the information it is based on (Wood, 2004). With the advancement of research and computer technology, slope stability modeling is getting more accessible as time goes on. Due to this, there is an array of software and methods available for modeling. Hence, the next section will aim to present the two most common methods used for modeling slope stability, namely Limit Equilibrium Method (LEM) and Finite Element Method (FEM). In addition, their benefits and limitations will be mentioned, as well as their applicability for modeling sensitive clay.

The LEM is the most common method for analyzing slope stability in both two and three dimensions. This method investigates the equilibrium of a slope under the forces of gravity. The intent of the LEM, is to identify the ratio of available shear strength (τ_f) to the mobilized shear strength (τ_{mob}), commonly referred to as the factor of safety (FS) (Huang, 2014). Depending on factor of safety, the slope is regarded as stable if FS $\geq$ 1.0 and unstable if FS < 1.0.

$$FS = \frac{\tau f}{\tau mob} \qquad (3.2)$$

For calculating the factor of safety, the the Mohr-Coulomb criterion is used to analyze the equilibrium of forces at the moment of failure (Lin et al., 2014). This criterion can be viewed in equation (3.3), where s = shear strength, c = cohesion, σn = normal stress and Φ = angle of internal friction (Huang, 2014).

$$s = c + \sigma_n \tan \Phi \qquad (3.3)$$

The concept of LEM is simple, but as with any basic theoretical method, there exist several approaches and versions. One of the more popular approaches is the *method of slices*. For the method of slices, the soil is discretized into vertical slices, and the forces acting on each slice is calculated, as shown in Figure 15. Depending on the software and aim of the modeling, different analysis methods can be implemented for calculating the forces that are acting on the slices. Some of the more popular methods are:

- Bishop simplified
- Janbu simplified
- Janbu corrected
- Spencer
- GLE-Morgenstern-Price

All the mentioned methods give different variations and in how the FS is calculated. However, due to the scope of this thesis, these methods will not be explained in detail. For more information, see (Huang, 2014).
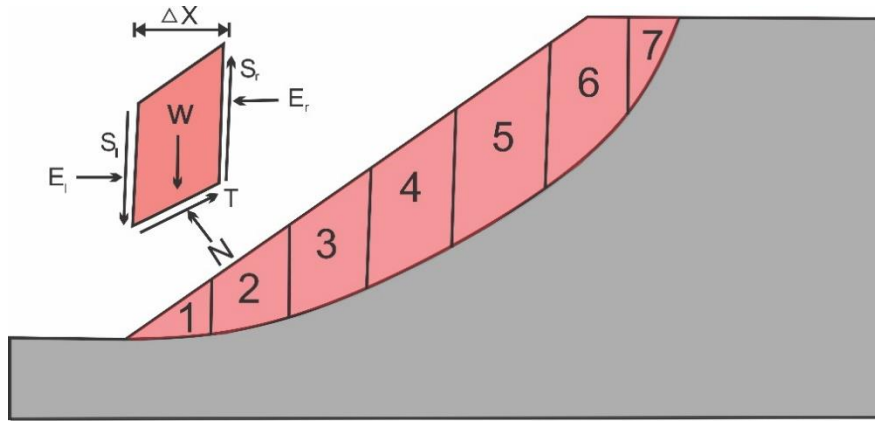
Figure 15: Schematic of a failure mass divided into a number of slices. The free-body diagram to the left illustrates the forces acting on a singular slice. The forces applied are weight (W), normal force (N), shear force (T), normal force on the vertical side (E_l/E_r) and shear force on the vertical side (S_l/S_r). The width of the slice is given by ΔX. Adapted from: (Huang, 2014).

The benefits of using a modeling software based on LEM, is that it is relatively fast and requires few input parameters. However, due to the simplifications, the results of the modeling might not reflect the conditions in the field. Stability analyses using LEM, assumes that the soils behave perfectly plastic, thus not accounting for the strain-softening behavior of the clay (Oset et al., 2014). As a result, simplified stability models, such as LEM, should only be used as a precursor for determining the stability of areas with sensitive clay. For more reliable data, a more complex model, such as FEM should be implemented.

With the development and advances in computer technology, the FEM has been increasingly used in slope stability modeling. Compared to the LEM, the FEM does not require any assumptions about the geometry, location of the failure surface, or directions of slice side forces. This allows the method to be applied on complex slope geometries and soil compositions, both for two- and three dimensions. In addition, the models can account for brittle soil behavior, which is a significant advantage when modeling with sensitive clays (Rocscience, 2001).

3 Methods and data

The results and interpretations presented in this thesis were acquired by a combination of methods based on various data sources, such as former studies and reports, digital mapping and acquired field data.

➢ Digital mapping

Digital mapping was completed using observations and drone-imagery collected in the field, as well as external data sources (Table 1). This was implemented in a geographic information system (GIS) using the ArcMAP application. ArcMAP is a primary GIS desktop application which is used to process and display GIS datasets, compile and distribute maps, and document geographic information (ESRI, 2020). For this thesis, version 10.6 was used for creating geological profiles, geomorphological maps, georeferencing data and creating hillshades. In addition, an orthomosaic of the landslide was created by drone-images collected in the field, which were implemented and processed in the software DroneDeploy (DroneDeploy, 2020), before being uploaded to ArcMAP.

➢ Fieldwork

Kråknes and its surrounding area was investigated from the 27th of July to the 1st of August, 2020. All fieldwork was carried out with concurrent master student Stina Mari Pettersen. For the first two days, the fieldwork was assisted by the supervisor, Louise Vick. The purpose of the fieldwork was to investigate the landslide and the surrounding area through the following:

- Geotechnical mapping of the soil profile in and outside of the landslide area, using the app Clino (from FieldMove) for collecting data.
- Geotechnical classification of in-situ soil using the New Zealand Geotechnical Society soil classification field guide (NZGS, 2005).
- Image and video collection using Mavic 2 Pro Uncrewed Aerial Vehicle (UAV).
- Soil sample collection in case of further testing needs.
- Mapping of structural orientations in the surrounding bedrock.
- Mapping of surface and groundwater flow and flooding, evidence of erosion and other factors which may contribute to instability.

➤ Ground investigation

After the slope failure on the 3rd of June 2020, subsurface ground investigations were engaged by NVE and carried out by Multiconsult AS. This consisted of 12 total soundings, two cone penetration tests and three retrieved core samples (Figure 16). The data and lab analysis from Multiconsult was later issued in a report, which has been a crucial resource for tying together field observations and providing geotechnical parameters to the slope stability models. Though this thesis was carried out separately to the Multiconsult ground investigation, a short summary of the methods associated is presented as the results are heavily referenced in this thesis.
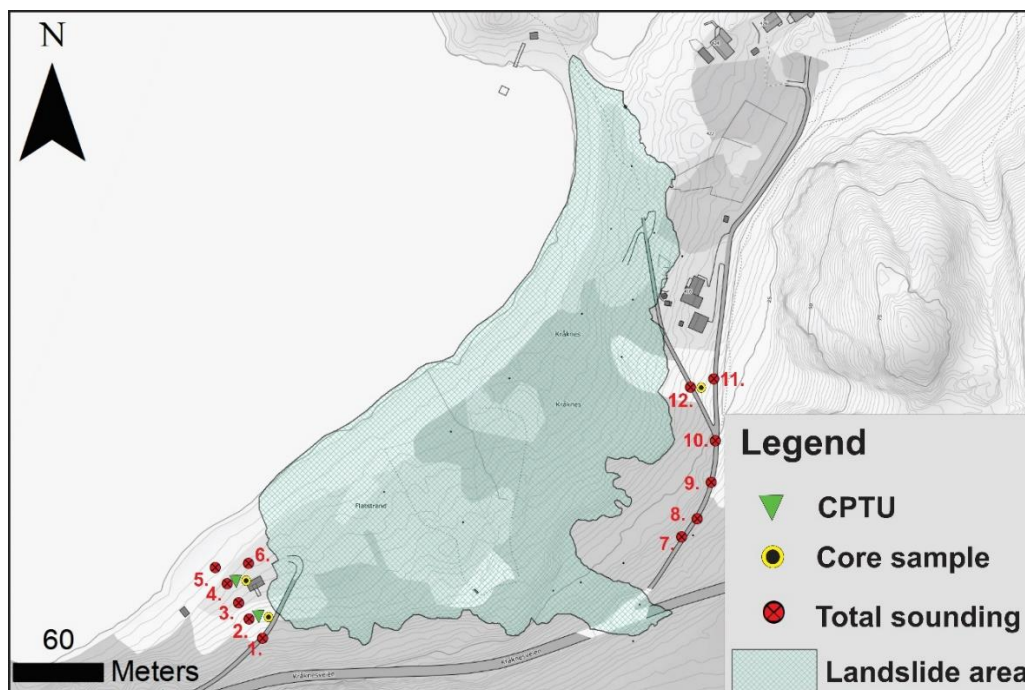

Figure 16: Topographic map displaying the location and order of boreholes completed during the ground investigations by Multiconsult (Kartverket, 2020).

The total sounding, CPTU and core samples were completed by a hydraulic drill rig, as shown in Figure 17. These drill rigs are constructed specifically for geotechnical ground investigations, and are thus able to perform multiple tests depending on the equipment of the drill. The ground investigations at Kråknes were all performed by the same drill rig, where the focus was to investigate the prevalence of quick clay in the area, as well as collect samples for further testing. As observed from Figure 16, most of the ground investigations performed at Kråknes were total soundings.

Figure 17: Photo of the hydraulic drill rig used at Kråknes. The rig is driven to the location by a remote operator. Photo: Multiconsult.

Total sounding is a well-known method of mapping soil stratifications and determining the depth to bedrock (Figure 18). The method combines rotary-pressure-sounding and drilling to penetrate the soil. The main measurement of the total sounding is penetration resistance force (kN), which is used for determining soil stratification (Haugen, 2016). The data from the total sounding can be used to identify harder and softer layers in the soil profile, and more importantly, the location of sensitive clays. Clays are generally characterized by low penetration resistance and a smooth sounding curve (NGF, 1994b). However, there can be situations where softer materials are camouflaged due to the friction of the overlying layer. Thus, results from total sounding should only be used as precursory information of the ground conditions. For more precise information regarding soil stratification and identification of sensitive clays, CPTU-test and lab analysis is recommended (NGF, 1994a).
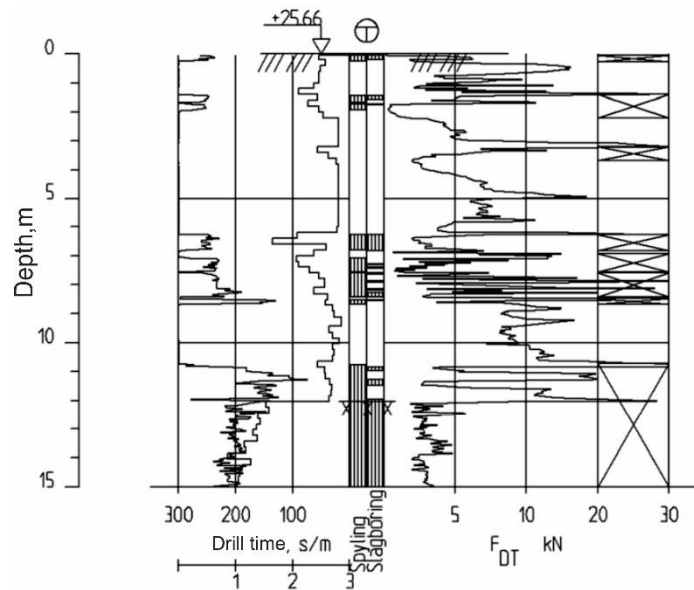
Figure 18: Total sounding profile/drill log for alternating hard and soft soil layers (NGF, 1994a). Drill log shows sounding in the left column and resistance in the right. The central column indicates changing methods depending on the resistance. Bedrock interface is marked by the x's in the middle column.

Cone penetration test undrained, hereafter referred to as CPTU, is a test method that is often used in geotechnical ground investigations, especially regarding the detection of quick and sensitive clay. The method is well known and regarded as one of the most precise in-situ measurement methods (Lunne et al., 1997). For a CPTU-test, a cone situated at the end of series of rods is pushed through the soil at a constant rate of 20 mm/s. During the test, cone resistance q_c, sleeve friction f_s and pore pressure u are recorded simultaneously by the cone penetrometer (Figure 19). The measurements are updated continuously every 0.02 meters, thus ensuring accurate information about the ground conditions (NGF, 1994b). Even though CPTU-tests are regarded as one of the most accurate in-situ tests, they are often accompanied by lab analysis to verify the results.
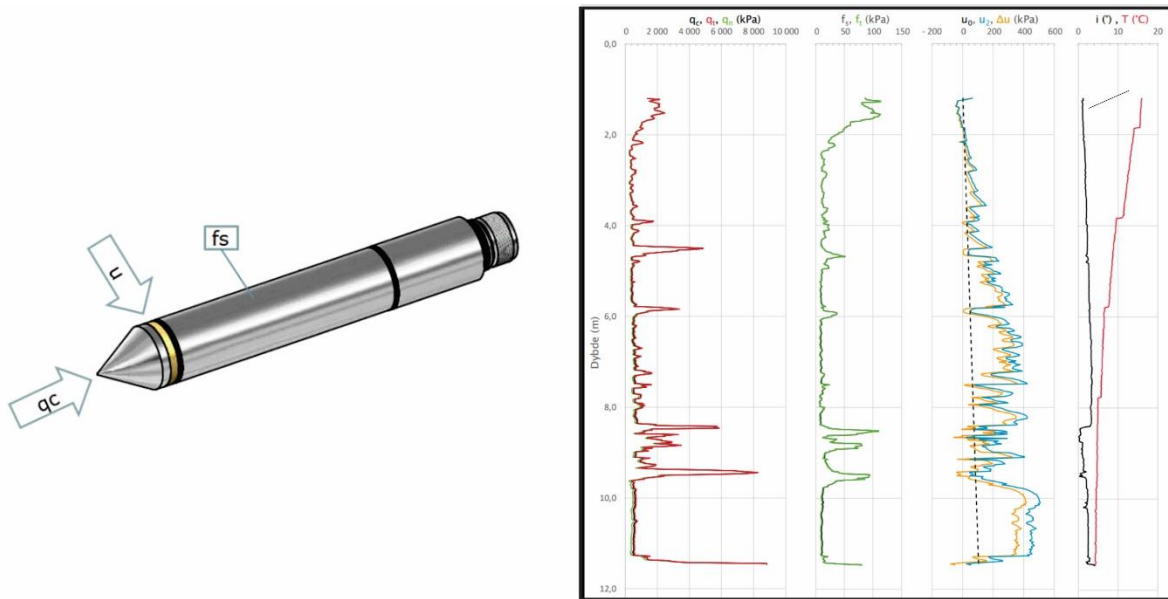
Figure 19: Illustration of CPTU cone (Geotech, 2015) and generated data (Waldeland, 2020).

In addition to total sounding and CPTU-tests, samples collected from the drill rig were tested by Multiconsult in a geotechnical lab following the slope failure at Kråknes. This negated the need to perform mechanical tests on samples collected for this thesis.

The included tests were: grain size distribution-, oedometer-, fall cone - and test and triaxial test. From the tests, soil samples were classified and identified with respect to their sedimentary and geotechnical properties. Values such as water content, density and disturbed- and undisturbed shear strength were determined.

> InSAR

Interferometric Synthetic Aperture Radar, better known as InSAR, was used to investigate ground motion at Kråknes prior to the slope failure. InSAR is ground motion measured by radar from satellite, where the data provided from the satellite is used in a mapping service to detect and track ground motion, with a millimeter-scale accuracy (Dehls et al., 2019). This method of measuring ground motion can detect areas that had otherwise been overlooked, even reaching places that cannot be reached by foot. Due to the orientation and geometry of the satellite orbits, the dataset is divided into two, ascending and descending. The ascending dataset measures eastward motion as negative, and westward as positive, while the descending dataset measures the opposite (Figure 20). For this study, datasets obtained from the Sentinel-1 Descending-1 satellite from 2015-2019 were used to investigate the average ground displacements at Kråknes.
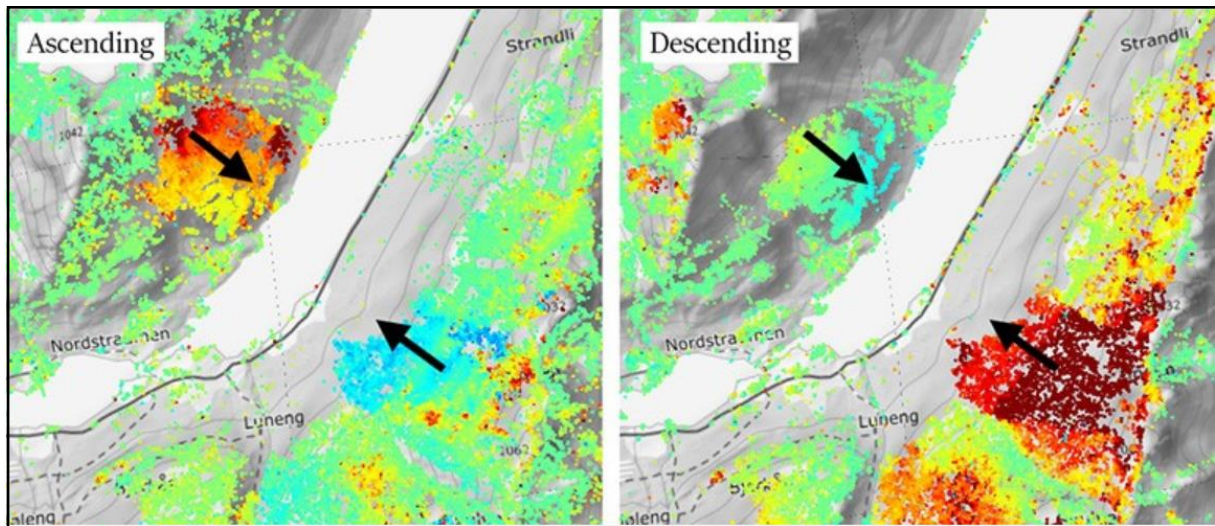
Figure 20: Maps illustrating the effects of the ascending- and descending datasets. Arrows indicate the movement of two unstable rock slopes moving towards east and west. Source: (NGU, 2020a).

Although InSAR is a relatively accurate and beneficial method of measuring ground motion in most cases, it has some known issues. The measurements from the satellites can be affected by snow cover, where snow is available between the months of June and October, when the data is collected. Annual variations due to changes in water content are also a source of error, especially for wetlands where changes can fluctuate more from year to year. The data can also be affected by noise, resulting in data points getting registered with the wrong values (NGU, 2020a).

➤ Statistical data

The statistical weather data presented in this thesis has been collected from reports and web-based forecasting tools. The bulk of the reports used for analyzing the environmental conditions prior to the slope failure at Kråknes are monthly weather reports distributed by The Norwegian Meteorological Institute (MET). These reports present and summarize temperature and precipitation for the chosen month and list detailed data from specific weather stations. In addition to the reports, information regarding landslide forecasts, snow- and hydrogeological conditions (groundwater level, soil saturation) were gathered from Xgeo.no.

Xgeo is an expert web-based tool used for forecasting and monitoring natural hazards (floods, landslides, snow avalanche and drought). In the model, Norway is split into 1 km^2 grids, where the information of the grids are based on real-time measurements, forecasts and model

simulations (Figure 21). Due to the data collection and simulations of the model, Xgeo permits the user to explore the modeled conditions for an area, both for past, present and future (Devoli et al., 2015).
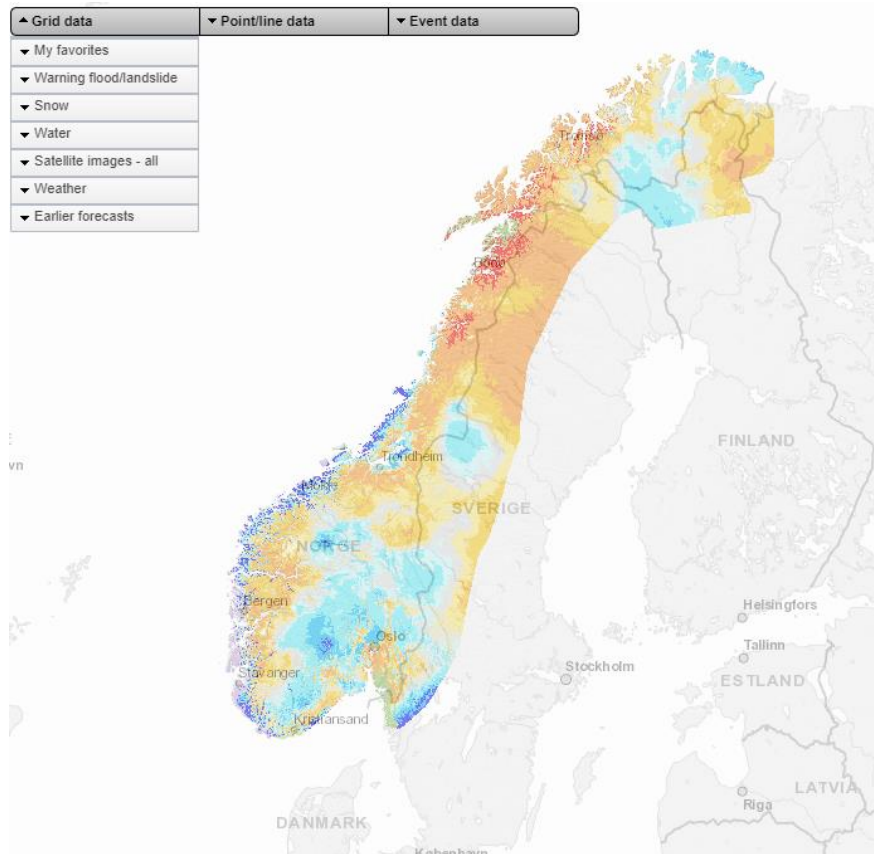

Figure 21: Overview map from Xgeo. Grid data menu shows the different categories of data available. Source: Xgeo.no.

➤ Slide2

The slope stability models presented in this thesis were generated using the slope stability program Slide2, developed by Rocscience. Slide2 is a 2D LEM program used for analyzing slope stability for both rock- and soil slopes (Rocscience, 2020). The analysis in Slide is based on the *method of slices*, mentioned in chapter 2.4. The program enables the user to define the geometry and material properties of the slope in question, in addition to choosing between a number of integrated methods, such as Janbu, Bishop and Spencer, when calculating the factor of safety.

The benefit of using a modeling programs such as Slide is that the analysis method is based on a well-established principle. In addition, the program is easy and fast to use, and requires relatively few in-put parameters. This simplicity also carries with it certain weaknesses and limitations that the user must be aware of.

For this thesis, slope profiles were obtained from the LiDAR- and bathymetry data provided by NVE (Table 1) and then imported to Slide. The profiles were then created with material boundaries, thickness and parameters based on fieldwork and available ground investigation data. All modeling was performed for non-circular and composite failure surfaces, using the grid-search method (Rocscience, 2021a).

4 Results

This chapter aims to present the most central elements that may have influenced the slope stability at Kråknes. To get a better understanding of how the slope failure evolved, an assessment of the sequence of events will be presented first. Subsequently, an in-depth study of hydrometeorology, ground conditions, geotechnical data and human activity will be presented, with a focus on the causal factors uncovered. In the end, this data will be implemented in Slide2 for slope stability modeling.

4.1 Sequence of events

The landslide at Kråknes is not a single event, but rather a culmination of destabilizing circumstances, that when combined, ended in the slope failure on the 3rd of June, 2020. As such, considerations for stability reducing factors must exceed the day of the landslide. Contributing factors started earlier in the year. Adverse weather conditions led to a large amount of snow being deposited at Kråknes and the surrounding catchment area during the first months of the year. This was combined with low and stable temperatures, ensuring the preservation of the snowpack. Warmer temperatures did not prevail until the middle of May, generating an instantaneous release of meltwater and facilitating unstable conditions. Circumstances regarding temperature, precipitation and snowmelt will be described in more detail later on 4.2. For the landslide itself, the main sliding event transpired over three days, from the 3rd – 6th of June, with a total of 12 major failures, as presented in Figure 22. However, signs of instability were observed at Kråknes prior to the main sliding event.
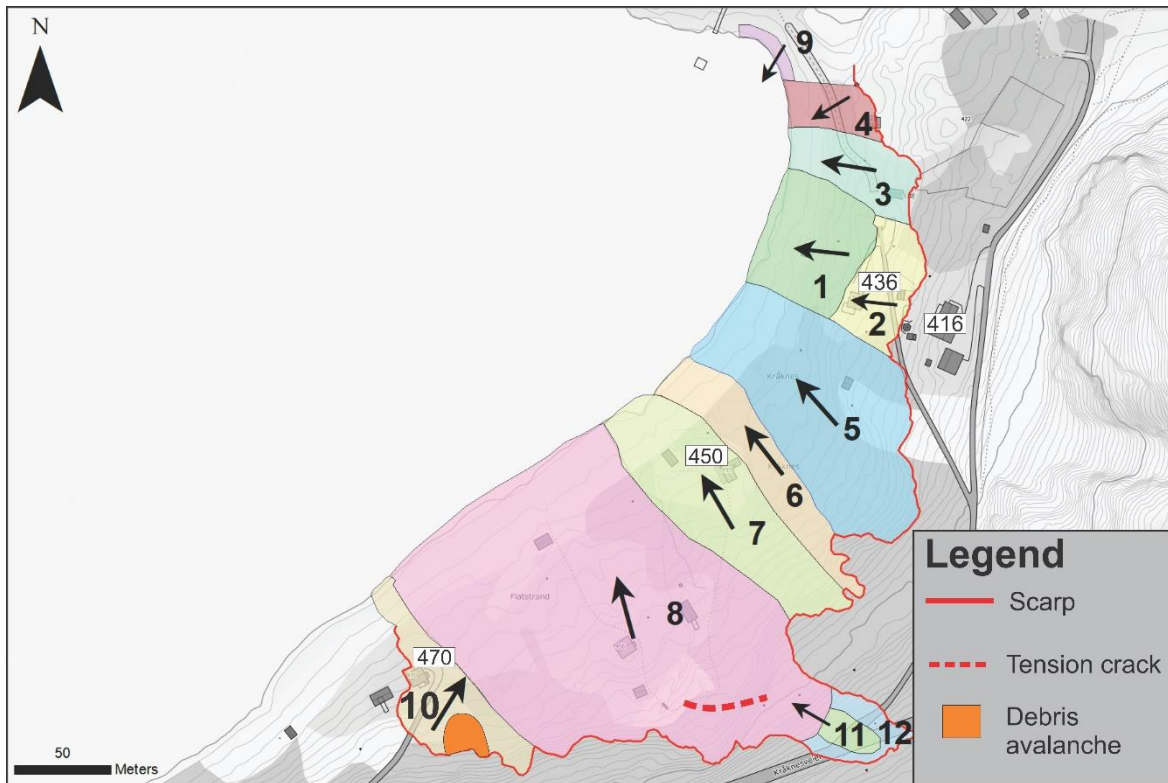
Figure 22: Proposed sequence of events for the Kråknes landslide. This map is based on video observations and reports from local residents.

After the temperatures had increased in the middle of May, local cabin owners staying at Kråknes between the 27th -29th of May stated that large amounts of water was observed on the fields and in the gutters around Kråknesveien 470 (Figure 22). Additionally, on the 29th of May, five days before the landslide, a smaller debris avalanche was reported above the cabin at Kråknesveien 470 (Figure 23 C/D). The landslide cut the water supply for one of the cabins, and was reported to the Flood and Landslide Warning Service. In the statement from the locals, it was emphasized that there was much water and clay on the ground in the area.

Some days after the small landslide, on the 2nd of June, locals reported that a crack had formed in the area. The 30 to 40 meter long tension crack was observed cross-cutting the road to one of the cabins. This crack was later filled in with sand, so that the residents could leave the cabin by car (Figure 23B).

Figure 23: A) Overview map of Kråknes. B) Tension crack discovered on the 2nd of June (Photo: Jan Egil Bakkeby). C/D) Small landslide reported by locals on the 30th of May (Photo: Marit Ekerhovd).

On the 3rd of June, at 15:15, a local living at Kråknesveien 416 was working outside on his house when the first slide initiated. He observed that the power lines from his house were pulled of the wall, and dissapeard down towards the fjord. After moving closer to the edge, he witnessed the house on his second property (Kråknesveien 436, Figure 23A) sliding into the water. From his house, located on bedrock, he witnessed the initial progression of the slide (sequence 1-7). Witness statements confirmed that the sliding progressed laterally northward in

a sequence of failures, before eventually moving to the south. Video observations from the nearby mountaintop confirmed this, as it captured sequence 8 on film (Figure 24

Figure *24*: Snapshots of the southward progression of the Kråknes landslide captured on video. A large flake is observed sliding into the fjord. This flake corresponds to sequence 8 in . Source: (Larsen & Quist, 2020).

). Approximately one hour after the first slide, at 16:20, slide number 10 initiated, marking the end of the sliding activity that day.

Figure 24: Snapshots of the southward progression of the Kråknes landslide captured on video. A large flake is observed sliding into the fjord. This flake corresponds to sequence 8 in . Source: (Larsen & Quist, 2020).

In the following days, smaller slides were released from the scarp, before the two last slides (11 and 12) released on the 5th and 6th of June. At this point, the landslide crossed the main road (Kråknesveien), as shown in Figure 25.

Figure 25: The development of the Kråknes landslide from the 4th-6th of June. As observed, the landslide removed parts of the main road on the 5th of June, and continued to develop backward until the 6th of June. (Photos: Anders Bjordal).

4.2 Hydrometeorology

Due to the effects of global warming, annual temperature and precipitation are increasing and expected to increase drastically during the next century. As a result, heavy rainfall and floods are becoming more frequent (Norsk Klimserviceasenter, 2016). About one-third of the yearly precipitation in Norway is stored as snow during the winter. As warmer temperatures follow from winter to spring, most of the snow is melted into water (NVE, 2016). With warm temperatures and large snow masses in the mountains, the risk of flooding increases. Thus, monitoring the accumulation and volume of snow is important for better prediction of flooding events. For predicting and analyzing the consequences of climate change, meteorological data is essential. When it comes to natural disasters such as slope failures, meteorological data can give viable input for analyzing past and future events. For the slope failure at Kråknes, meteorological data will be necessary to evaluate the effects of temperature, precipitation, snow cover and water. Thus, a study of the hydrometeorological conditions preceding the event will be presented first.

4.2.1 Temperature and precipitation

The year 2020 started with high temperatures and precipitation. January 2020 experienced an overall 2.1°C increase in temperature when compared to the normal from 1961-1990 (Figure 26). In addition, precipitation rates were 125% of the median value of the same period. Although changes were observed over the whole country, they were especially prominent in Finnmark. The area around Kråknes experienced an increase in temperature of 2.6-3.0°C and precipitation rates 150-200% of the normal (Grinde et al., 2020a).

Continuing to February, temperature and precipitation rates were still high. February was 4.0°C above average (Figure 26), with overall precipitation measured at 190%, adding up to the seventh wettest February in the last 120 years (Grinde et al., 2020b, Figure 27). For the area around Kråknes, temperatures averaged 3.0-4.0°C above normal, with precipitation ranging between 175-200% (Grinde et al., 2020b).

For March, the average temperature was 2.4°C above normal (Figure 26). Likewise, precipitation was recorded as 170% of the normal, with some weather stations in Finnmark registering 2-300% of the normal amount (Grinde et al., 2020c, Figure 27). Similarly, for April,

precipitation ranged between 150-175% of the normal, with a temperature variance of 1.0-1.5°C (Grinde et al., 2020d).

Following into may county of Troms and Finnmark experienced a higher increase in average temperatures compared to the rest of the country, registering from 0.5-2.0°C above average for the month (Grinde et al., 2020e, Figure 26). However, even with warmer temperatures, two-thirds of the month still registered below 5°C at Kråknes. The three warmest days were registered from May 31st to June 2nd, just before the slope failure. During these three days, the average termperture ranged from 10.8 to 13.6 °C, with maximum temperatures between 17.2 and 18.7 °C. Precipitation was generally low for May, with no considerable amount recorded before the slope failure (Meteorologisk Institutt, 2020).
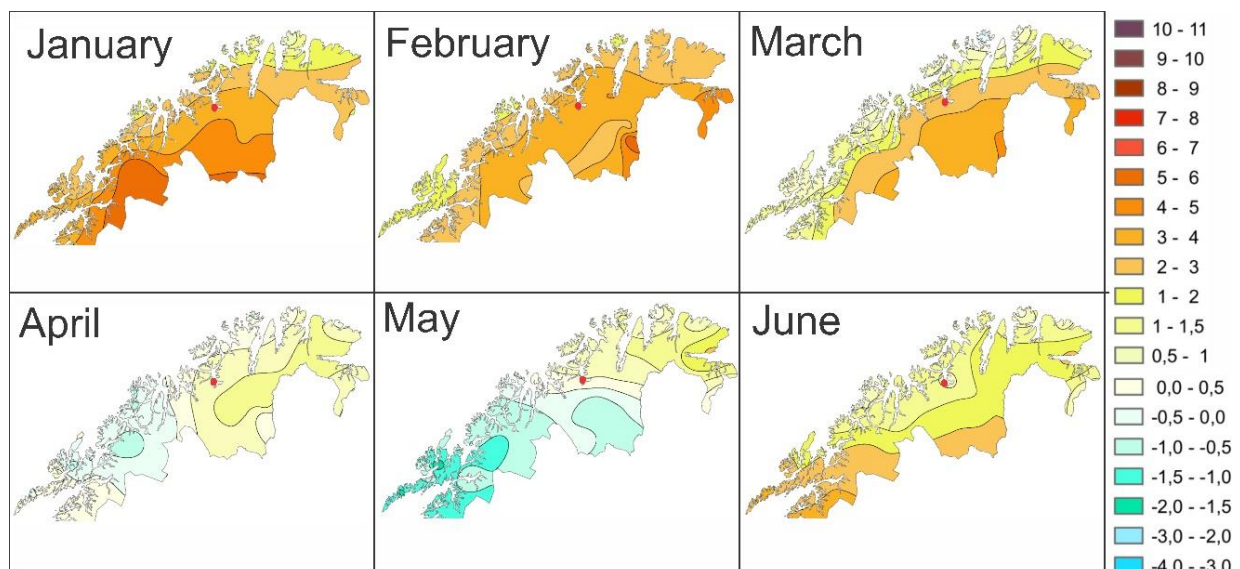

Figure 26: Temperature map for Troms and Finnmark. The location of Kråknes is represented by a red dot. Temperature (°C) is presented as the variation from the monthly normal. Adatpted from Grinde et al. 2020a,b,c,d,e,f).
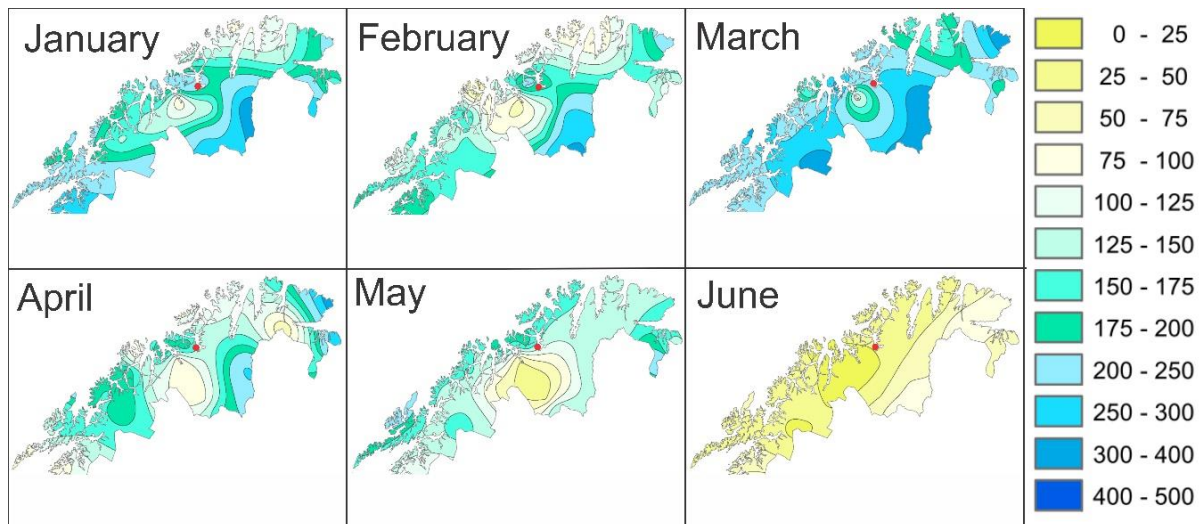
Figure 27: Precipitation map of Troms and Finnmark. The location of Kråknes is represented by a red dot. Precipitation (%) is presented as the variation from the monthly normal. Adapted from Grinde et al. 2020a,b,c,d,e,f).

4.2.2 Snow cover

The heavy precipitation in January, February and March generated large volumes of snow in Troms and Finnmark. As a result, several gauging stations recorded snow depths close to an all-time high. As an example, the month of March 2020 had the most recorded snow, going back to 1958 (NVE, 2020). The combination of a thick snowpack and low temperatures resulted in the preservation of the snowpack, even into the warmer months of April and May (Grinde et al., 2020d). Snow covered most of Kråknes and the surrounding mountains until the end of May. It was not until the turn of the month that warmer temperatures led to a drastic decrease in snow cover, as observed in Figure 28.
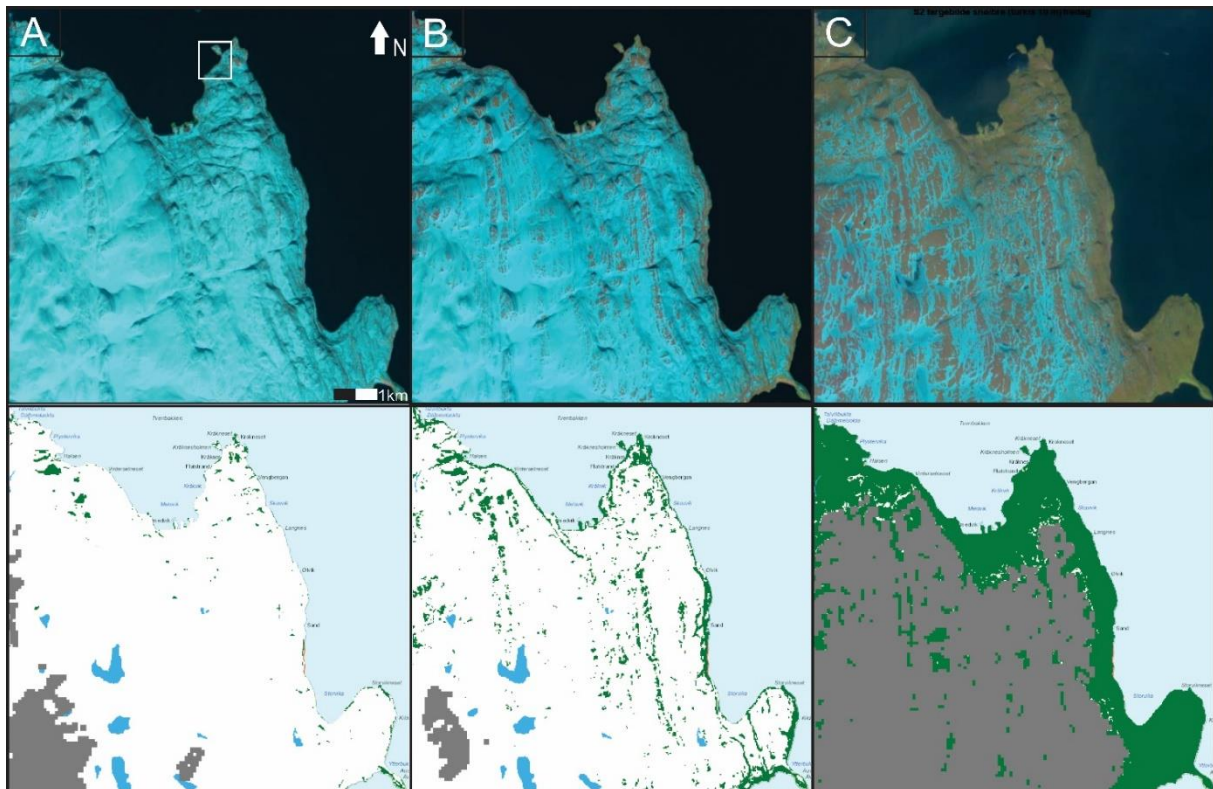
Figure 28: Figure illustrating the snow-cover at Kråknes and the surrounding area at three different times. The snow-cover is demonstrated both by orthophoto and concurrent snow-cover model from Xgeo. In the model, white color illustrates snow cover, while green is bare ground. Dark grey color comes from cloud cover. A) Snow-cover at 02.05.2020. The location of Kråknes is illustrated by a white square. B) Snow-cover at 22.05.2020. C) Snow-cover at 05.06.202. Retrieved from Xgeo.no.

The snow depth at Kråknes measured 70-80 cm in the start of May (Figure 29B). It was not until the influx of warmer temperatures around the 23rd of May, that a more drastic increase in snow melt was observed (Figure 29A). As a result of the warmer weather, the snow-melt peaked during the 24-29th of May, reducing the snowpack from 55 to 20 cm (Figure 29B). Subsequently, a new period of warmer weather followed into the start of June, although snow-melt levels continued to drop due to the reduced snowpack. Hence, most of the snow at Kråknes had melted by the early days of June (Figure 28, Figure 29B).
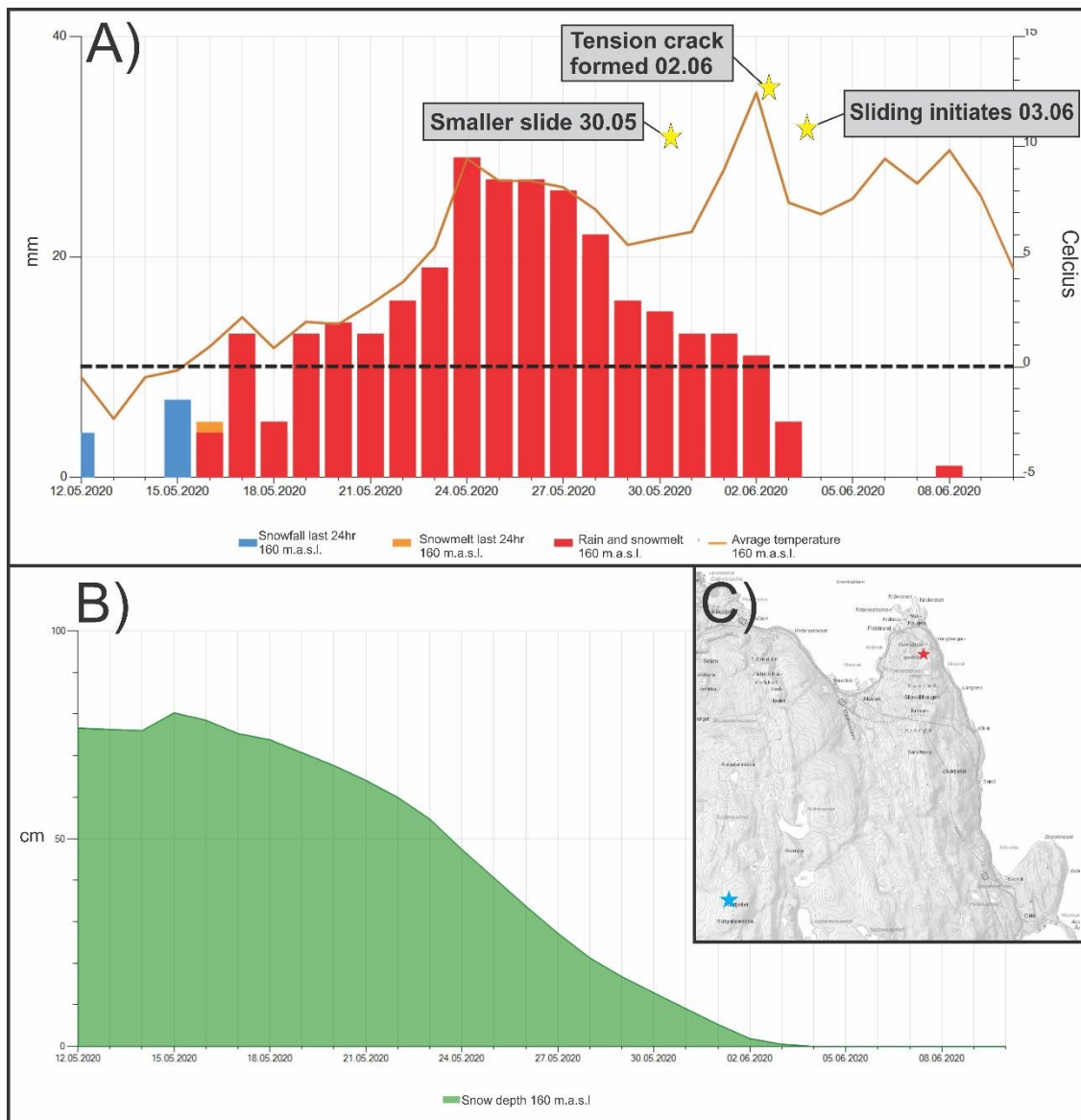
Figure 29: A) Graph displaying the snowfall and snowmelt in relation to temperature between May 12th and June 8th. B) Graph of snow depth at Kråknes. C) Topographic map of the study area. Red star marks the location of the measurements. Blue star marks the location of Flintfjellet. (Kartverket, 2020). Source: Xgeo.no.

4.2.3 Water

Water is one of the most effective triggers for landslide-related activity, as it penetrates, lubricates and erodes rock- and soil masses, reducing friction and decreases stability (Highland & Bobrowsky, 2008). Thus, it is essential to consider how water has influenced the area at Kråknes.

4.2.3.1 Groundwater levels and soil saturation

As temperatures rose and the snowpack started to melt during the middle of May, large volumes of water were released. This is reflected in the groundwater monitoring station at Lakselv, 70 km east of Kråknes (Figure 2B). The station at Lakselv is the closest monitoring station for Kråknes, and provides a useful proxy for groundwater level changes in the region. From the monitoring station, a considerable increase in groundwater level can be observed from the 18th of May (Figure 30A). This corresponds well with the increased temperature and snowmelt witnessed at Kråknes for the same time period (Figure 29A). As the groundwater level continued to rise during the end of May, it even exceeded the 100th percentile boundary, indicating exceptional circumstances (Figure 30A). These percentiles are calculated by comparing the registered groundwater level on the given day, to the groundwater level for the same day for previous years. This means that at the 50th percentile, we have the same amount of observations registered above and below. Subsequently, at the 100th percentile, all observations are equal to or less than the registered value. For Kråknes, a similar increase in groundwater level was observed. Here, the volume of groundwater was estimated to be 80-90% of the maximum on the 27th of May, and continued to increase to over 90 % of maximum to the 3rd of June (Figure 30 C/D). These maps show groundwater volume as a percent of the maximum value for the period 1981-2010 (Xgeo, 2020). In addition to the rise in groundwater levels, soil saturation levels also registered at an all-time high for this period.
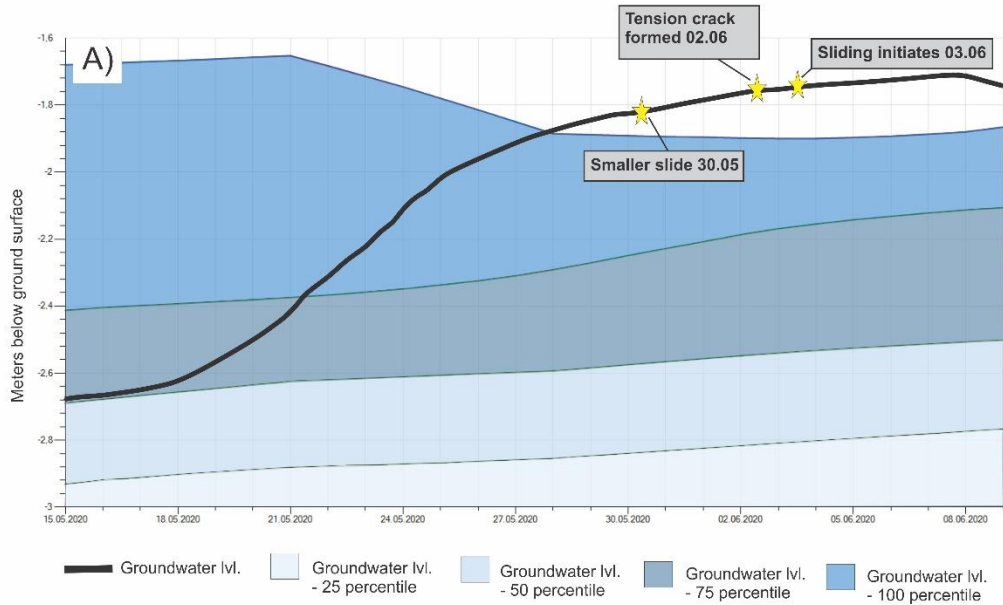
Figure 30: A) Graph of the groundwater level at Lakselv. The percentiles are based on the data from 1957-2020 (Xgeo.no). Yellow stars indicate the timing of the smaller debris avalanche, tension crack and sliding initiation. B) Groundwater volume in % of maximum for 27.05.2020 (source: xGeo.no, 1 km^2 grids). C) Groundwater volume in % of maximum for 03.062020 2020 (source: xGeo.no, 1 km^2 grids).

Soil saturation measurements from Kråknes revealed an increase from 55 to 100 percent from the 15th of May until the 1st of June (Figure 31). A similar increase in soil saturation was observed at Flintfjellet (775 masl), about 8 kilometers from Kråknes (Figure 29C), indicating that the temperatures at this time were sufficient to initiate snowmelt at higher altitude as well.
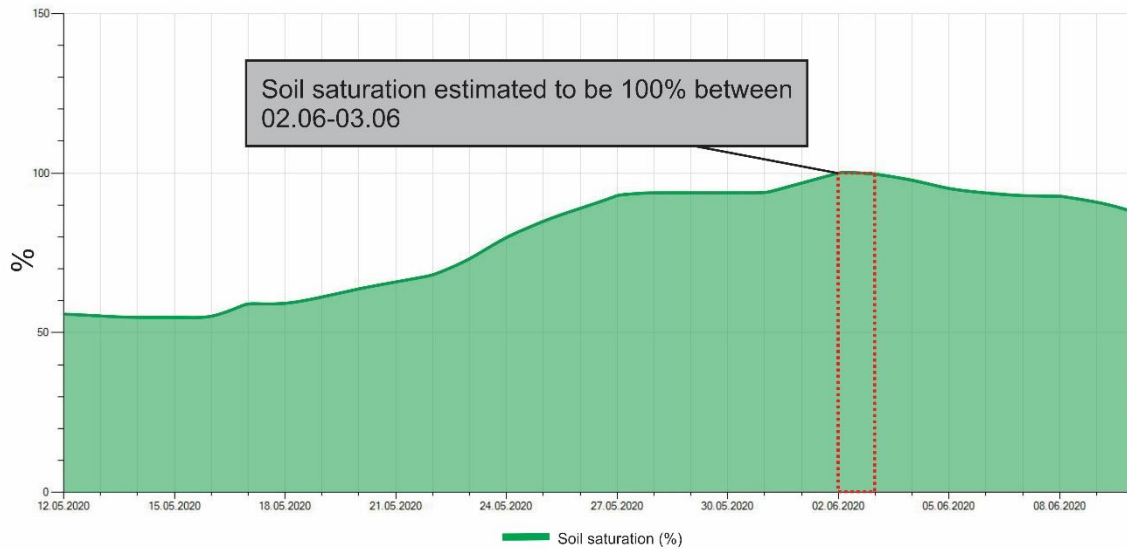
Figure 31: Graph of soil saturation (%) at Kråknes. Soil saturation was estimated to reach 100% on 02.06, the day before the landslide initiated. (Xgeo.no).

4.2.3.2 Tidal influence

Low water levels, represented by low tides, is known to have a destabilizing effect on slopes confined by water, due to the repeated fluctuations in pore-water pressure and (Kramer, 1988; L'Heureux et al., 2011). Consequently, variations in the tide must be analyzed in days leading up to the main sliding event.

For Kråknes tide levels fluctuates between 45 and 260 cm above the sea chart datum in the days leading up to the event. On June 2nd at 17:00 tension cracks crossing Kråknesvegen 450 were observed by a local. At this time, the tide level was registered at 59 cm, corresponding to the value of "mean low water springs". For the initiation of the main sliding event on June 3rd at 15:15, the tide level was between high- and low tide. At this time the tide level registered at 171 cm, corresponding to the "mean sea level (1996-2014)", dropping around 60 cm/h (Figure 32).
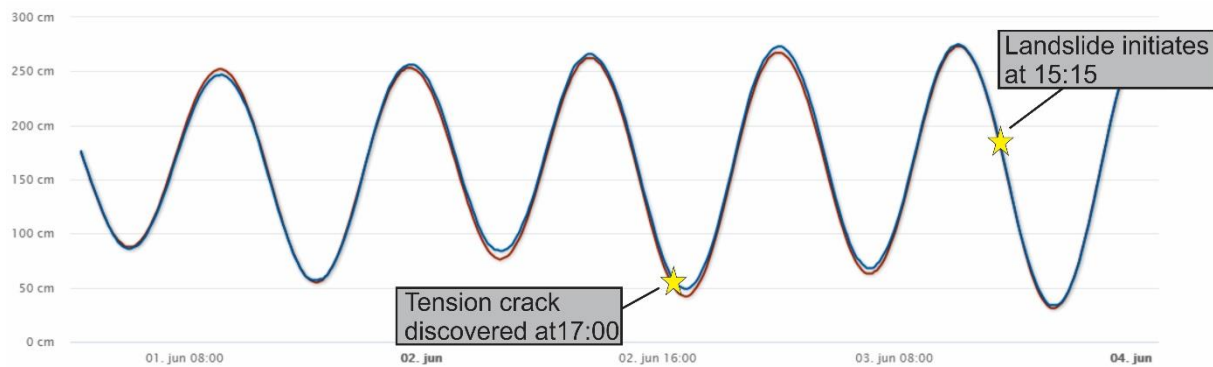
Figure 32: Graph of the tides prior to the landslide. Blue line is the observed tide level from the nearest tide gauge, adjusted for Kråknes. Red line is the predicted tide. The tide level is referenced from the "sea chart datum". Data from https://kartverket.no/en/at-sea/se-havniva.

4.3 Ground conditions

The following section is a description of the ground conditions at Kråknes. The focus has been on describing the characteristics of the area, with an emphasis on the stability reducing factors that have been uncovered. The description of the sediments has been simplified in respect to their characteristics, e.g clay/silt, gravel/sand instead of more detailed descriptions as silty-clay or gravelly-sand. This is due to the safety restrictions of the fieldwork, where most of the sediments had to be identified through images, making it difficult to distinguish the particular fractions of the sediment. The information presented is based on both fieldwork and the ground investigations by NVE and Multiconsult. To simplify the descriptions of the ground conditions, the landslide area has been divided into three areas; A, B and C, respectively (Figure 33). Each area will be presented and described initially, before more detailed data about the ground conditions will be introduced later in the chapter.
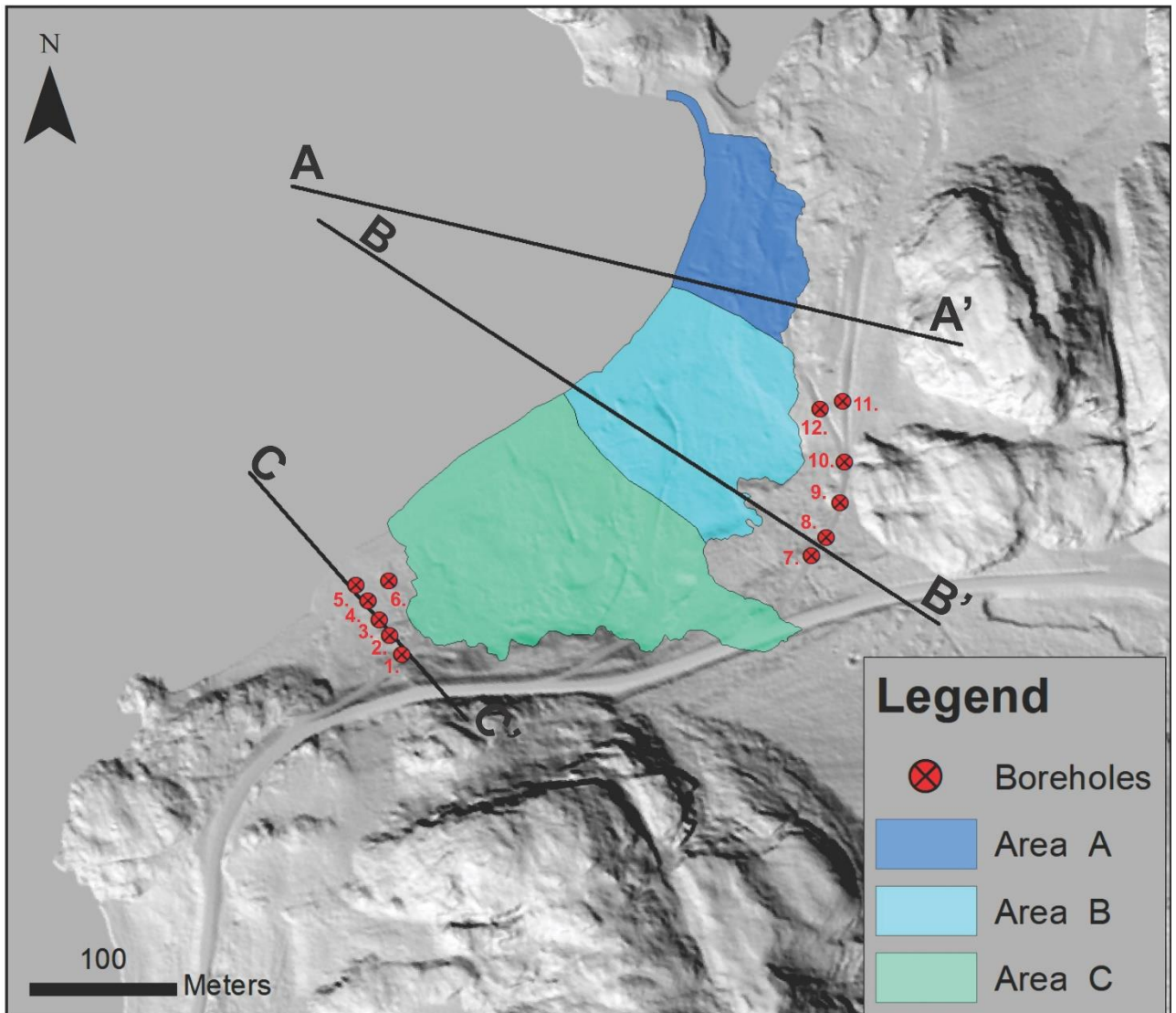
Figure 33: Hillshade relief map of the Kråknes. The landslide has been divided into three separate areas, depending on geomorphology and soil characteristics. Boreholes from ground investigations are marked on the map, in addition to profiles selected for slope reconstruction and stability modeling.

4.3.1 Field observations

4.3.1.1 Area A

The northernmost area of the landslide, defined as area "A", is characterized by a thin layer of clay, sand and gravel, superimposing the bedrock (Figure 34A). The sedimentary strata visible at the scarp is relatively thin, ranging from one to three meters in thickness. The clay was hand tested for sensitivity in the field using the field guide from the New Zealand Geotechnical Society (NZGS, 2005), and determined to be *highly sensitive (*Figure 34B). Field measurements

and approximations made from photos reveal that the bedrock has a dip ranging from 20-25°
NW at the scarp in this area.

Figure 34: A) Photo taken in the NE direction. A layer of sand/gravel is observed above soft clay.
Smaller areas of bedrock are exposed. B) Close-up photo of clay and sand/silt boundary (photos: Anders
Bjordal, June 4th 2020).

Beneath Kråknesveien 416, the sediment thickness remains approximately the same, but the
height and steepness of the scarp changes . At this point, the scarp has a height of about ten
meters, with steeply dipping bedrock exposed at several locations (Figure 35A). The dip of the
bedrock has changed from 20-25° to 25-30° northwest. The sediments exposed are
predominantly clay/silt, superimposed by a coarser layer of sand, gravel and rocks (Figure 35B).
The clay is interpreted to be the same highly sensitive clay as tested further north (it was too
dangerous to physically access this area). One of the more interesting observations of area A
are the drainage pathways observed in the scarp (Figure 35C). The concentration of drainage
pathways reveals that the area has been under the influence of water prior to the landslide. From
Figure 35C, we can observe that water has exited out from the upper part of the scarp, at the
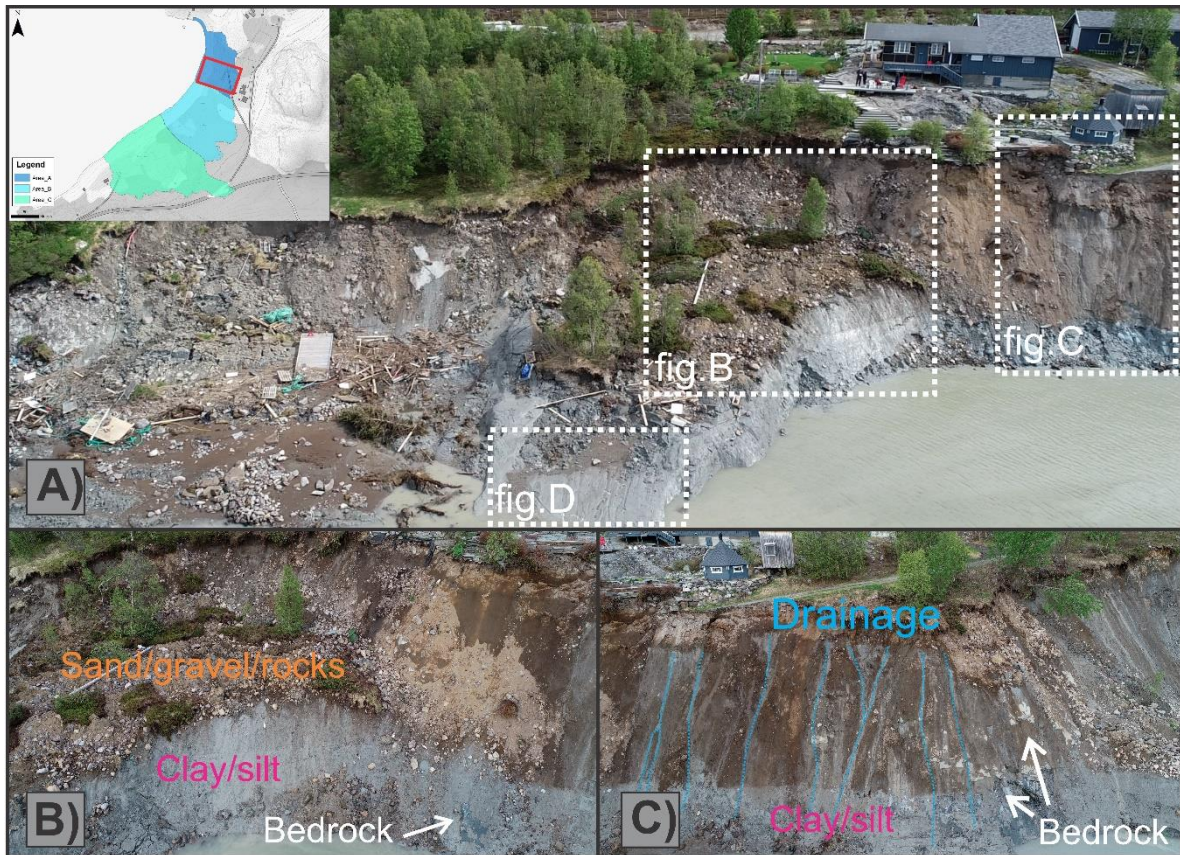boundary between the bedrock and the coarser sediments.

Figure 35: A) Drone photo of the scarp beneath Kråknesveien 416. Photo: Anders Bjordal. B) Thick landslide debris on top of clay/silt. Small patch of bedrock visible next to the water. Photo: Anders Bjordal. C) Visible signs of water drainage in the scarp. Water is interpreted to exit at the soil-bedrock interface. Bedrock is exposed in large parts of the scarp, with a thin veneer of clay/silt on top. Photo:Anders Bjordal.

Three weeks after the landslide, new photos were taken at Kråknes (Figure 36). Here, the water from the upper part of the scarp has dried out, although the impressions from the water can still be observed. Several soil pipe structures were observed at the interface between the clay/silt layer and the coarser material above (Figure 36). The soil pipes have been interpreted as the remains of drainage pipes, and have presumably supplied water from higher eleveation and down to the sea. A developed network of drainage pipes can rapidly transport water from hillslopes, reducing the pore pressure on the slope. However, if these drainage pipes are blocked, excess pore pressure can develop around the pipe due to the hydrostatic head of the water. For slopes at the limit of failure, the added pore pressure from drainage pipes can be sufficient to trigger a landslide (Pierson, 1983).

Figure 36: Photo of scarp three weeks after the landslide. Plumes of fine material indicate possible active drainage pipes, even two-three weeks. Photo: Raymond Eilertsen.

4.3.1.2 Area B

Area B is characterized by a thicker successions of sediment, and less exposure of bedrock when compared to area A. The top sediment layer consists of coarse material, consisting of sand, gravel and rocks. This superimposes a thicker layer of silt and clay, which has been identified from the closest borehole (nr.12, Figure 33). From the drone photos, lenses of coarser material have been identified in the scarp, and marked as blue squares (Figure 37A). These lenses display a darker color than the neighboring sediment, presumed to be the result of higher water content. Similarly, the influence of water can be observed at the bedrock exposure in Figure 37B. Water can clearly be observed exiting beneath the coarse layer on top of the bedrock, comparably to the observation in area A (Figure 35C).
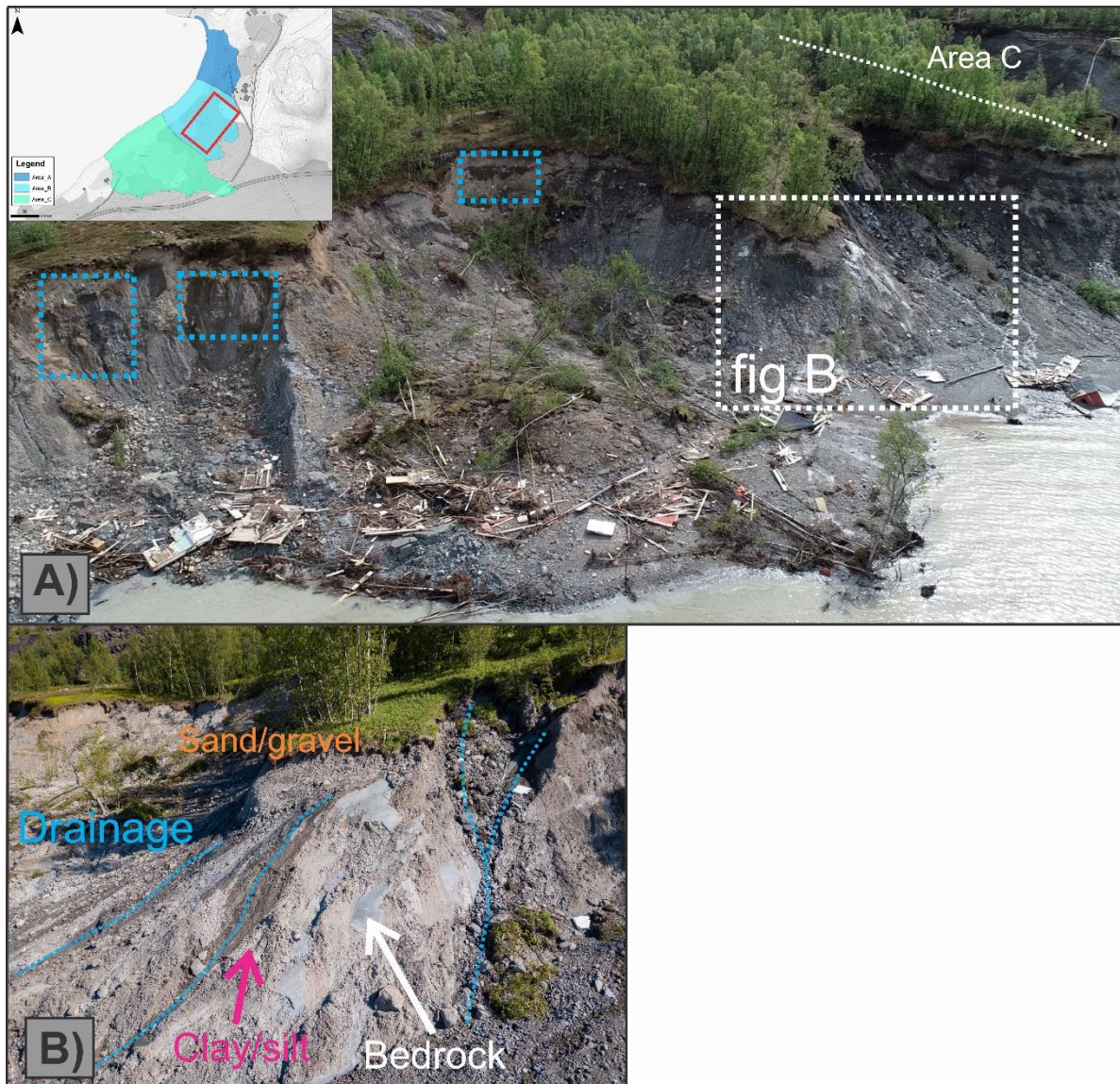
Figure 37: A) Drone photo of Area B. Blue squares indicate the location of lenses of coarser material. Photo: Anders Bjordal. B) Bedrock exposed under a thin layer of sand and gravel. Water can clearly be observed exiting at the boundary between bedrock and sediment. Photo: Raymond Eilertsen.

4.3.1.3 Area C

Area C is characterized by the thickest sediment package of the landslide area. This is also the area where the largest volume of mass has released during the landslide. Four localities will be focused on and presented from this area (Figure 38).

Figure 38: Overview photo from area C. White boxes illustrate the location of figures 39 and 40. Photo: Raymond Eilertsen .

The amount of sediment released from area C during the landslide, has been substantial. This is especially evident at the transect with area B, where the road has collapsed (Figure 39A). Here, the scarp ranges from 10 to 15 meters in height, consisting primarily of unsorted sand and gravel, separated by thinner layers of clay and silt. The gravel displays a distinctive layering, where the layers are dipping towards north, at an angle of approximately 20 ° (Figure 39B). Beneath the unsorted sand and gravel, holes interpreted to be the remains of old drainage pipes are exposed in the scarp (Figure 39C). Compared to the interpreted drainage pipes in area A and B, these are substantially larger, indicating that a significant amount of water must have been transported beneath the surface in this area.
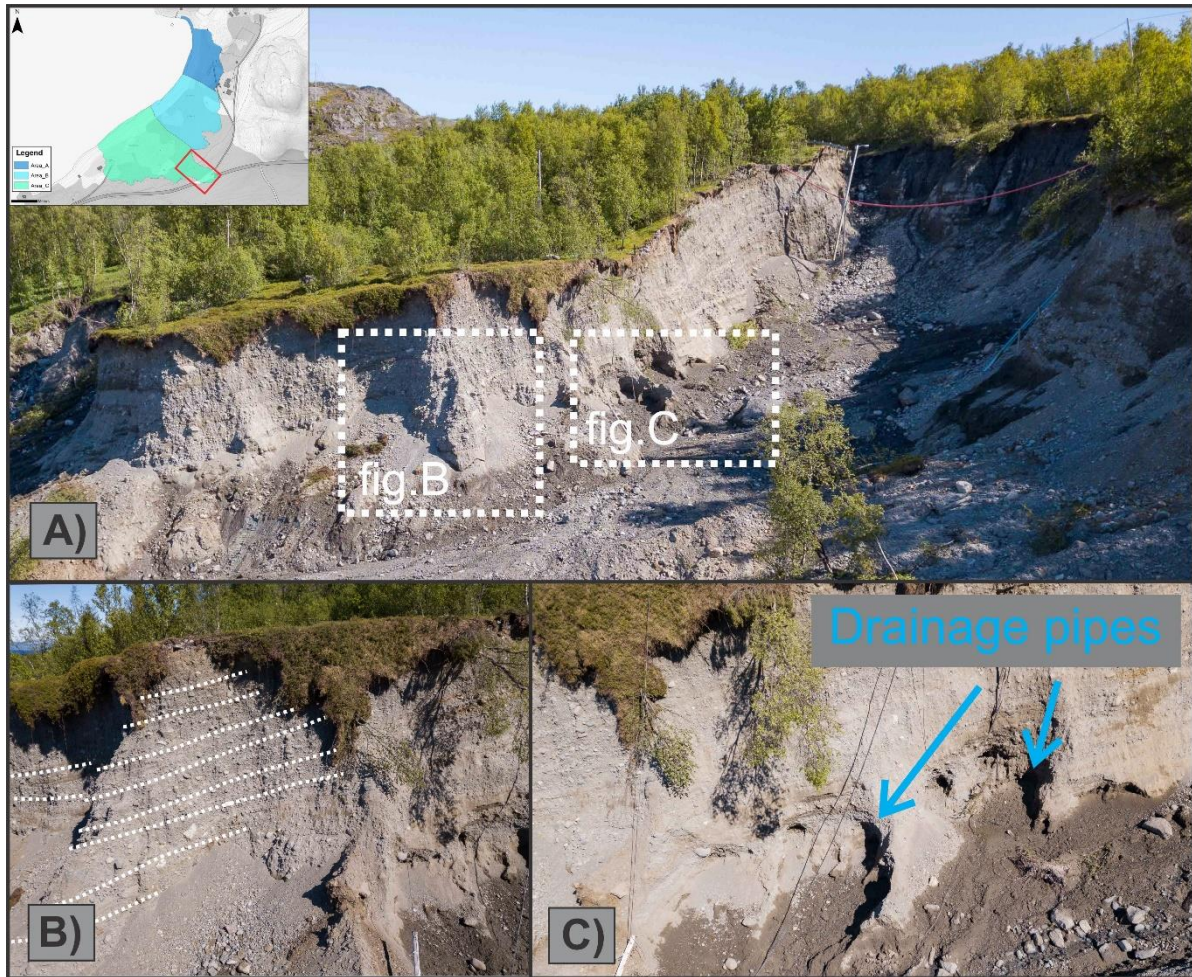
Figure 39: A) Photo displaying the scarp in area C. The scarp ranges from 10 to 15 meters in height, with unsorted sand and gravel being the dominating sediment. The location of figure B and C are illustrated with white boxes. B) Layers of unsorted sand and gravel dipping towards north. C) Drainage pipes exiting the lower end of the scarp, with darker colored sediments that are saturated with water.

Further south in area C, there is a distinct change in sediment composition. The coarse layer of unsorted sand and gravel tapers of, as silt and clay become more dominating. These layers are recognized by the darker color and higher moisture content (Figure 40A). This trend is supported by the geotechnical data, where clay and silt dominate BP 1-6, while sand and gravel are more prevalent in BP 7-11 (Figure 33, Appendix A).
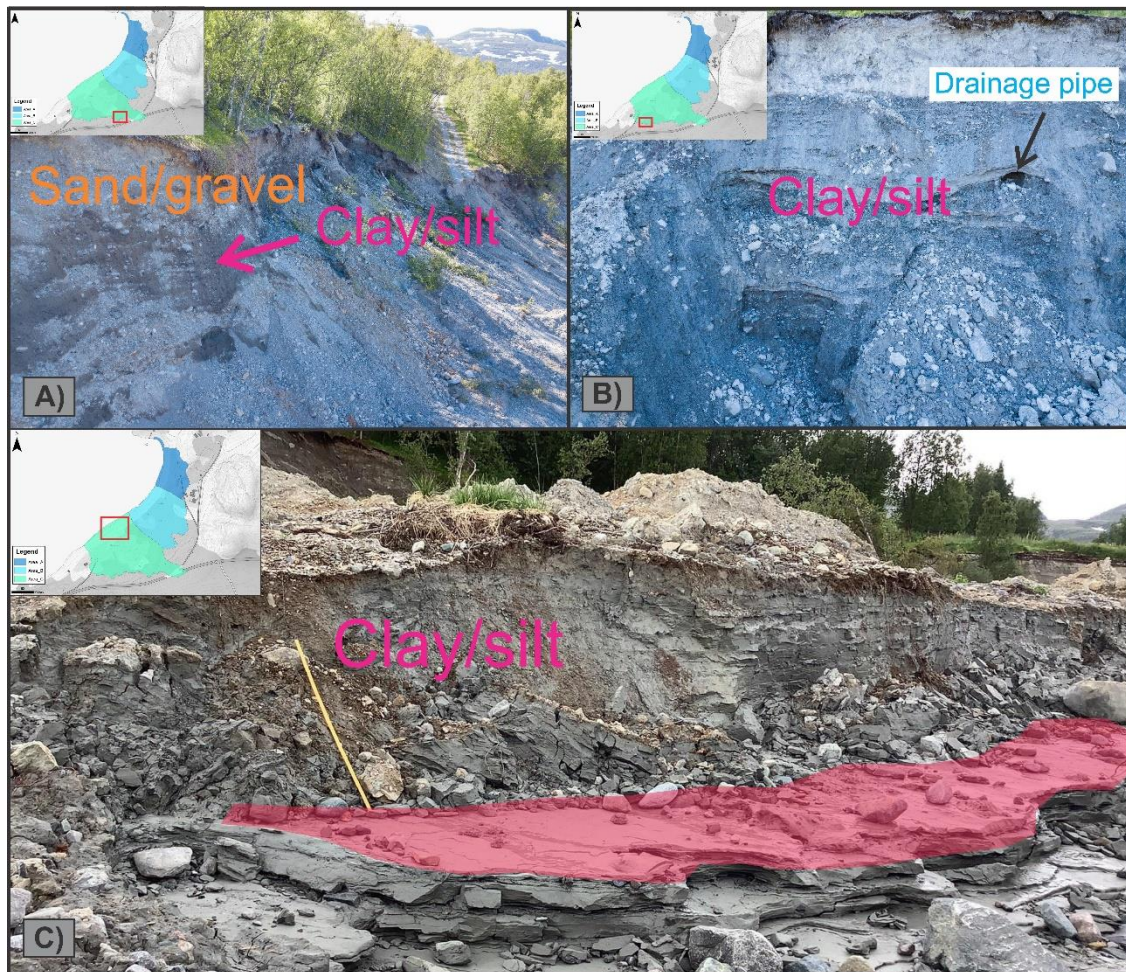
Figure 40: A) Scarp composed of unsorted gravel and sand, with a darker layer of silt and clay visible. The dark color indicates a higher moisture content compared to the surrounding sediment. (Photo: Raymond Eilertsen). B) Scarp composed of silt and clay, with remnants of a drainage pipe exposed. (Photo: Raymond Eilertsen). C) Outcrop of clay and debris which has been transported and deposited during the slope failure. The clay displays a layered stratigraphy with thinner layers of silt separating the clay. Smooth, low-friction surfaces appear where the overlying sediments have been removed, as illustrated by the red color.

The distinctive change in sediment type can be observed in Figure 40B, where the scarp is composed of alternating layers of clay, silt and fine-grained sand. Due to the relative proximity to BP 1-6, it can be inferred that sediments observed in the scarp should reflect the results from BP 2 and 4 (Appendix A). Thus, highly sensitive- and quick clay would be expected in this area. Additonally, remenants of a drainage pipe is visible in the scarp, indicating a widespread and well-established system for sub-surface water at Kråknes, covering area A, B and C (Figure 40B).

56

A thick unit of silt and clay deposited by the landslide was investigated at the shoreline slide (Figure 40C). The clay demonstrated a distinctive layering with surface-parallel layers. Where the coarser silt was removed, smooth surfaces of clay were left behind. Field tests revealed that this clay was *highly sensitive*.

While field-observations and drone-photos give useful information about the general conditions and soil properties at Kråknes, more detailed geotechnical data must be introduced to understand what caused the slope to fail. Hence, the next section will present and interpret the most relevant geotechnical data and combine it with field-observations, to reconstruct the slope before failure.

4.3.2 Interpretation of geotechnical data and slope reconstruction

The reconstruction of the slope at Kråknes is based on the geotechnical data acquired from Multiconsult, combined with field observations. For the reconstruction, three profiles were chosen, based on the failure sequence of the landslide and their proximity to the ground investigations. Due to the limited distribution of the ground investigations, most of the data had to be extrapolated from the closest boreholes. Interpretations of the depositional environment will also be included, although the accuracy and complexity of the interpretation will be limited due to the scope of this thesis.

4.3.2.1 Soil characteristics and interpretation

The geotechnical data from Multiconsult revealed that the sediments at Kråknes exhibited a layered stratigraphy, composed of both coarse- and fine-grained material. Data from the eastern boreholes (BP 7-12), indicated that coarse-grained material with high penetration resistance dominated this area of the landslide. This is also supported by samples taken from BP 12, showing that the top layer of the stratigraphy is composed of a thick layer of sandy gravel (Appendix A).

A layer of sand and gravel is generally found in the upper part of the stratigraphy in BP 7-12. From the total soundings, the layer exhibits a medium penetration resistance of about 5 kN, with a thickness varying from 2 to 7 meters. The characteristics of this layer are compatible with what you would expect to find in a beach deposit. Sand and gravel are the dominant sediments, with the addition of larger pebbles, cobbles and boulders (Figure 41A). In addition,

there is little evidence of silt and clay, which is expected in a beach deposit (Nichols, 2009). This also corresponds well with the quarternary deposits mapped in Figure 5B.

Below the layer of sand and gravel, a layer with a distinctive higher penetration rate (15-25 kN) is identified. This layer is interpreted to be the layered unsorted gravel visible in (Figure 41B). This layer can be identified in almost all the boreholes, suggesting that the layer covers most of Kråknes. The thickness of the layer ranges from 3 to 19 meters, fitting well with the observations from the field. The distinctive layering of the gravel can be recognized on the total sounding data as alternating penetration resistance, further supporting the observations from the field.

Additionally, some of the pebbles in the scarp show signs of imbrication, indicating a fluvial environment Figure 41B. The larger clasts are observed to be sub-angular to sub-rounded compared to the more rounded clast of the superimposing beach deposits. As a result, a different depositional environment is expected. Taking the glacial history of Kråknes into account, this layer has been interpreted to be a glaciofluvial deposit.
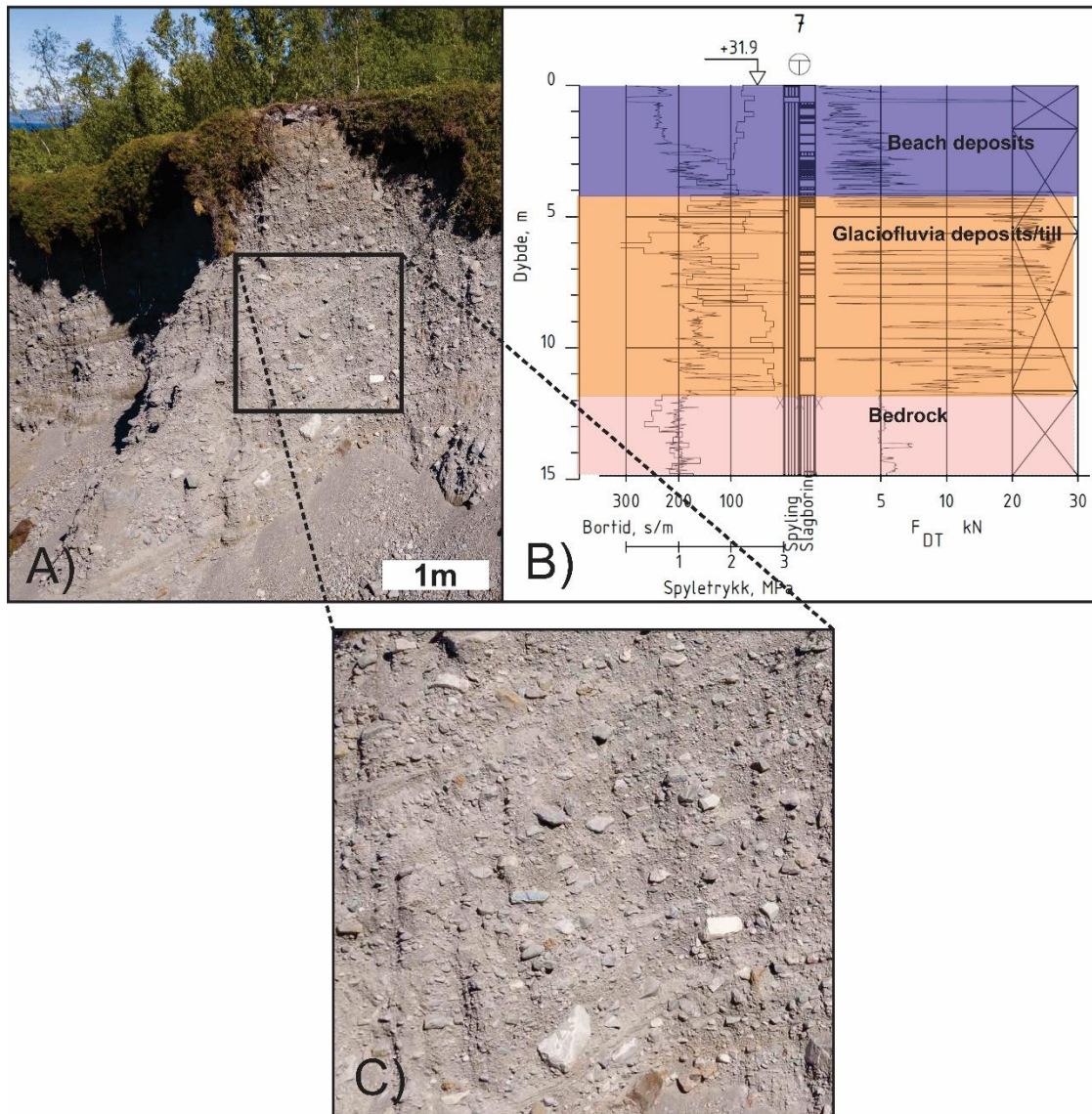
Figure 41: A) Photo of the layered unsorted gravel layer at the scarp. B) Interpreted total sounding data from the closest borehole (BP7). C) Close-up of the layered gravel. Clasts are observed to be sub-rounded to sub-angular, and show signs of imbrication.

Beneath the glaciofluvial deposits, the alternating layer of clay and silt is found (Figure *42*A). The layer varies in thickness from 2 to 17 meters in the boreholes, but is interpreted to be thicker in the central part of area B. The composition of the material is predominantly clay, with alternating amounts of silt, as supported by the sample classifications by Multiconsult (Appendix A). The clay and silt shows an apparent stratification, where thin layers of silt separates the clay. This has been interpreted to be a marine deposit, which has been exposed to the surface by the isostatic uplift. In some areas of the scarp, coarser lenses of sand and gravel are observed to cut the finer layers of clay and silt. These layers can be recognized by higher

penetration resistance in the total sounding data, and is interpreted to be glaciofluvial deposits that have been deposited under periods of greater meltwater levels (Figure 42A).
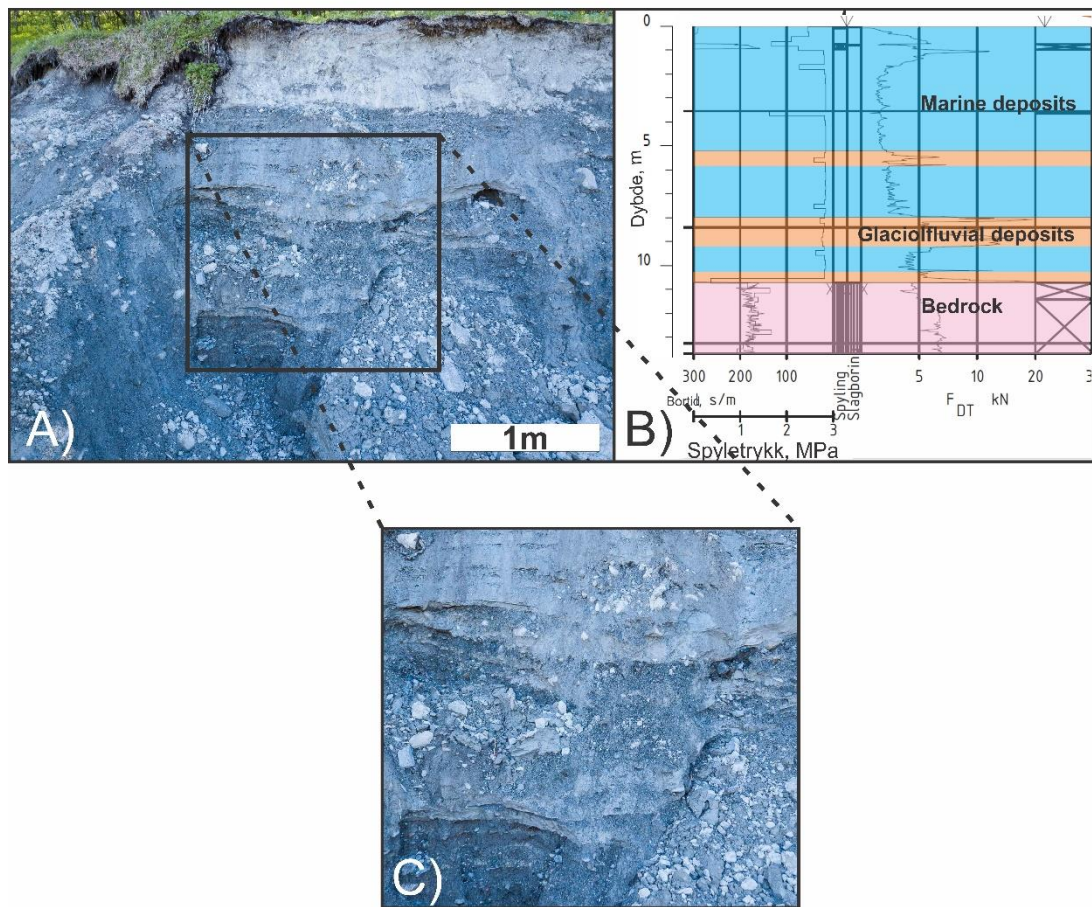

Figure 42: A) Photo of the clay/silt-layer interpreted to be a marine deposit. B) Interpreted total sounding data from the closest borehole (BP2). C) Close-up, showing the layered stratigraphy of clay and silt interrupted by coarser sediment.

For reconstructing the slope, we are interested in the general stratigraphy of the slope, as well as the layers that have a specific influence on the stability. Since sensitive clay landslides often are triggered by an increase in pore pressure, more permeable layers are of interest to identify. In Figure 43 and Figure *44*, permeable layers have been identified and marked on the figures. These layers are identified by an abrupt decrease in pore pressure (u), and a corresponding increase in cone resistance (q_c) and sleeve friction (f_s).

From BP2, five permeable layers were identified (Figure 43). These layers range from 10 to 30 cm in thickness, presumably consisting of a mixture of sand, silt and gravel. This is based on the sample classifications by Multiconsult, where one of the core samples overlap the location

of a permeable layer. From the samples collected, we can observe that the general composition of the soil at BP2 is predominantly clay and silt with smaller amounts of gravel. Lab tests reveal that the clay exhibits a sensitivity (s_t) between 8 and 16, and remolded shear strength ranging from 0.8 to 1.3 kPa. However, the values satisfying the requirement for sensitive clay is only found between 8 and 9 meters depth (Appendix A). It can be observed that the location of sensitive clay overlaps a more permeable layer indicating a possible connection.
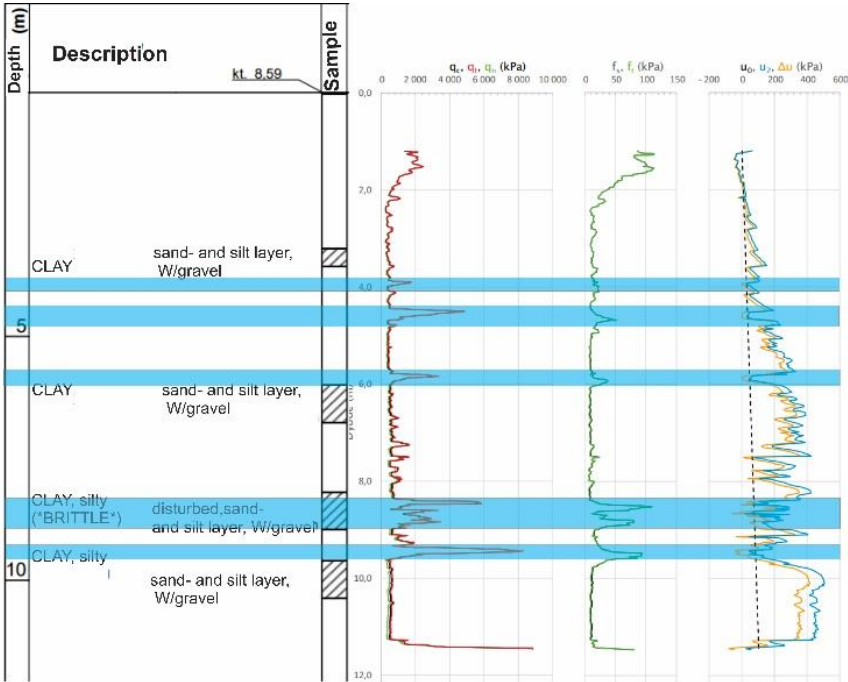

Figure 43: Figure showing the depth and description of samples collected in BP2. The graphs to the right are the corresponding CPTU-data, showing cone resistance (q_c), sleeve friction (f_s) and pore pressure (u). Blue lines indicate more permeable layers. Figure adapted from Waldeland (2020).

At BP4, the sediment thickness has increased by four meters compared to BP4. Along with the thicker sediment, more permeable layers have been identified, increasing from 5 to 7 (Figure 44). Although the permeable layers have increased in numbers, it must be taken into account that the overall variation in the dataset for BP4 is far less than for BP2. This means that the values required for interpreting a layer as permeable in BP2 is higher than BP4, suggesting that some layers may have been excluded in BP2. Comparing to BP2, the values from the CPTU are more uniform, with q_c and f_s showing fewer spikes. It is also apparent that the permeable layers have become thinner (5-10 cm), indicating that these layers thin out in the down-slope direction.

Similarly as for BP2, soil samples were tested for sensitivity (s_t) and undrained shear strength (c_u). These results combined with the CPTU-test show that sensitive- and quick clay is located between 8 and 15 meters in BP4. Although the data from the CPTU is valuable, the majority of the ground investigations at Kråknes were done by total sounding. As a result, the data from the total soundings must be taken into account when reconstructing the slope stratigraphy.
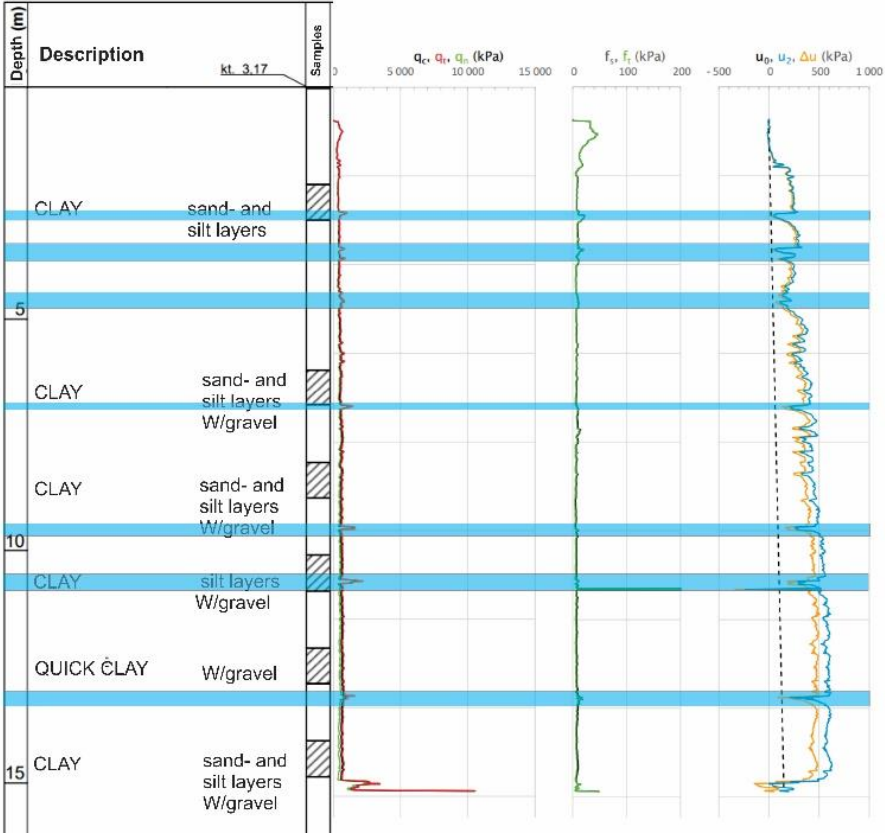

Figure 44: Figure showing the depth and description of samples collected in BP4. The graphs to the right are the corresponding CPTU-data, showing cone resistance (q_c), sleeve friction (f_s) and pore pressure (u).Blue lines indicate more permeable layers. Figure adapted from Waldeland (2020).

A schematic of the slope profile and locations of BP 1-5 are shown in Figure 45. Despite the fact that total sounding is more rudimentary than CPTU, it is possible to estimate the location of permeable layers by the increased penetration resistance and their concurrent location from CPTU-data. As a consequence, four layers where interpreted to follow the entire length of the slope, for BP 1-5 (Figure 45). From this, sedimentary layers were interpreted in respect to depositional environment, and the following profiles were constructed.
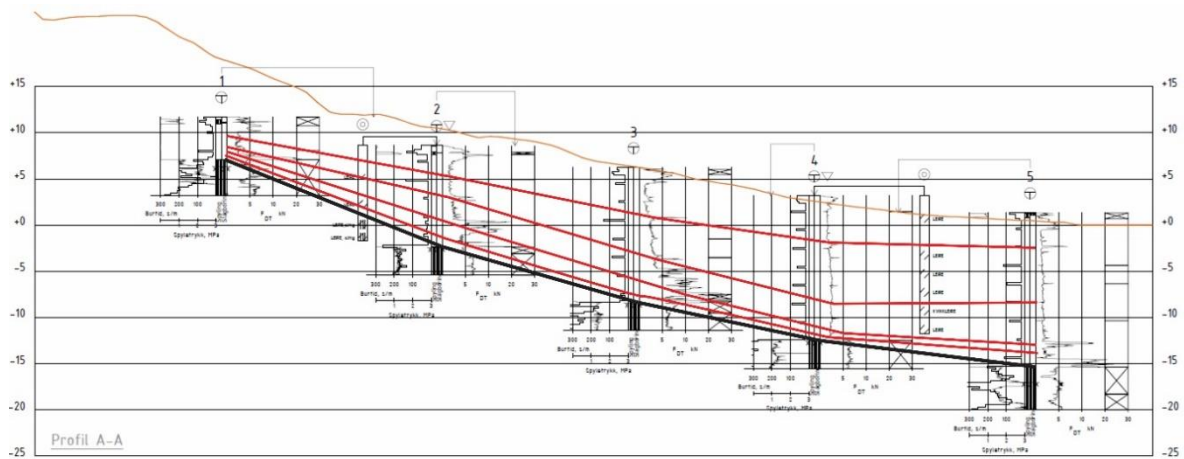
Figure 45: Profile of total soundings from BP 1-5. Slope geometry is represented by the yellow line, and elevation contours are listed on the y-axis. Red lines are drawn on to illustrate the location of permeable layers. The bedrock interface is represented by the black line. Adapted from (Waldeland, 2020).
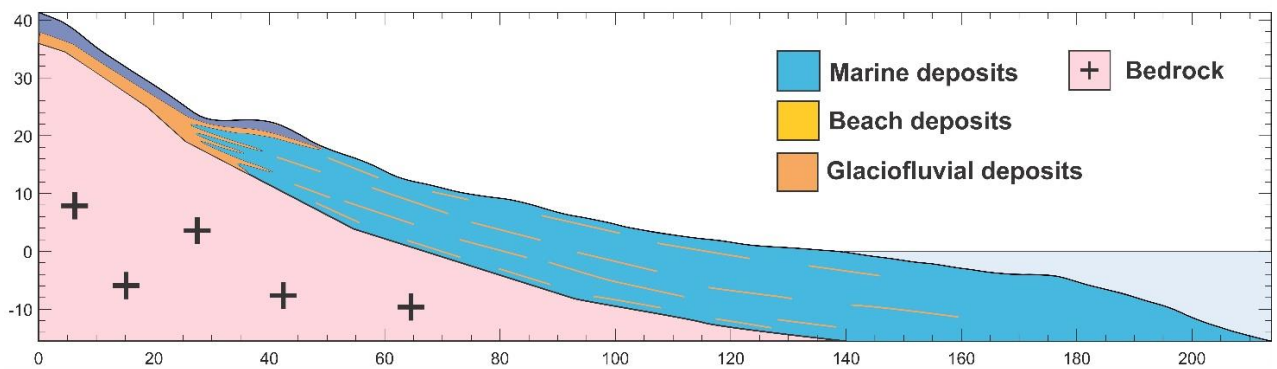

Figure 46: Profile C-C': Geological profile based on the CPTU- and total sounding data from BP 1-5.
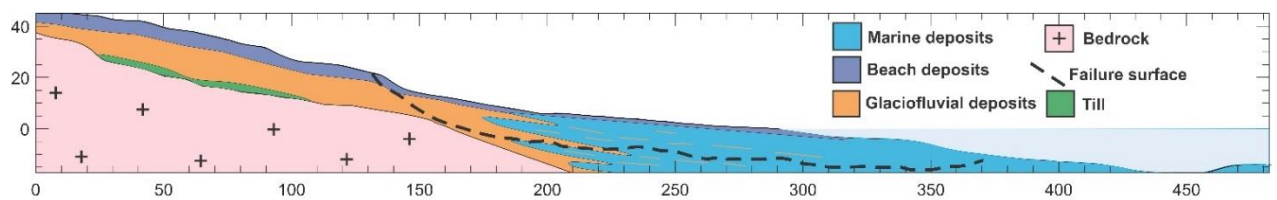

Figure 47: Profile B-B': Geological profile from the area expected to have the thickest sediment cover. The failure surface on the profile is based on the LiDAR- and bathymetry-data from after the slide.
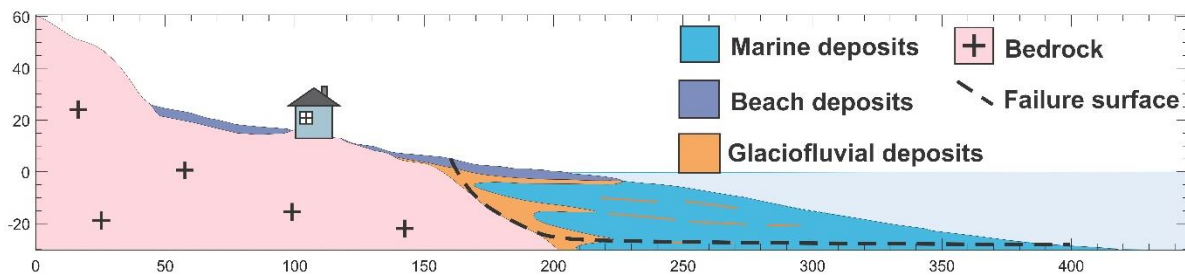
Figure 48:Profile A-A'. House where local observed the initiation of the landslide is drawn on the profile (house not to scale). The failure surface on the profile is based on the LiDAR/bathymetry-data from after the slide.

4.3.3 InSAR and seismic activity

InSAR-data from Kråknes is presented in Figure 49. The data shows little overall displacement at Kråknes over the last five years, with an average displacement of 3-5 mm/yr. Apart from the average, single points have registered displacement up to 20 mm/yr in the SW corner of the landslide area. In general, the area exhibits poor data coverage, especially where there has been human activity. As such, there remains uncertainties related to their reliability of this data.

Additionally, seismicity was investigated preceding the event. The data registered at NORSAR revealed little activity that could be connected to the slope failure at Kråknes, where the closest registered measurement happened at the 25th of May in Finland, with a magnitude of 1.38, presumably connected to mining activity (Appendix B).
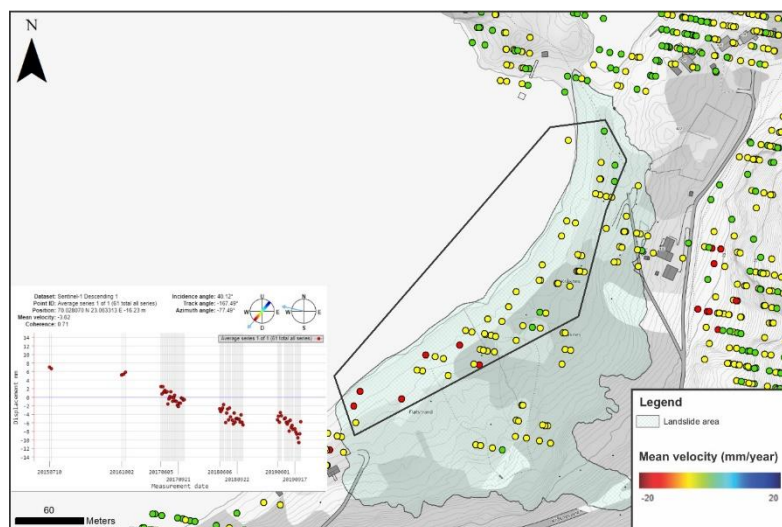

Figure 49: Topographic map of Kråknes with the landslide area overlaid (Kartverket, 2020). Colored dots represent InSAR reflector points. The diagram to the left displays the average displacement from 2015 to 2019, registered by the InSAR reflectors inside the black polygon (NGU, 2020b).

4.3.4 Subaqueous morphology

A topographic map of the seafloor from before and after the landslide at Kråknes is presented in Figure 50. The seafloor-map from before the landslide is covered by hydrograph-5204 from 2004 (1 meter grid) for the shallow section, while the deeper sections are covered by _nhs-0598 from 1998 (5 meter grid). These datasets were later mosaicked together with LiDAR-data. After the landslide, the surface- and seafloor terrain was mapped in detail by GeoNord Survey team (Alta) (Multiconsult, 2021).
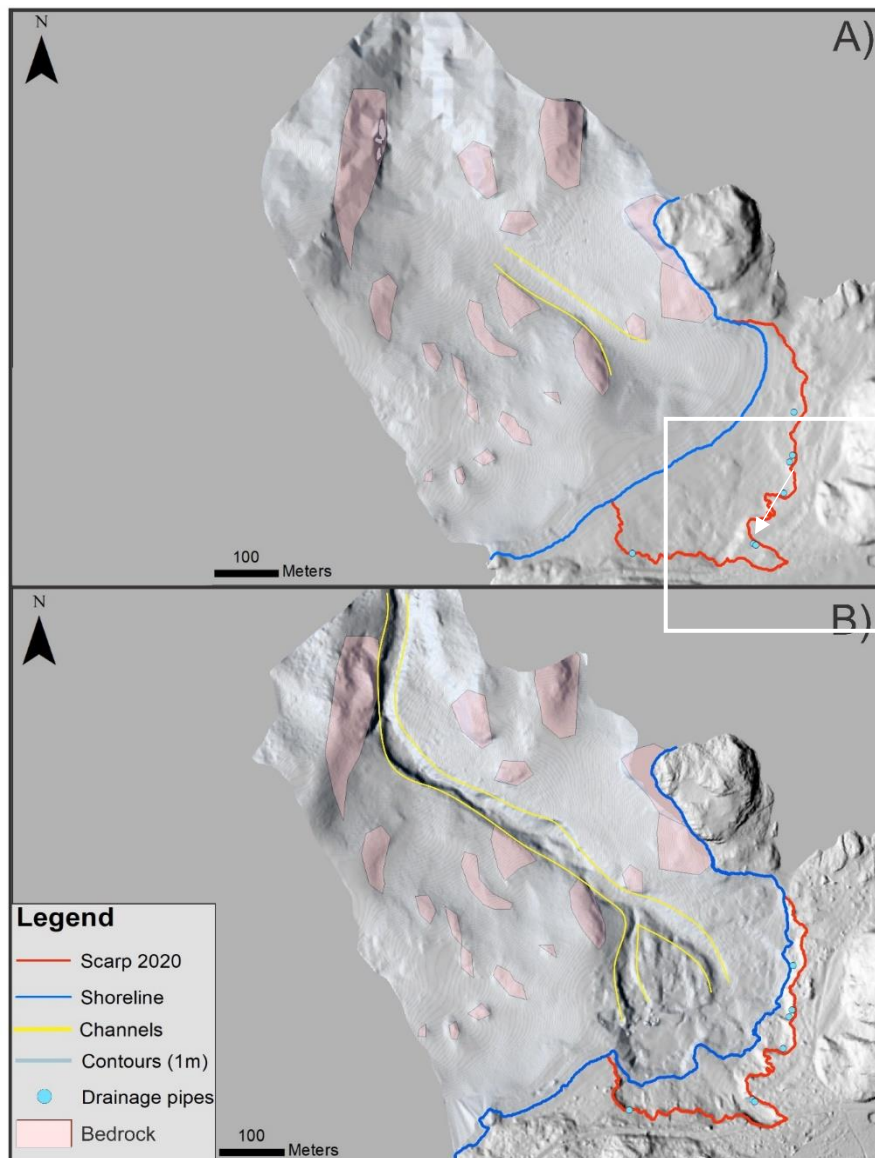

Figure 50: Maps based on LiDAR and bathymetry data, illustrating the subaqueous geomorphology from before and after the landslide. Scarp, shoreline (0 m), subsurface-channels and interpreted drainage pipes are marked on the maps. A) Map of the pre-slide geomorphology, white arrow indicates the location of the small bulges that were observed.

The seafloor from before the landslide had a varied and undulating topography. Steeper areas and protruding "lumps" have been interpreted to be exposed bedrock, while smooth surfaces are interpreted to be covered with sediment. Just outside of the NE part of the landslide, the topography forms a "bowl"-shape, marked by the white square (Figure 50A). Inside of the bowl, the seafloor bulges out in some areas, which could be due to exposed bedrock or remnants of smaller slides. Alternatively, the bulging could be caused by the mobilization of sediment caused by the drainage pipes identified earlier. Below the bowl, a channel is visible. This channel feeds out from the bottom of the bowl, and stretches out approximately 240 meters to the NW, with a depth ranging from 5 to 10 meters. Although it is difficult to predict what caused the channel to form, it can be suspected that a prehistoric sliding event may have played a part. This will be described in more detail in section 4.3.7.

After the landslide, most the bowl-shape was destroyed and replaced by a rougher and more gently dipping surface (Figure 50B), consistent with the morphology of a translational slide (Figure 12B). In addition, two smaller channels have appeared above the original channel, presumably as a result of the sediment flow during the landslide. The sediment from the landslide followed the old channel, consequently deepening and elongating it. In total, the channel increased from 240 to 650 meters in length, and from 5 to 10 meters in depth. This shows that the sediment flow had an erosional effect on the seafloor, proving that most of the sediment must have been deposited beyond the limits of the dataset (Figure 50B).

4.3.5 Bedrock

The large-scale bedrock structures at Kråknes have been mapped with Lidar, showing faults striking ENE-WSW to NE-SW, with a fall predominantly to the NW (Figure 4C). As observed from B/C, the bedrock is influenced by joints and fractures. Some of the more fractured areas (Figure 51C), generally correspond to the larger faults that were identified by LiDAR (Figure 4C). Given a well-developed network of faults, fractures and joints, groundwater flow could be facilitated into the landslide area.

In addition to faults and fractures, the aspect of the bedrock and ground surface can influence the transport of water. This can be compared with rain hitting the ridge of a roof, where water will be transported down the side of the roof of where it landed. As a consequence, the aspect of the ground surface can channel water into specific areas, and should therefore be considered

when investigating the causalities of the landslide. Ground surfaces with aspects ranging from north to west are highlighted in Figure 51A. These aspects have been considered to be the most significant for channeling water towards the landslide area at Kråknes. The aspect map revealed that the mountains surrounding Kråknes demonstrate an aspect that will channel the water towards the landslide area. This is further supported by the observation of water exiting the scarp at the bedrock and soil interface, suggesting that groundwater follows the bedrock surface (Figure 35C, Figure 37B).
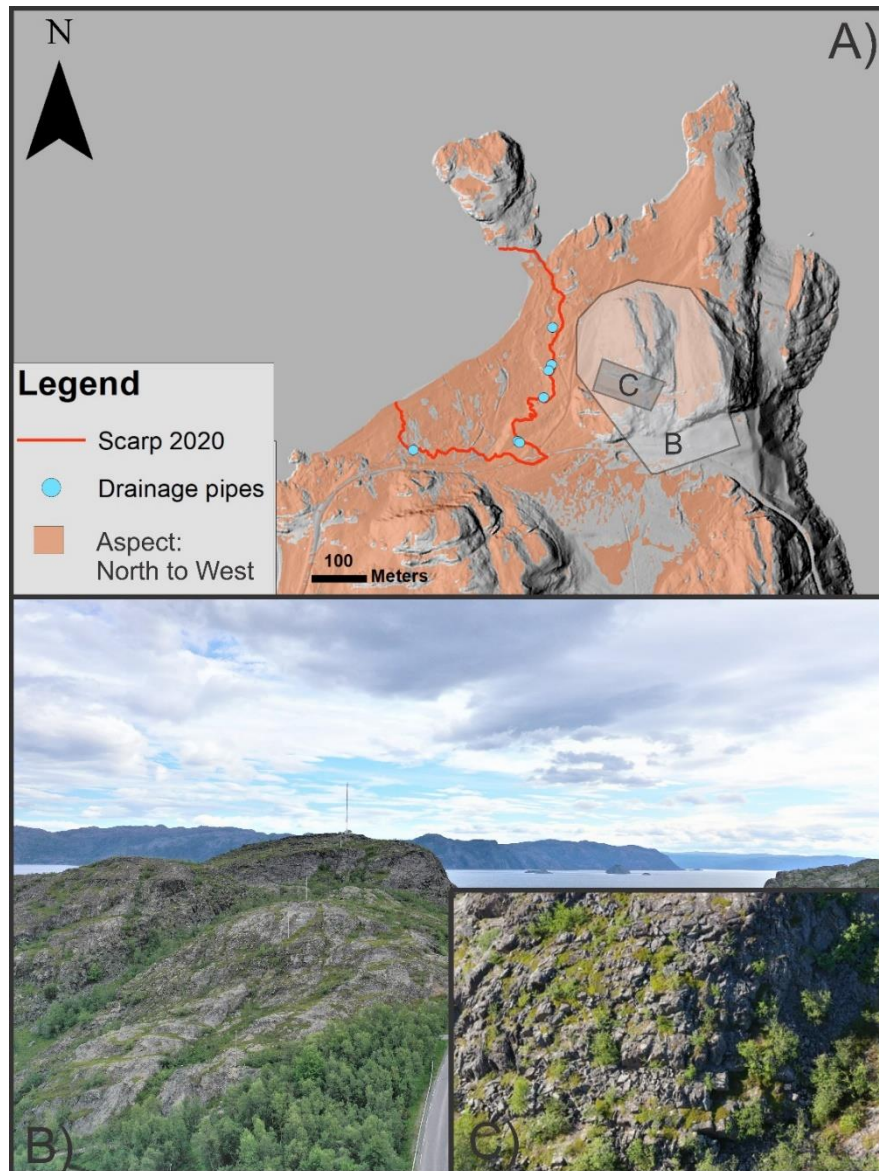

Figure 51: A) Hillshade topography illustrating the aspect of the bedrock and ground at Kråknes. Aspects between North and West have been highlighted (red) as they potentially channel water towards the landslide area. Locations of Figures B and C are shown as grey polygons. B) Drone photo of the bedrock at Kråknes. C) Close-up photo of the fractured bedrock found at Kråknes.

4.3.6 Surficial water and erosion

Signs of surficial water and erosion have been mapped at Kråknes (Figure 52). The aim of the mapping has been to determine the extent of water-related characteristics, such as surficial water, erosion, and old drainage paths. The mapping was done by a combination of fieldwork and reviewing drone photos.

Mapping of drainage pathways in the landslide area revealed that water has influenced all areas of the landslide, from Area A in the north to Area C in the south (Figure 52A). However, the mapping demonstrated an unbalanced distribution, with Area C exhibiting a higher density compared to the other areas. This is likely due to the topography of the surrounding area, channeling water more effectively towards this section. Similarly, signs of surficial water was observed from drone photos taken two days after the landslide initiated (Figure 52B). This suggests that the area southeast of Area C was completely saturated with water in the days before the landslide, which is supported by soil saturation models by Xgeo.no (Figure 31). In addition, visible signs of erosion were observed next to Kråknesveien during field investigations (Figure 52C). As observed, the ditch has been eroded 15-30 centimeters, indicating high water flow.

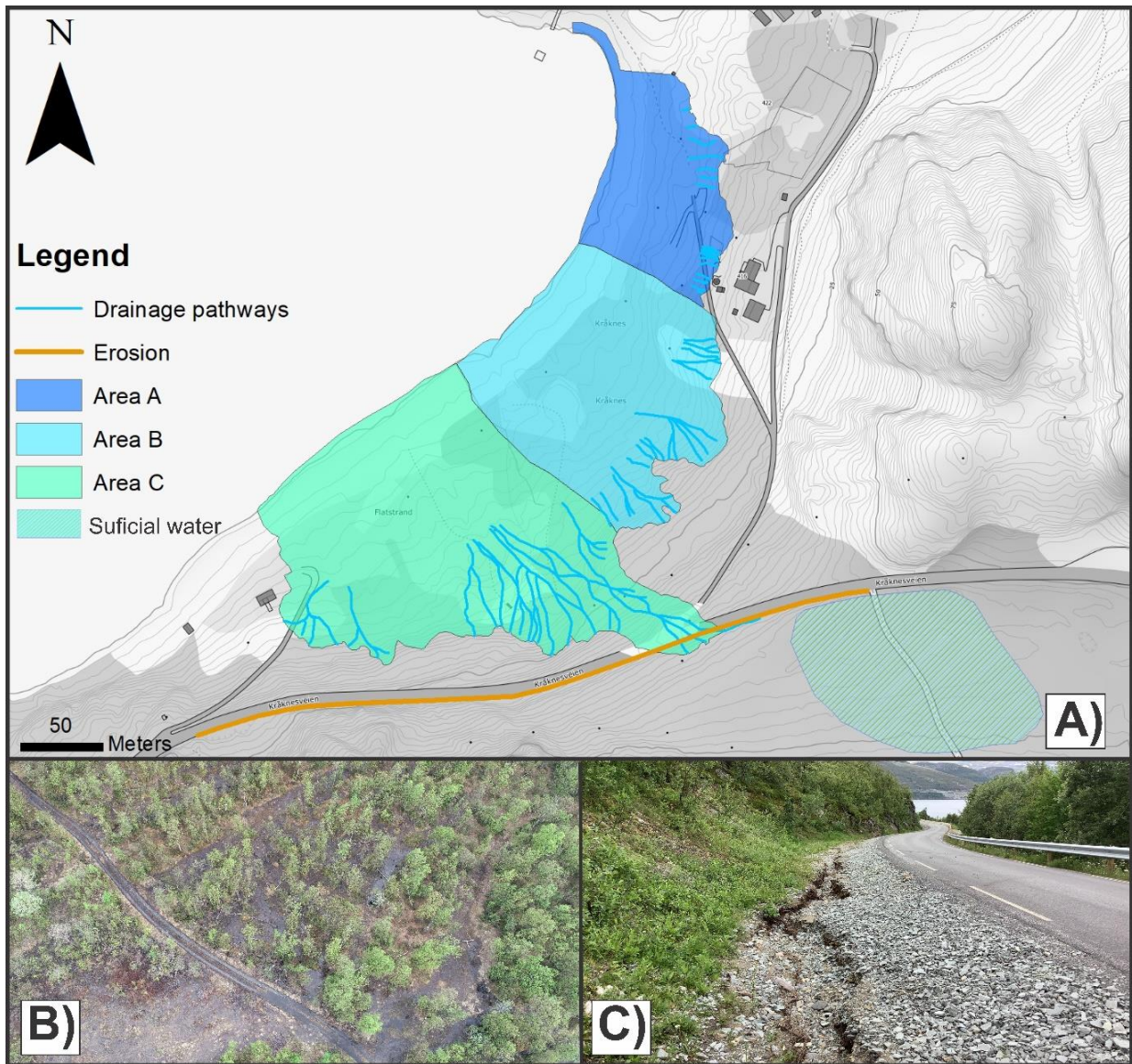Figure 52: A) Mapped drainage pathways, surficial water and erosion at Kråknes, overlain a topographic map (Kartverket, 2020). B) Drone photo of surficial water. The ground in this area is completely saturated, with darker-colored areas being covered by water (Photo: Anders Bjordal, 05.06.2020). C) Visible signs of erosion of next to Kråknesveien. This photo is taken just below the area where the road collapsed.

4.3.7 Historical events at Kråknes

A prehistoric landslide scarp is identified in the pre-2020 landslide event lidar data (). The scarp follows a similar alignment to the current landslide scarp around the bay with an elevation of approximately 30 meters. The identification of a prehistoric scarp indicates that a landslide event has taken place at Kråknes in the past, and that the landslide in 2020 might be the most recent in a series of events. Due to the scarp not being dated, it is difficult to determine when the prehistoric landslide might have happened. However, the lack of raised beach ridges within the landslide area suggests that the scarp is relatively young (Figure 5B), and the event may have occurred in the last 1000 years, as supported by (Multiconsult, 2021).
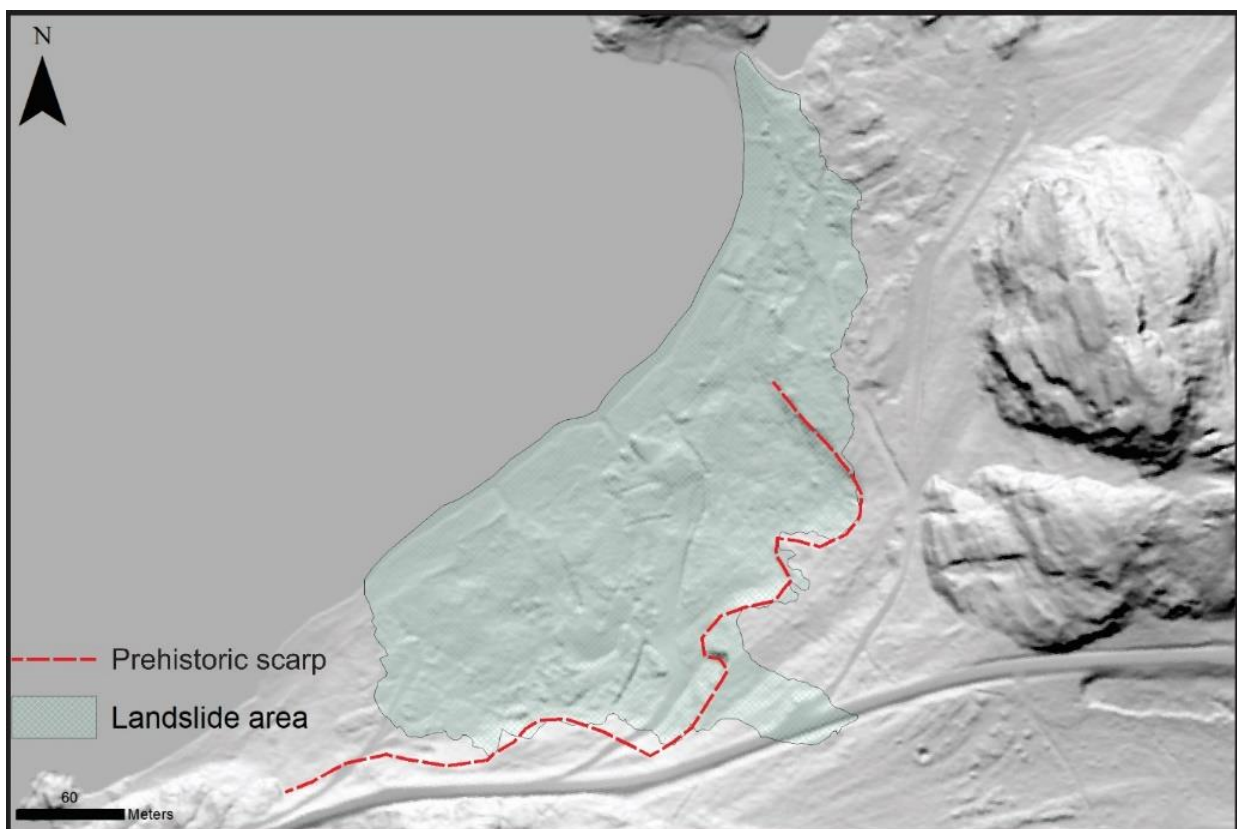

Figure 53: Hillshade topography of Kråknes based on 1 metetr resolution digital elevation model (Source: Kartverket.no). Prehistoric scarp (red) overlain the landslide area from 2020.

4.4 Human activity

The information about the influence of human activity at Kråknes has been acquired through an interview with a local resident, and information disclosed in the report by NVE (Multiconsult, 2021). As a result, four situations of human activity have been investigated, and will be presented accordingly.
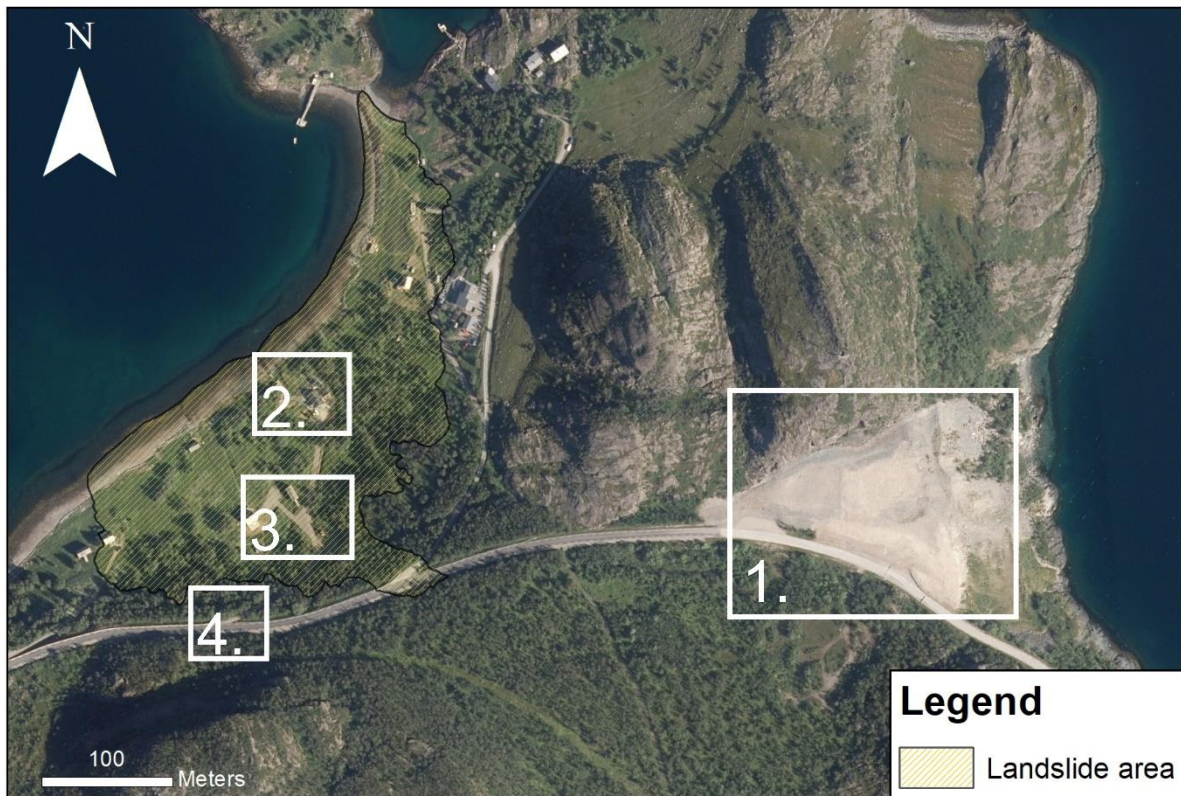
Figure 54: Overview map of human activities before the landslide. The numbers indicate the location of the different activities. 1) Landfill. 2) Ground work for cabin building. 3) Mass relocation. 4) Road work.

4.4.1 Landfill

During the construction of the new E6 Alta Vest in 2015, a landfill was built on the eastern side of Kråknes (Figure 54). The landfill covers an area of approximately 230 x 150 meters, with an average thickness of around 6 meters. The landfill material consists mainly of silt, sand and gravel. Smaller lobes of material on the eastern side of the landfill suggest that material has released from the side of the landfill.

4.4.2 Cabin building

In 2015, a new cabin was built at Kråknesveien 450. Due to the soft ground conditions at the cabin location, new material was deposited to stabilize the ground (Figure 55). In total, 80 truck-loads of crushed stone (1000-1200 m^3) were deposited at the location (Multiconsult, 2021). According to the cabin owner, the material was predominantly acquired from the landfill east of Kråknes (Figure 54). At the same time as the cabin was built, the road to the property was upgraded. In addition, a septic tank was installed for the cabin. According to the contractor

responsible for the installation, the ground consisted of mostly fine-grained materials, believed to silt and clay (Multiconsult, 2021).

Figure 55: Photo of the groundwork associated with cabin building in 2015 (Photo: Vidar Heitmann).

4.4.3 Mass relocation

At the same time as the cabin was built, another project involving mass relocation took place at Kråknes. As seen from Figure 56, mass was removed from a small hill, and used for leveling the ground on the eastern side of the white house. The total amount of mass that has been relocated is unclear. However, reports suggest that the filling around the house is about 0.5 meters thick on average (Multiconsult, 2021).

Figure 56: Bottom right corner shows where mass was removed. This mass was used for leveling the area east of the white house, and repairing the road. (Photo: Vidar Heitmann).

4.4.4 Roadwork

After the construction of the new E6, The Norwegian Public Roads Administration upgraded parts of Kråknesveien (Figure 57). New tarmac and railings were added, and the gutters were cleaned. There were no new culverts installed in the section above Kråknes (Multiconsult, 2021). It is also apparent that the road became narrower after the upgrade.

Figure 57: A) Aerial photo of Kråknesveien in 2011. B) Aerial photo of Kråknesveien in 2018, after the road was upgraded. (Source: Norgeibilder.no).

4.5 Slope stability modeling

For slope stability modeling, three profiles were chosen to be modeled in Slide2 (Figure 58). The profiles are based on the geological profiles in chapter 4.3.2, but have been simplified with respect to the thickness and geometry of certain layers, due to the geometry limitations of the modeling software. The purpose of the modeling has been to determine the effect changing groundwater levels and excess pore pressure has had on the stability at Kråknes. In addition, stability modeling was undertaken to determine the possible effect of the cabin building in chapter 4.4.2. The purpose of the chosen profiles will be described briefly next.
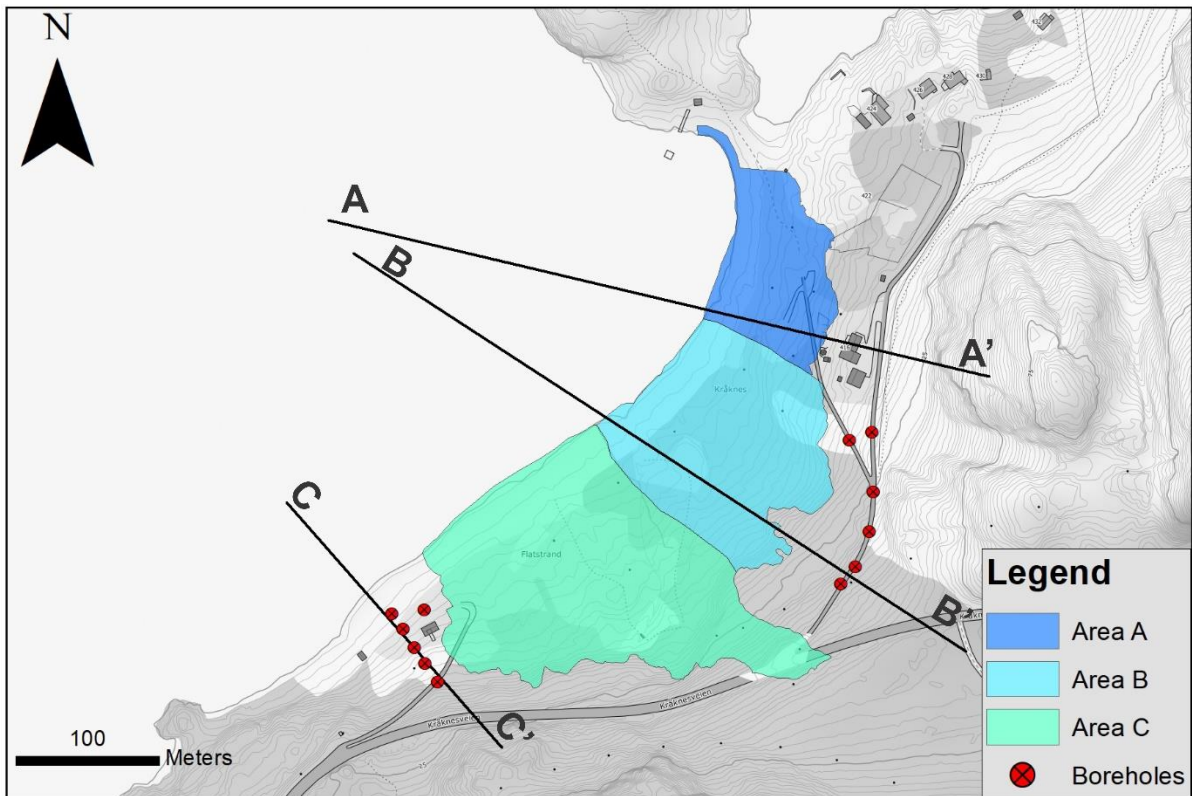
Figure 58: Topographic map of Kråknes illustrating the location of the profiles used for slope stability modeling. (Kartverket, 2020).

➢ *Profile A-A'* is located across the area where the first sliding activity was observed.

➢ *Profile B-B'* represents the central part of the landslide, and where the thickest sediment deposits are expected. In addition, this profile covers the area where the cabin was recently built (4.4.2), and thus incorporates the effect the cabin-building might have had on the slope (B).

➢ *Profile C-C'* represents the area with the most accurate geotechnical information. Material thickness and geometry of this profile are interpreted from the ground investigation. Hence, large parts of Profile A-A' and B'B are extrapolated from this data.

The stability modeling for this thesis was carried out for undrained conditions. This has been based on the hydrogeological data uncovered in chapter (4.2.3), where the effects of snowmelt is presumed to have saturated the ground at Kråknes. Given the short timeframe from the start of the snowmelt to the failure initiated, undrained conditions were expected to be the most probable. As such, the marine deposits were modeled with the "Undrained (Phi = 0)" model in Slide2. For the more permeable beach- and glaciofluvial sediments, the Mohr-Coulomb model
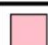
was used to simulate drained conditions. For more information about the different strength models, see (Rocscience, 2021b).

The geotechnical parameters used for the modeling are listed in Table 2, and are based on the parameter interpretations by Multiconsult (Appendix B). The marine deposits have been modeled with a C_u (cohesion) of 16 kPa at the top of the layer, increasing with 3.2 kPa per meter, until a maximum value of 45 kPa. This corresponds with the interpreted values from BP 4, which exhibited the lowest undrained shear strength of the area, and subsequently the lowest expected stability (Appendix B). Hence, the stability modeling will account for the most unstable scenario.

To model the effects of changing groundwater levels and excess pore pressure, three different settings were used: Low groundwater (-5 meters), high groundwater (at surface) and excess pore pressure (+ 10 meters). In addition, the loading effect of the fill material deposited during the cabin construction was modeled, were the dimensions were estimated from Figure 55.

As a basis for the modeling results, the failure surface for profiles A-A' and B-B' have been added (Figure 59A/B). The failure surfaces are extracted from the post-slide LiDAR- and bathymetry data, and thus represents the actual failure surface from the field. For profile A-A', the failure surface measured 265 meters in length and approximately 10 meters in depth. Similarly, the failure surface for profile B-B' measured 250 meters in length and 10 meters in depth. This data will prove as a benchmark for the modeling results, which will be discussed in chapter 5.

Table 2: Table of the soil- and modeling parameters used for the slope stability analysis.

Material Name	Color	Unit Weight (kN/m3)	Strength Type	Cohesion (kPa)	Phi (deg)	Cohesion Type	Cohesion Change (kPa/m)	Cutoff (kPa)
Beach deposits		18.8	Mohr-Coulomb	10	38			
Glaciofluvial deposits		19	Mohr-Coulomb	3	30			
Marine deposits		19	Undrained	16		FDepth	3.2	45
Bedrock		24	Infinite strength					
Fill material		18.8	Mohr-Coulomb	10	35			
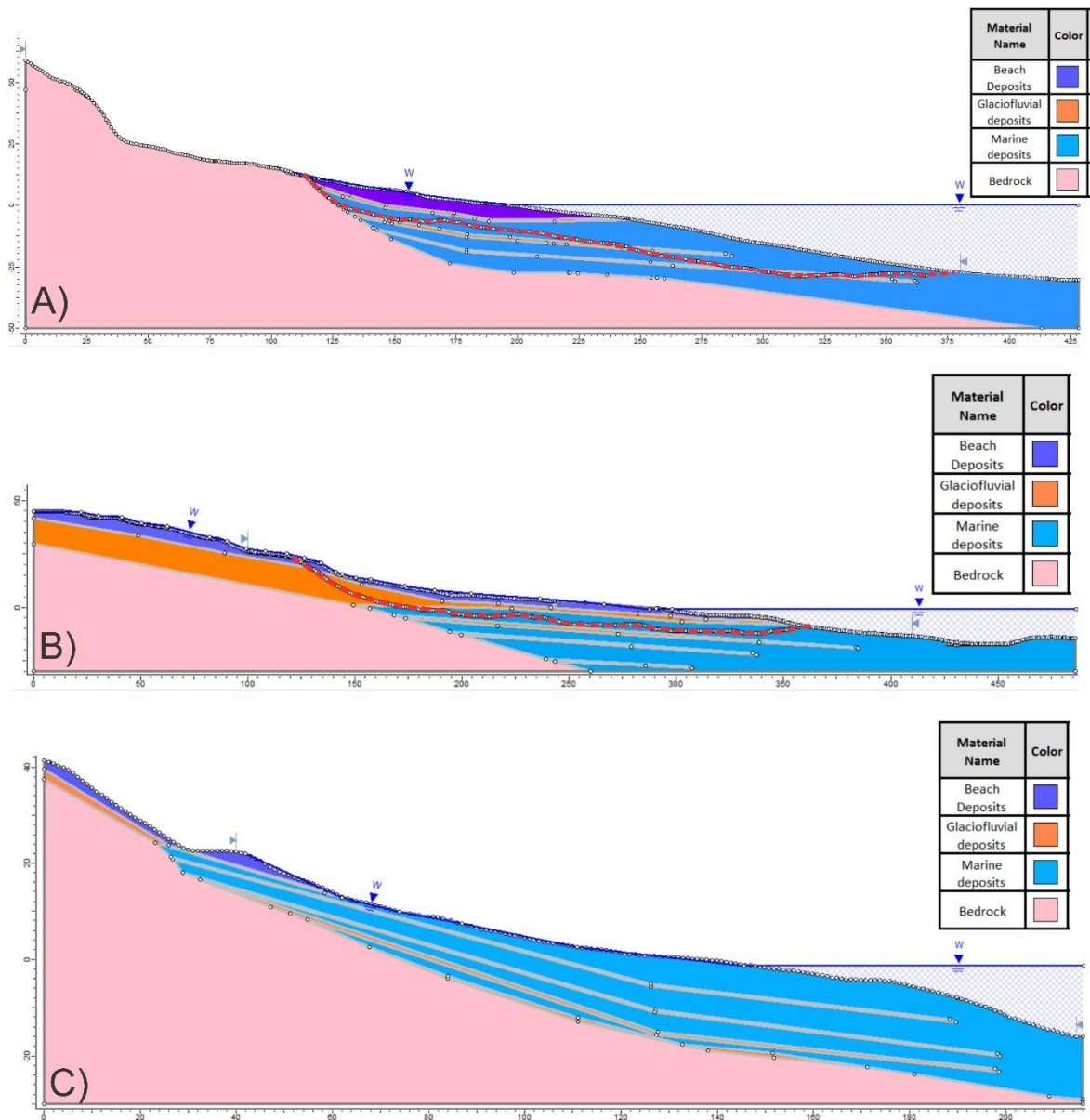
Figure 59: Profiles used for stability modeling in Slide2. Failure surface (red) is based on the post-slide LiDAR- and bathymetry data. A) Profile A-A'. B) Profile B-B'. C) Profile C-C'.

4.5.1 Low groundwater level

Low groundwater (GW) levels were simulated to determine the stability of the area in a "dry" state. This was done by lowering the groundwater table approximately 5 meters below the ground surface. For profile A-A' (Figure 60) this resulted in a FS = 1.209. The failure surface stretches a total length of 230 meters. For Profile B-B' (Figure 61), low GW levels gave a FS

= 1.248, with a failure surface of 260 m. For profile C-C' (Figure 62), FS = 1.033 with a failure surface of 80 meters.

Figure 60: Profile A-A'': Undrained total stress analysis using the grid-search method. No excess pore pressure (sea level 0 meters). FS =1.209.

Figure 61: Profile B-B'': Undrained total stress analysis using the grid-search method. No excess pore pressure (sea level 0 meters). FS = 1.248.

Figure 62: Profile C-C': Undrained total stress analysis using the grid-search method. No excess pore pressure (sea level 0 meters). FS = 1.033.

4.5.2 High groundwater level

A high GW level was modeled to determine the stability of the area after the snow-melt event, when soil saturation levels reached 100%. Hence, the groundwater level was set at the surface of the slope, and pore pressure was modeled hydrostatically, which means that no excess pore pressure was included. As a result, FS = 1.116 was achieved for profile A-A' (Figure 63), with a failure surface of 175 meters. For profile B-B' (Figure 64), high groundwater levels achieved an FS = 1.030 and a failure surface of 115 meters. Lastly, profile C-C' (Figure 65) resulted in a failed situation with FS = 0.899, and a failure surface of 80 meters.
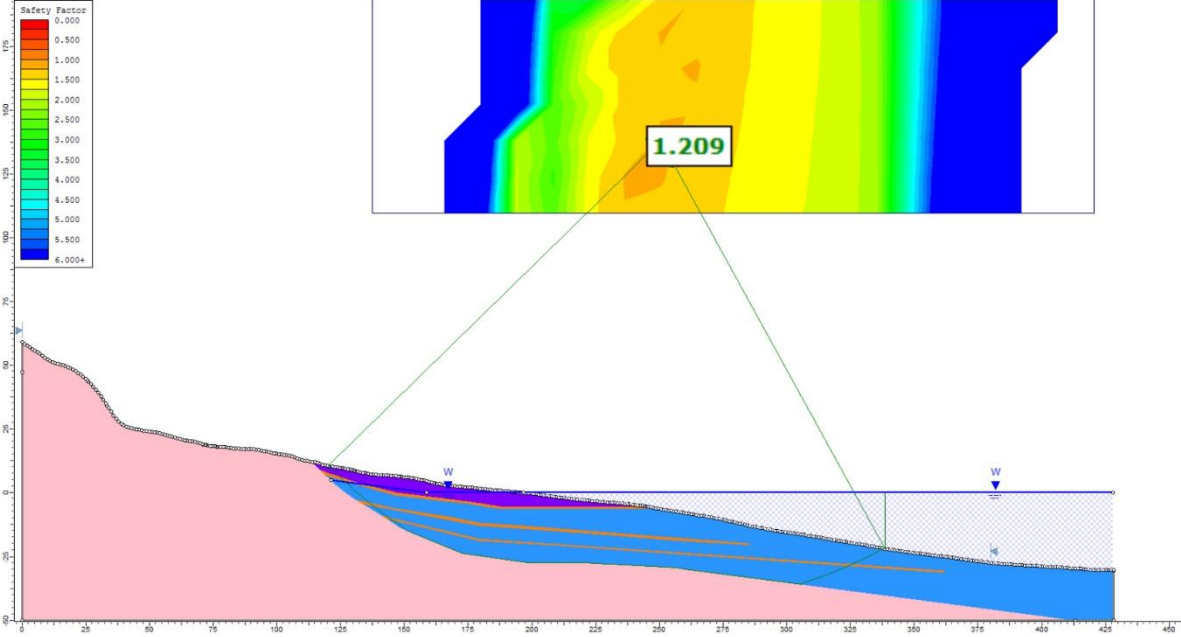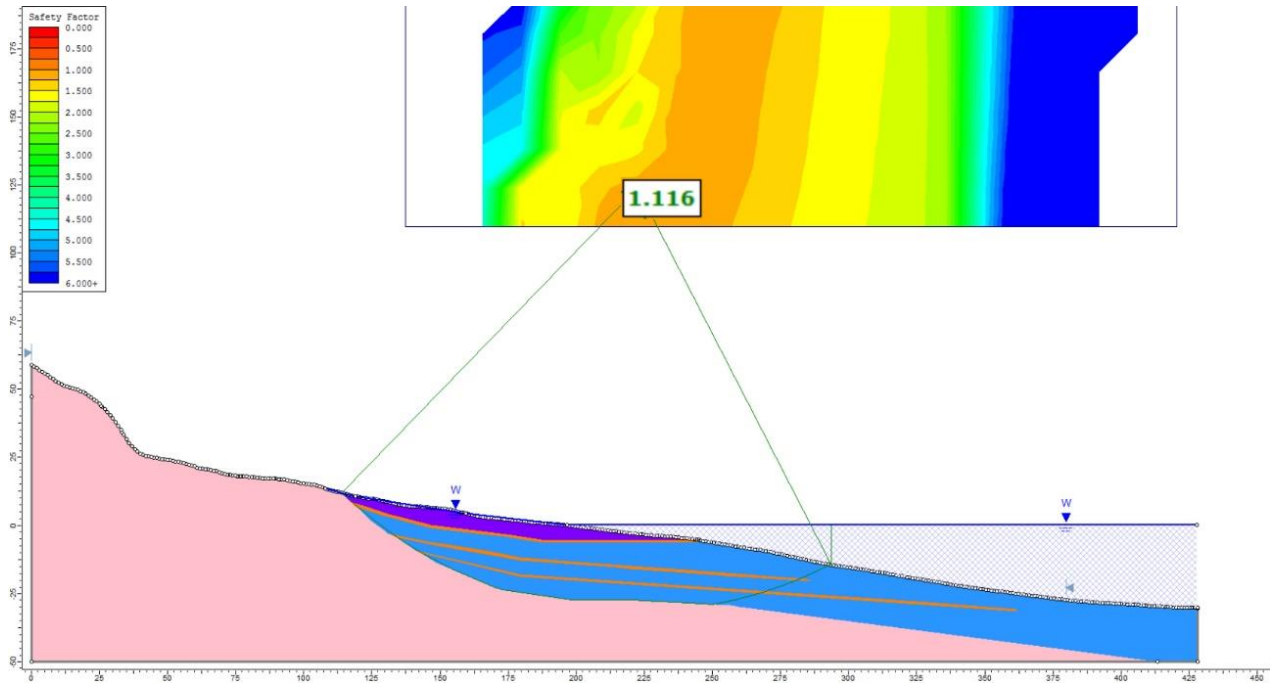
Figure 63: Profile A-A': Undrained total stress analysis using the grid-search method. No excess pore pressure (sea level 0 meter). FS =1.030
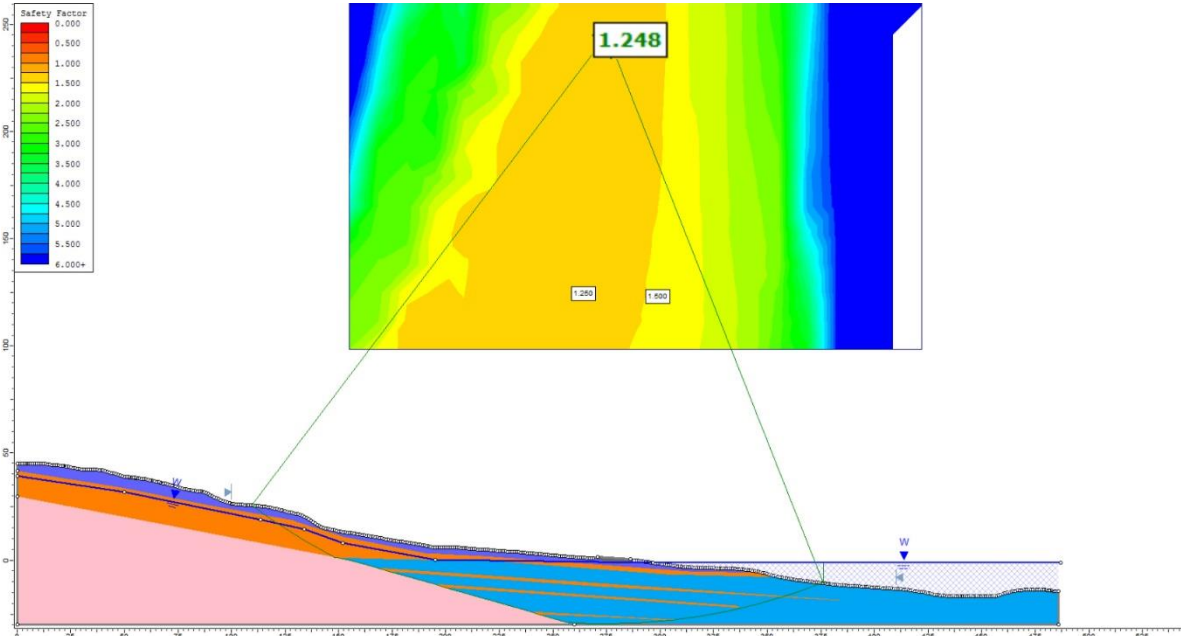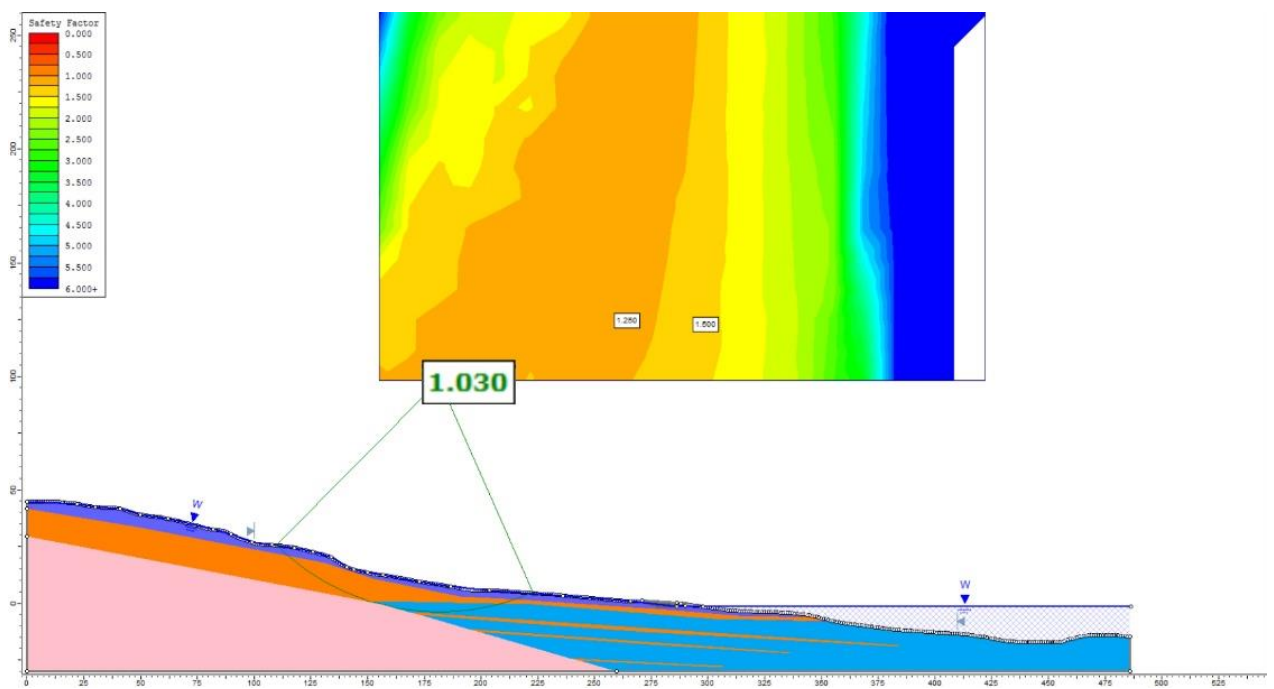

Figure 64: Profile B-: B': Undrained total stress analysis using the grid-search method. No excess pore pressure (sea level 0 meter). FS = 1.030.
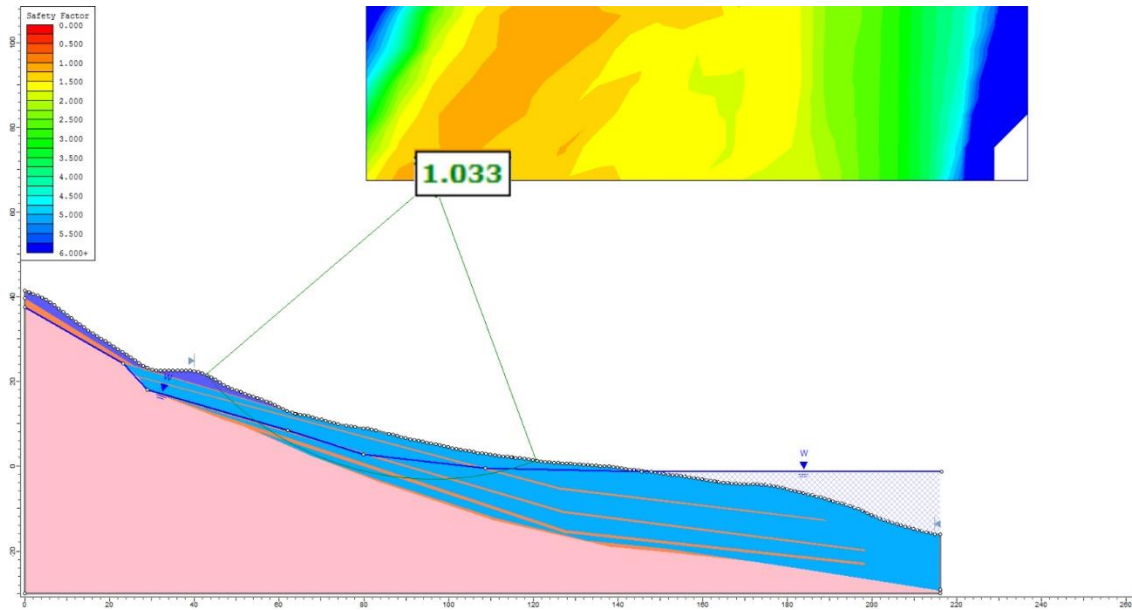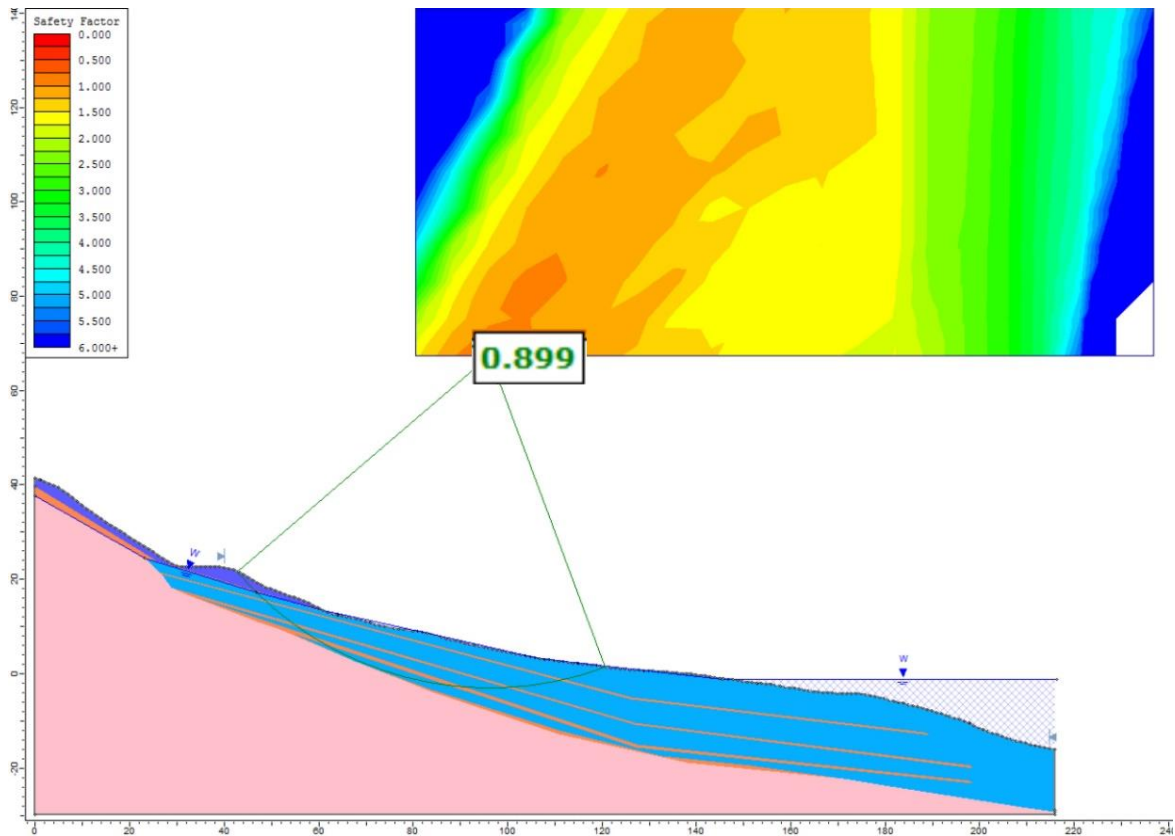
Figure 65: C-C': Undrained total stress analysis using grid-search method. No excess pore pressure (sea level 0 meter). FS = 0.899.

4.5.3 Excess pore pressure

The modeling of excess pore pressure at Kråknes is based on the assumption that coarse-grained glaciofluvial deposits are interconnected such that water from higher elevations is trapped between the impermeable marine deposit layers, building up excess pore pressure. The piezometric line was assigned ten meters above the surface, adding close to 100 kPa in excess pore pressure (Eq 5.1).

$$9.81 \frac{\text{kN}}{\text{m}^3} \text{ x } 10 \text{ m} = \sim 100 \text{ kPa} \tag{5.1}$$

The excess pore resulted in two of the three profiles obtaining a factor of safety lower than 1, indicating unstable conditions. Profile B-B' (Figure 67) and C-C'(Figure 68) obtained values of FS = 0.433 and FS = 0.471, while profile A-A'(Figure 66) still registered as stable with FS

= 1.015. The length of the failure surfaces for all profiles were similar to those for high groundwater levels.
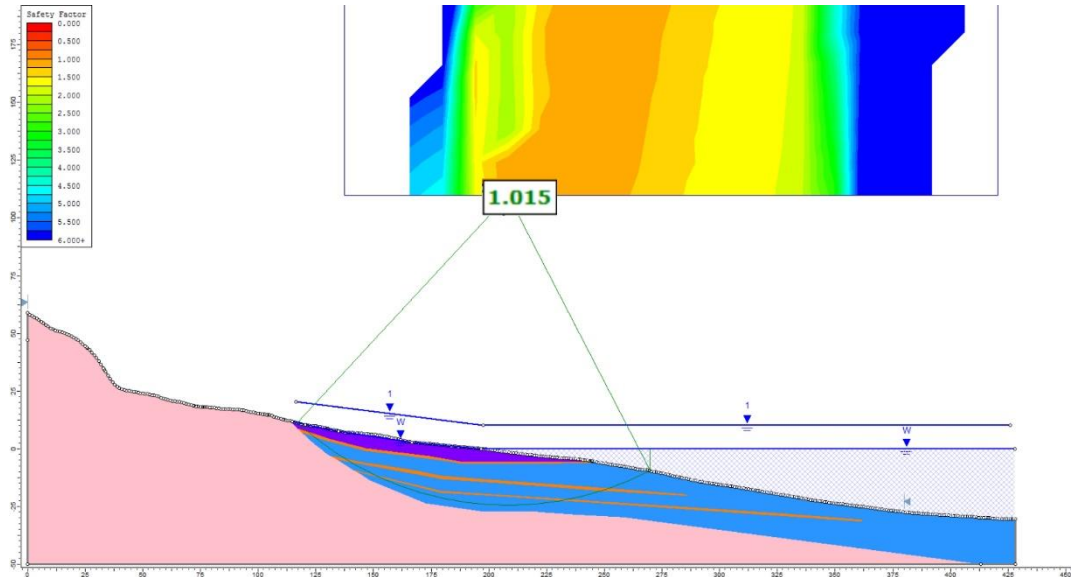
Figure 66: Profile A-A'': Undrained total stress analysis using the grid-search method. Glaciofluvial deposits (orange) are modeled with an excess pore pressure of ~100 kPa (1) (sea level 0 m). FS =1.015.
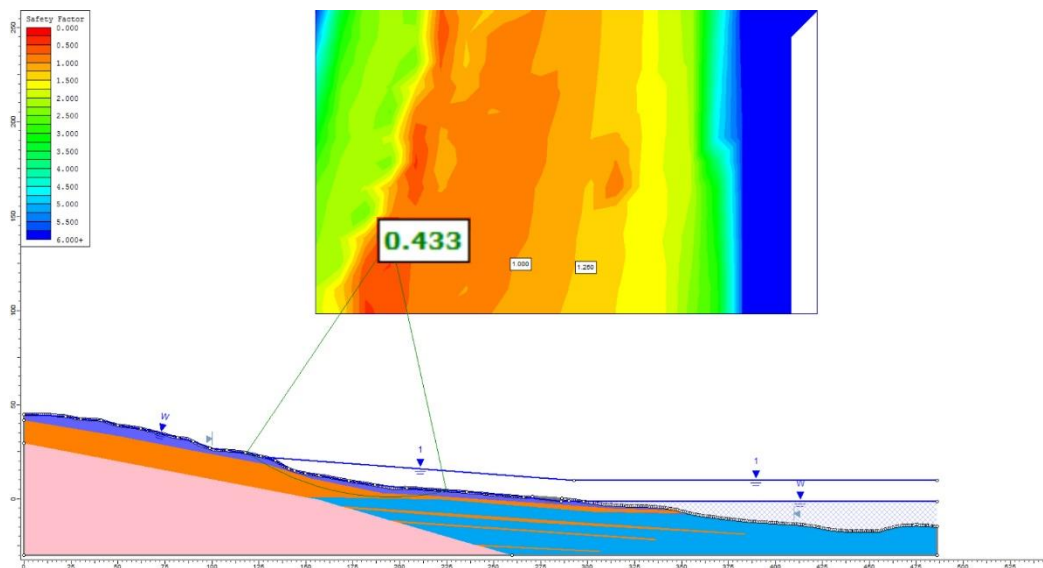
Figure 67: Profile B-B'': Undrained total stress analysis using the grid-search method. Glaciofluvial deposits (orange) are modeled with an excess pore pressure of ~100 kPa (1) (sea level 0 m). FS =0.433.
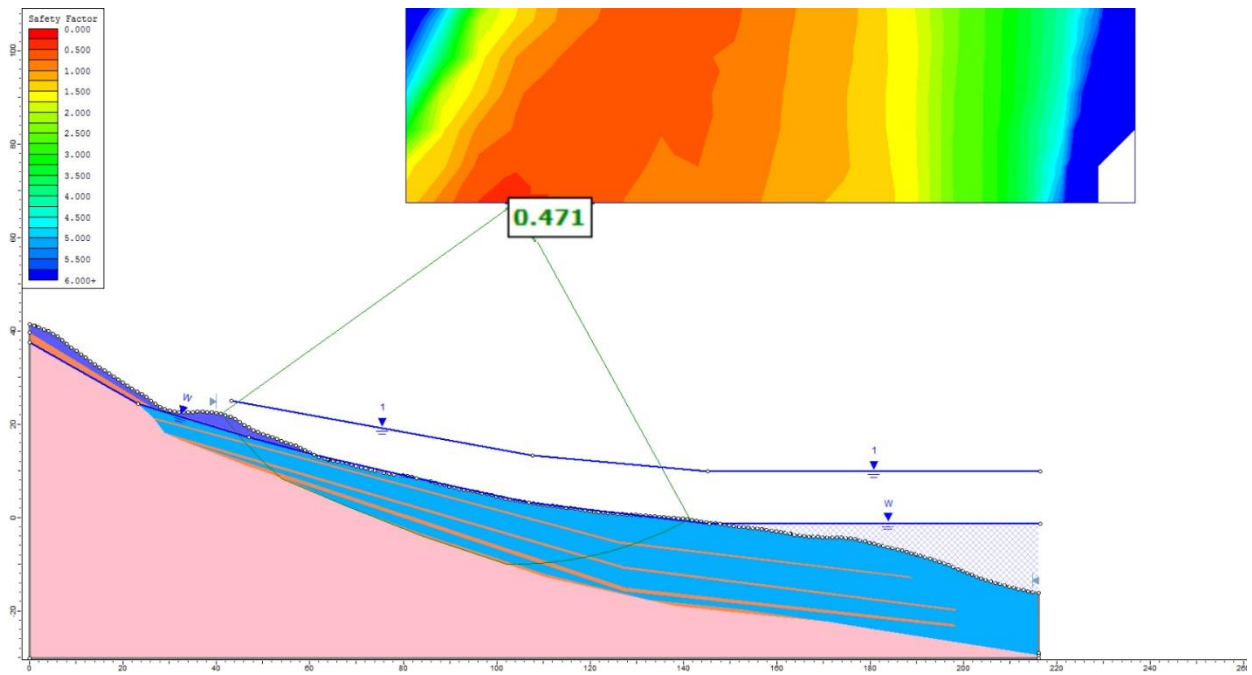
Figure 68: C-C': Undrained total stress analysis using the grid-search method. Glaciofluvial deposits (orange) are modeled with an excess pore pressure of ~100 kPa (1) (sea level 0 m). FS =0.471.

4.5.4 Loading

To model the loading from the ground work associated with the cabin building, a fill was constructed at the estimated cabin location on profile B-B'. The fill was modeled to be 55 meters in length and 4 meters thick, which was approximated from photos (Figure 55,Figure 56) and the report from Multiconsult (2021). The material parameters for the fill material are listed in Table 2.

Modeling was performed for high GW levels, under similar conditions as shown in Figure 64 (FS = 1.030). The weight of the fill material was modeled to influence the pore pressure for the underlying glaciofluvial deposits (Figure 69A). As a result, the fill added an excess pore pressure of 87 kPa, lowering the stability by 3.2 % and producing an unstable situation (FS = 0.997 < 1.0) (Figure 70). The length of the failure surface was approximately 120 meters, similar to the one produced for high GW levels (Figure 64).
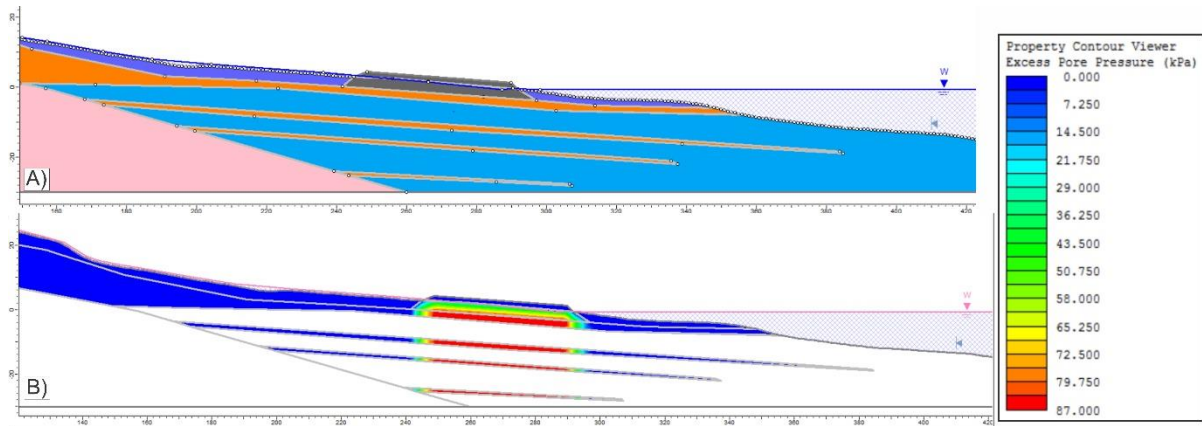
Figure 69: Profile: B-B':A) Close-up of the fill material (black) modeled at the approximate location of the cabin. The weight of the fill material was modeled to apply excess pore pressure on the underlying glaciofluvial deposits (orange). B) Profile displaying the pore pressure at the same area as A). The fill material applied an excess pore pressure up to 87 kPa on the glaciofluvial deposits. The remainder of the materials were modeled with hydrostatic pore pressure (blue) or as undrained/no pore pressure (white).
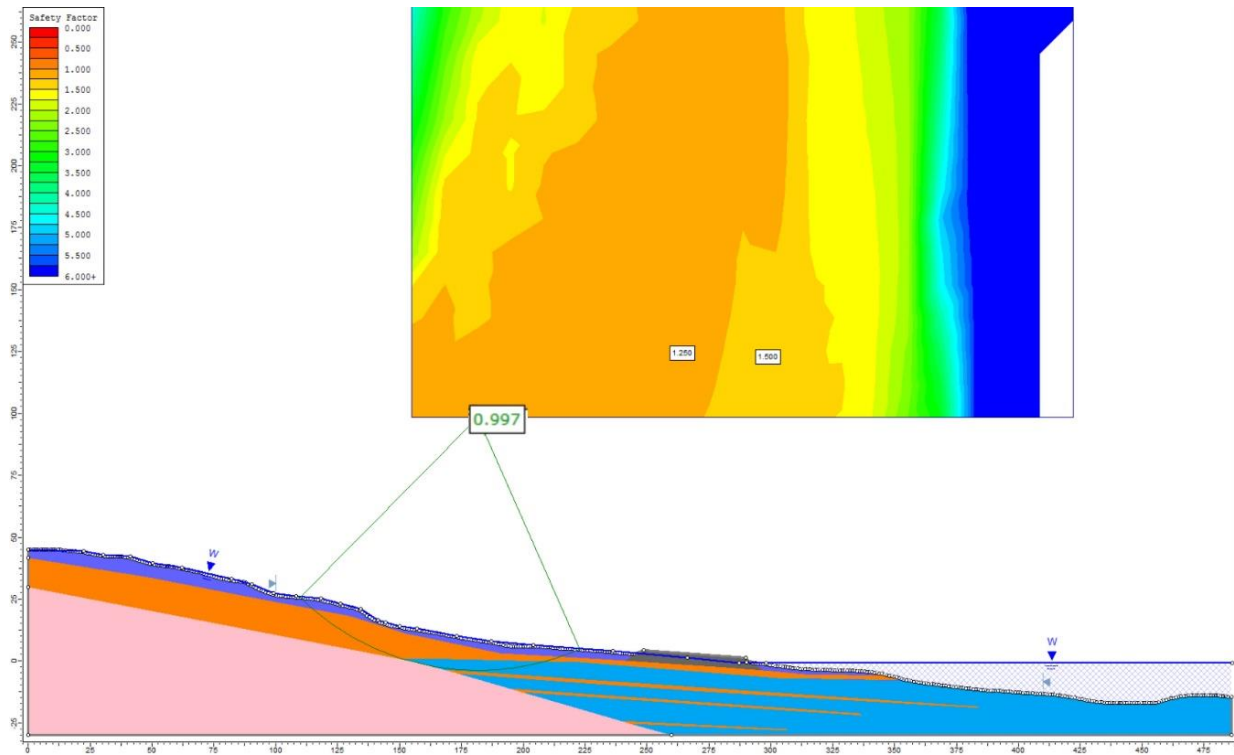
Figure 70: Profile B-B': Undrained total stress analysis using the grid-search method. FS = 0.997 with the added weight of fill material.

5 Discussion

In this chapter, the possible causal factors for the Kråknes landslide will be discussed. The discussion will bring together key results from the investigation regarding the hydrometeorological data, ground conditions and human activity. Coherent modeling results will be discussed in conjunction with the possible causal factors. Subsequently, the assumed failure mechanism for the landslide will be discussed, as well as the interpreted overall stability of the area preceding the landslide event. Lastly, an evaluation of the modeling results will be addressed, contemplating the validity and limitations of the results.

5.1 Causal factors

5.1.1 Hydrometeorology

Meteorological and hydrological data has been instrumental in the investigation of the main causal factors for the slope failure. Several studies have shown a correlation between large amounts of rainfall or snowmelt and landslides (Lafleur & Lefebvre, 1980; Terlien, 1998; Take et al., 2004; Jean Sébastien L'Heureux et al., 2017), indicating the significance of this data.

For Kråknes, temperature and precipitation registered well above average from January to May, resulting in close to all-time-high recording of snowfall and snow depth. Although the temperatures registered above average, it was still cold enough for the snowpack to retain most of its size until the middle of May (Figure 28). Subsequently, with the onset of warmer temperatures, there was a drastic increase in snowmelt, resulting in most of the snow melting in a two-week period. This snow-melt period had a substantial effect on the soil saturation and groundwater level at Kråknes, and is interpreted to be one of the main causal factors for the landslide.

As the soil saturation and groundwater levels approached their maximum, the first signs of instability started to appear. Large amounts of surficial water and a small debris avalanche were reported at the end of May, shortly followed by the formation of a tension crack on the 2nd of June (Figure 23B). Given the high levels of groundwater and soil saturation, the unit weight of the soil would increase. This presumably led to an increase in the driving forces and pore pressure acting on the slope, consequently reducing the stability. This is also reflected by the slope stability modeling, where the factor of safety was reduced for all profiles when groundwater levels were increased (Figure 63,Figure 64,Figure 65). In addition, the timing of

the tension crack corresponds well with the lowest tide levels (Figure 32), indicating a possible connection. As the tide levels dropped, the resisting forces on the slope would have been lowered, causing a more unstable situation. However, the slope stability modeling only accounts for the lowest tide level, and thus does not reflect the changes in stability caused by the tide. Hence, this effect can only be assumed.

5.1.2 Ground conditions

The investigation revealed that Kråknes is composed of both fine- and coarse-grained deposits. The fine-grained silt and clay have been interpreted to be marine deposits, while the coarser deposits of sand and gravel were interpreted to be a mixture of till-, glaciofluvial and beach deposits. However, sedimentary interpretations will not be discussed in depth, as the focus has been put on the geotechnical properties of the sediments, and how this has influenced the slope stability.

Field observations revealed that the scarp at Kråknes consisted of subsurface parallel layers of clay and silt, with the occurrence of thinner lenses of sand and gravel in between. On top of this, a thick layer of unsorted sand and gravel dominated the central part of the landslide. This combination of fine- and coarse-grained sediments has likely been essential in the destabilization of the slope. As the coarser sediments have greater permeability, water would have drained through more easily and destabilized the slope by accelerating the leaching process of the clay. This is supported by Bjerrum (1955), confirming that leaching often occurs along more permeable zones in the soil, resulting in horizontal layers of quick- and sensitive clay. From the geotechnical ground investigations, a similar trend can be observed. Quick- and sensitive clay is only found between 8 and 9 meters in BP 2 and 8, and 15 meters in BP 4 (Appendix A), suggesting that leaching is more effective through these permeable layers than from the percolation of rainwater from the surface.

In addition, excess pore pressure is interpreted to have formed in the more permeable glaciofluvial deposits prior to the slope failure. This is supported by the presence of several drainage pipes identified in the scarp, indicating a well-established hydrogeological system (Figure 36, Figure 39C, Figure 40B). With the observation of surficial water above the scarp, it is assumed that water has been confined in this area (Figure 52B.). Excess pore pressure is expected to have developed if the permeable layers and drainage pipes were uninterrupted from

this area. The excess pore pressure would be created by the difference in hydraulic head between the glaciofluvial deposits, and surrounding marine deposits. Studies by Pierson (1983) show that if drainage pipes are parallel to the fall of the slope, excess pore pressure could develop and potentially trigger a landslide. As a result, the influence of the drainage pipes in combination with excess pore pressure is regarded as one of the potential triggers for the landslide at Kråknes. The modeling results support this theory, with the factor of safety dropping drastically for profile B-B' and C-C' with the addition of excess pore pressure on the glaciofluvial deposits (Figure 67, Figure 68). The validity of these results will be discussed in more detail later on.

The surrounding bedrock is also interpreted to have played an important role in the destabilization of the slope. With water being one of the most effective catalysts for slope failure, it is important to evaluate all the possibilities where water can infiltrate the slope. For Kråknes, the bedrock is characterized by fractures and faults that are believed to have facilitated water flow into the landslide area (Figure 51C). The NW dip on the large-scale faults indicates that water could be transported into the area through these structures. Additionally, the overall aspect of the bedrock and ground surface is interpreted to acts as a relief, encouraging water to be guided into the landslide area (Figure 51A).

For the subaqueous morphology, the pre-slide bathymetry did not reveal any destabilizing factors that were directly linked to the slope failure. No visible signs of erosion or pockmarcks were uncovered, and the element of rapid sediment deposition was ruled out due to the area not being under the influence of a large river system at the time. By comparing pre- and post-slide bathymetry, it is apparent that both slides have created elongated channels where the debris has been transported away from the slope (Figure 50). This suggests that the material for both slides has been composed of highly liquefiable sediments, such as sensitive clays (Hansen et al., 2013).

Apart from the sediment and bedrock at Kråknes, InSAR-data and seismic activity were also investigated for observations that could be attributed to the slope failure. The InSAR-data revealed an average displacement of 3-5 mm/yr at Kråknes, with some reflectors averaging close to 20 mm/yr (Figure 49). Due to the limited data for the area, and possible sources of error, little emphasis has been put on these observations. Similarly, seismic activity has been

considered to be unrelated to the slope failure at Kråknes, as there were no recordings close to the time event (Appendix B).

5.1.3 Human activity

Four human activities have potentially influenced the stability of the site. The landfill at the eastern side of Kråknes was established in 2015 in accordance with the establishment of the new E6 (Figure 54). With the size and potential weight of the landfill, unstable conditions would be expected if the landfill was located in an area predisposed to instability. However, the location of the landfill is regarded as an unlikely to be a contributing factor as it is placed on the opposite side of the peninsula to Kråknes. It is also deposited directly on bedrock, removing the potential effect of subsidence of the ground underneath. As for water transport, the same argument is interpreted to be applicable, as water from the landfill will concern a different watershed.

Similarly, the mass relocation (Figure 56) and the roadwork (Figure 57) executed at Kråknes are interpreted to have had minimal effect on the slope stability. The mass relocation involved relatively small amounts of material, which is why the stability impact has been interpreted to be negligible. As for the roadwork, the cleaning of the gutters may have induced a higher water flow than previously, instigating more erosion in the gutters. However, this is believed to only affect the surface layers at Kråknes, and consequently, not the overall stability of the slope. On account of this, the only human activity that has been interpreted to impact the stability at Kråknes, is the cabin construction (Figure 55).

During construction, approximately 1000-1200 m^3 of fill was deposited on the slope. This is a large enough load that a reduction in stability would be expected. The modeling supports this, with the factor of safety dropping from 1.030 without the load to 0.997 with the load. In general, a load would be considered a contributory factor as natural conditions have to be prone to instability for human activity to trigger a landslide (Hansen 2013).

In hindsight, the influence of human activity is recognized as significant, especially when considering the abundance of quick clay and the history of previous landslides in the region. No ground investigations had been completed at Kråknes prior to the landslide. If this had been undertaken,chances are high that the sensitive clay would been discovered, and appropriate actions could have been implemented. This highlights the challenges faced with older

infrastructure built under the ML during a time when geotechnical investigations were not required. As a result, small encroachments in the terrain can result in catastrophic slope failures.

5.1.4 Assessment of failure mechanism and overall stability

Geotechnical ground investigations revealed that the area contained quick- and sensitive clay. As stated by Gregersen (1981), quick clay slides occur in two ways, either retrogressively or as flake-type slides. For the landslide at Kråknes, evidence points towards the latter. Video captured by locals witnessing the initiation of the landslide, shows large flakes releasing from the scarp, giving strong evidence towards flake-type being the dominant failure mechanism (Figure 24).This is likely the result of the sensitive- and quick clay being loaded in an undrained state caused by the snowmelt event prior to the slide. As the clay was loaded beyond its peak strength , the structure of the clay started to collapse, resulting in an immediate increase in pore pressure and a subsequent decrease in shear strength (Gregersen, 1981). This failure is interpreted to have initiated progressively, as evident by the tension crack observed on the day before the landslide (Figure 23B). The progressive failure likely developed northwards over the night, causing the landslide to initiate below Kråknesveien 416 (Figure 22).

With the assumption of a progressive flake-type failure mechanism, several factors indicate an initial low stability for Kråknes prior to the landslide. Given that extreme periods of snowmelt or rainfall likely has led to similar soil saturation levels before, the rapid snowmelt event cannot be given full accountability for triggering the landslide. The same argument is applicable for the ground conditions, where there is little data justifying an abrupt deterioration of the stability in the last 20-30 years. As a result, it is interpreted that human activities, specifically the loading of the fill associated with the cabin building is responsible for lowering the average stability sufficiently for the landslide to be triggered on June 3rd, 2020 (Figure 71).
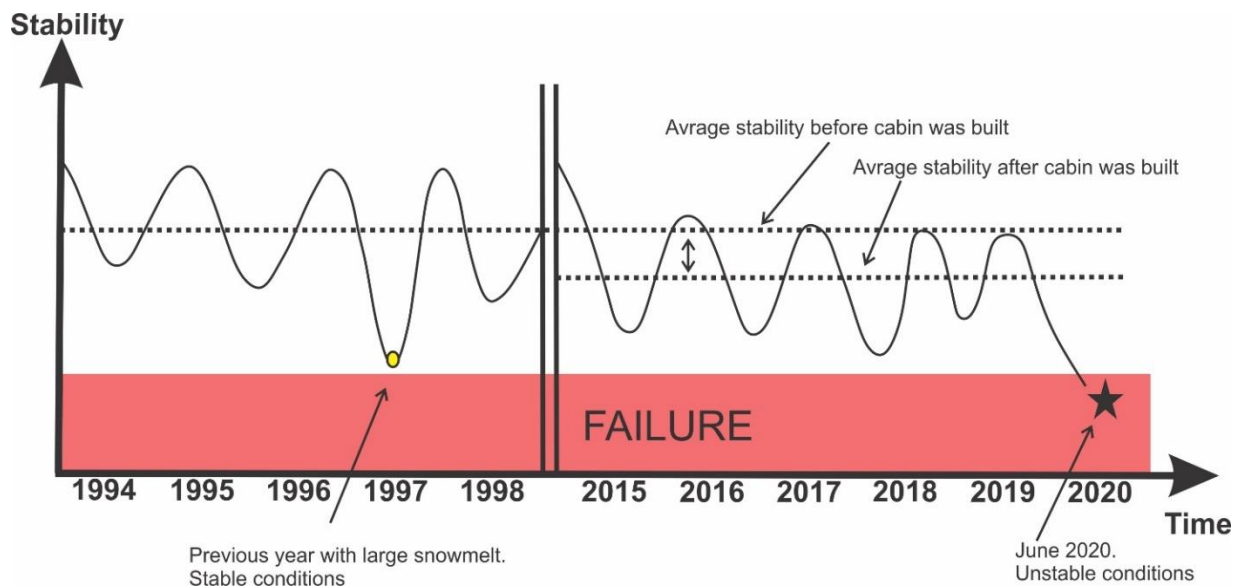
Figure 70: Principal schematic of the stability at Kråknes, before and after the cabin was built. Adapted from (Multiconsult, 2021).

5.1.5 Evaluation of modeling results

The modeling results have some major limitations. Firstly, the lowest factor of safety generated in all simulations was in profile C-C' (Figure 59C) which transects a currently stable area. Secondly, as the landslide has already occurred in this case and is being back analyzed, and the input parameters are taken from real testing the results should reflect the physical conditions in the field. However, the modeling resulted in failure surfaces that generally overestimated the depth and underestimated the length. Additionally, the modeling resulted in questionably low values for both high groundwater levels and excess pore pressure for all profiles.

The possible sources of error are many. As this is a 2D model of a 3D scenario, limitations must be accepted, both in regards to the geometry of the slope and the forces acting on it. Hence, any effect of lateral forces is disregarded in the modeling, making it a very simplistic scenario. Additionally, the model cannot account for the strain-softening behavior of the sensitive clay, which is considered to be one of the more significant sources of error. Similarly, much of the modeling is based on assumptions, both in regards to the geometry and thickness of sediments in addition to the setting of the GW level and magnitude of excess pore pressure. Consequently, the modeling results are a culmination of several possible sources of error. Hence, the question remains if the modeling results should be disregarded in total, or still can serve a purpose. Given the ambiguous results from the slope stability modeling, accurate results regarding the factor of safety is considered improbable. However, the general trend of the modeling results is presumed

90

to have validity, as the modeling demonstrates lower stability for higher groundwater levels, excess pore pressure and added loading.

6 Conclusion

The main objective of this thesis has been to determine the central causal factors for the Kråknes landslide. In doing so, the hydrometeorology, ground conditions and human activities preceding the landslide have been investigated. Slope stability modeling, using the LEM has been utilized to determine the effect of specific causal factors. In addition, the failure mechanism of the landslide and general stability at Kråknes has been estimated. The main findings of this work are:

- The landslide at Kråknes has been attributed to the culmination of several causal factors coming together in June 2020. Analyzes of hydrometeorological data indicate that high rates of precipitation combined with stable temperatures led to the preservation of a thick snowpack at Kråknes into the month of May. This was followed by a rapid increase in temperature and snowmelt, leading to most of the snow melting in a two-week period. As a result, soil saturation levels at Kråknes were modeled to have reached 100% on the 2nd of June. This is believed to have increased the loading on the slope, as well as facilitating the development of excess pore pressure, resulting in lower stability.

- Fieldwork and corroborating geotechnical investigations by Multiconsult and NVE, revealed that the ground conditions at Kråknes consisted of a layered stratigraphy, with permeable- and non-permeable sediments. Sensitive- and quick clay was detected in two of the boreholes, although it is believed to have been widespread throughout the whole area. The permeable sediments have been interpreted to be in hydrological contact with the observed surficial water above the scarp at Kråknes, producing excess pore pressure. In addition, it is assumed that water has infiltrated the landslide area through fractures and faults in the bedrock. The combination of inflow of water is believed to have intensified the leaching process of the marine clay, as well as enabling the development of excess pore pressure, causing the slope to become more unstable.

- Bathymetry data showed no clear signs that could be attributed to the triggering of the landslide, although the development of subsurface channels indicated that the landslide was composed of highly liquefiable sediments. The identification of a prehistoric scarp in combination with the remnants of an older channel, indicates that a similar landslide probably has happened at Kråknes before.

- The 80 truckloads of crushed stone deposited during the groundwork for the cabin construction in 2015, has been interpreted to have lowered the average slope stability at Kråknes.

- The observation of the tension crack on the 2nd of June is interpreted to be the start of a progressive flake-type failure in the sensitive clay at Kråknes. The timing of the tension crack corresponds with low tide levels, presumably due to a decrease in the resisting forces acting on the slope at this time. The failure is interpreted to have developed north overnight, causing the landslide to initiate below Kråknesveien 416 on the 3rd of June.

- Based on the analysis of hydrometeorology, ground conditions and human activity, the initial stability at Kråknes has been interpreted to be low. With the added loading associated with the cabin building, the average stability of the slope was reduced sufficiently to be triggered by the rapid snowmelt event in May.

- Slope stability modeling for undrained conditions showed clear discrepancies in regards to the observed conditions from the field. The modeling resulted in the lowest factor of safety for an area not affected by the slide, in addition to being inconsistent regarding the length and depth of the failure surface. However, the general trend of the modeling supports the destabilizing effect of the predicted causal factors, and thus maintains some merit.

References

Andersen, B., & Borns, H. (1994). *The Ice Age world: an introduction to Quaternary history and research with emphasis on North America and northern Europe during the last 2.5 million years*. Scandinavian University Press, Oslo.

Aune, B. (1993). *Temperaturnormaler, normalperiode 1961-1990*. Norwegian Meterol Inst 2: 1-63.

Bergh, S. G., Eig, K., Kløvjan, O. S., Henningsen, T., Olesen, O., & Hansen, J. A. (2007). *The Lofoten-Vesterålen continental margin: A multiphase Mesozoic-Palaeogene rifted shelf as shown by offshore-onshore brittle fault-fracture analysis*. Norsk Geologisk Tidsskrift, 87(1–2), 29–58.

Bergh, S. G., & Torske, T. (1988). *Palaeovolcanology and Tectonic Setting of a Proterozoic Metatholeiitic Sequence near the Baltic shield margin, northern Norway*. Precambrian Res. v.*39*, 227–246.

Bjerrum, L. (1955). *Stability of Natural Slopes in Quick Clay*. *Géotechnique*, *5*(1), 101–119.

Bjerrum, Laurits. (1954). *Geotechnical Properties of Norwegian Marine Clays*. Geotechnique, *4*(2), 49–69. https://doi.org/https://doi.org/10.1680/geot.1954.4.2.49

Böse, M., Lüthgens, C., Lee, J. R., & Rose, J. (2012). Quaternary glaciations of northern Europe. *Quaternary Science Reviews*, *44*, 1–25.

Dehls, J. F., Larsen, Y., Marinkovic, P., Lauknes, T. R., Stødle, D., & Oslo, N.-. (2019). *INSAR . NO : A NATIONAL INSAR DEFORMATION MAPPING / MONITORING SERVICE IN NORWAY -- FROM CONCEPT TO OPERATIONS Geological Survey of Norway Postbox 6315 Torgarden , NO-7491 Trondheim , Norway NORCE Postbox 6434 , NO-9294 Tromsø , Norway PPO . labs 2496PC T. Figure 1*, 5461–5464.

Devoli, G., Kleivane, I., Sund, M., Orthe, N.-K., Ekker, R., Johnsen, E., & Colleuille, H. (2015). Landslide Early Warning System and Web Tools for Real-Time Scenarios and for Distribution of Warning Messages in Norway. *Engineering Geology for Society and Territory - Volume 2: Landslide Processes*, *2*, 625–629. https://doi.org/https://doi.org/10.1007/978-3-319-09057-3_104

Devoli, G., Ingeborg, K., Monica, S., Nils-Kristian, O., Ragnar, E., Erik, J., & Hervé, C. (2015). Landslide early warning system and web tools for real-time scenarios and for distribution of warning messages in Norway. In G. Lollino, D. Giordan, G. B. Crosta, J. Corominas, R. Azzam, J. Wasowski, & N. Sciarra (Eds.), Engineering Geology for Society and Territory (Vol. 2, pp. 625– 629). Switzerland: Cham: Springer International Publishing.

Devoli, G., & Strand, S. (2020). NVE. *Internt notat Kvikkleireskred i Kråknes i Alta, 03. juni 2020 – Sammenstilling av hydrometeorologiske forhold*.

DroneDeploy. (2020). *Drone Mapping Software* . Retrieved from: https://www.dronedeploy.com/

Duncan, J. M., Wright, S. G., & Brandon, T. L. (2014). *Soil strength and slope stability* (2nd ed.). John Wiley & Sons Inc.

Eilertsen, R. S., Hansen, L., Bargel, T. H., & Solberg, I. L. (2008). Clay slides in the Målselv valley, northern Norway: Characteristics, occurrence, and triggering mechanisms. *Geomorphology*, *93*(3–4), 548–562.c

Eronen, M., Glückert, G., & Hatakka, L. (2001). Rates of Holocene isostatic uplift and relative sea-level lowering of the Baltic in SW Finland based on studies on isolation contacts. *Boreas*, *30*(1), 17–30. https://doi.org/10.1111/j.1502-3885.2001.tb00985.x

ESRI. (2020). *What is ArcMap?* Retrieved 12.09.2020 from:

https://desktop.arcgis.com/en/arcmap/latest/map/main/what-is-arcmap-.htm.

Fredin, O., Bergstrøm, B., Eilertsen, R., Hansen, L., Longva, O., Nesje, A., & Sveian, H. (2013). *Glacial landforms and Quaternary landscape development in Norway*. Norges geologiske undersøkelse, Special Publication, 13, 5-25.

Geotech. (2015). *Datasheet - Geotech CPT Probes*.Retrieved from: http://gateway.geotech.se/manuals/CPT_NOVA-Manual-EN.pdf

Giles, D. P. (2020). Quick clay behaviour in sensitive quaternary marine clays – A UK perspective. *Geological Society Engineering Geology Special Publication*, *29*(1), 205–221. https://doi.org/10.1144/EGSP29.7

Gregersen, O. (1981). The quick clay landslide in Rissa, Norway. In *Soil mechanics and foundation engineering. Proc 10th international conference, Stockholm, June 1981. Vol. 3, (A.A. Balkema)* (pp. 421–426).

Grinde, L., Mamen, J., Tunheim, K., & Tveito, O. E. (2020a). *Været i Norge. Klimatologisk månedsoversikt. Januar 2020* (02-2020). https://www.met.no/publikasjoner/met-info/met-info-2020

Grinde, L., Mamen, J., Tunheim, K., & Tveito, O. E. (2020b). *Været i Norge. Klimatologisk månedsoversikt. Februar 2020 og vintersesongen 2019/20* (02-2020). *https://www.met.no/publikasjoner/met-info/met-info-2020.*

Grinde, L., Mamen, J., Tunheim, K., & Tveito, O. E. (2020c). *Været i Norge. Klimatologisk månedsoversikt. Mars 2020* (03-2020*). https://www.met.no/publikasjoner/met-info/met-info-2020.*

Grinde, L., Mamen, J., Tunheim, K., & Tveito, O. E. (2020d). *Været i Norge. Klimatologisk månedsoversikt. April 2020* (04-2020*). https://www.met.no/publikasjoner/met-info/met-info-2020.*

Grinde, L., Mamen, J., Tunheim, K., & Tveito, O. E. (2020e). *Været i Norge. Været i Norge. Klimatologisk månedsoversikt. Mai 2020* (05-2020*).*
https://www.met.no/publikasjoner/met-info/met-info-2020.

Grinde, L., Mamen, J., Tunheim, K., & Tveito, O. E. (2020f). *Været i Norge. Klimatologisk månedsoversikt. Juni 2020* (06-2020*). https://www.met.no/publikasjoner/met-info/met-info-2020*

Hampton, M. A., Lee, H. J., & Locat, J. (1996). *Submarine Landslides*. *34*. https://doi.org/10.1007/978-3-319-57852-1_13

Hansen, L., L'Heureux, J.-S., Solberg, I.-L., & Longva, O. (2013). *Forebyggende kartlegging mot skred langs strandsonen i Norge*. (Naturfareprosjektet: Delprosjekt 6 Kvikkleire 8241008902.

Hansen, L., L'Heureux, J. S., & Longva, O. (2011). Turbiditic, clay-rich event beds in fjord-marine deposits caused by landslides in emerging clay deposits - palaeoenvironmental interpretation and role for submarine mass-wasting. *Sedimentology*, *58*(4), 890–915. https://doi.org/10.1111/j.1365-3091.2010.01188.x

Hansen, L. (2020). Kvartærgeologi rundt Kråkneset ved Altafjorden. Innspill til utredning av Kråknesskredet 3. juni 2020.Retrieved from: https://www.alta.kommune.no/getfile.php/4825994.1023.siqawqjblsziaw/NVE+Ekstern+Rapport+4+2021.pdf

Haugen, E. (2016). A preliminary attempt towards soil classification chart from total sounding. *Proceedings of the 17th Nordic Geotechnical Meeting*.

Highland, L. M., & Bobrowsky, P. (2008). The landslide Handbook - A guide to understanding landslides. *US Geological Survey Circular*, *1325*, 1–147. https://doi.org/10.3133/cir1325

Holtz, R., Kovacs, W., & Sheahan, T. (2010). *An introduction to geotechnical engineering* (2nd ed.). Pearson.

Hoseth, K. A., Kristensen, L. L., & Håland, G. (2014). Sikringstiltak mot skred- og flom Befaring i Troms og Finnmark høst 2012. In *Naturfareprosjektet: Delprosjekt 7 Skred og flomsikring* (Rapport nr.4/2014).

Høydal, Ø. A., & Haugland, H. H. (2011).NVE. *Kvikkleirekartlegging - Kartblad Alta: Risiko for kvikkleireskred*. Retrieved from:
https://webfileservice.nve.no/API/PublishedFiles/Download/201600907/1867124

Huang, Y. H. (2014). *Slope Stability Analysis by the Limit Equilibrium Method*. American Society of Civil Engineer.

Hughes, A. L. C., Gyllencreutz, R., Lohne, Ø. S., Mangerud, J., & Svendsen, J. I. (2016). The last Eurasian ice sheets - a chronological database and time-slice reconstruction, DATED-1. *Boreas*, 45(1), 1–45. https://doi.org/10.1111/bor.12142

Jørgensen, P. Sørensen, R., Haldorsen, S., (1995). *Kvartærgeologi*. Norges Landbrukshøyskole,Tun Forlag.

Kartverket. (2020). *Topografisk norgeskart gråtone*. Retrieved from:
www.kartverket.no

Koehl, J. B. P., Bergh, S. G., Osmundsen, P. T., Redfield, T. F., Indrevær, K., Lea, H., & Bergø, E. (2019). Late devonian–carboniferous faulting and controlling structures and fabrics in NW finnmark. *Norsk Geologisk Tidsskrift*, 99(3), 1–39.
https://doi.org/10.17850/njg99-3-5

Kramer, S. L. (1988). Triggering of liquefaction flow slides in coastal soil deposits. *Engineering Geology*, 26(1), 17–31. https://doi.org/10.1016/0013-7952(88)90004-X

L'Heureux, J., Locat, A. . ., Leroueil, S., Demers, D., & Locat, J. (eds). (2014). Landslides in Sensitive Clays From Geosciences to Risk Managment. In *Advances in Natural and Technological Hazards Research* (Vol. 36). https://doi.org/10.1007/978-94-007-7079-9_25

L'Heureux, J. S., Hansen, L., Longva, O., & Eilertsen, R. S. (2011). Landslides along Norwegian fjords: causes and hazard assessmen. In *Landslide science and practice* (pp. 81–87). Springer.

L'Heureux, J. L., Longva, O., Steiner, A., & Hansen, L. (2012). Submarine Mass Movements and Their Consequences. *Submarine Mass Movements and Their Consequences*, *January*. https://doi.org/10.1007/978-94-007-2162-3

L'Heureux, J. S., Hansen, L., Longva, O., Emdal, A., & Grande, L. O. (2010). A multidisciplinary study of submarine landslides at the Nidelva fjord delta, Central Norway - Implications for geohazard assessment. *Norsk Geologisk Tidsskrift*, 90(1–2), 1–20.

L'Heureux, Jean Sébastien, Nordal, S., & Austefjord, S. W. (2017). Revisiting the 1959 quick clay landslide at Sokkelvik, Norway. *Advances in Natural and Technological Hazards Research*, *46*, 395–405. https://doi.org/10.1007/978-3-319-56487-6_35

Lafleur, J., & Lefebvre, G. (1980). Groundwater regime associated with slope stability in Champlain clay deposits. *Canadian Geotechnical Journal*, *17*(1), 44–53.
https://doi.org/10.1139/t80-004

Larsen, H. (2020). Aud mistet lillebror Harder (19) i dødsraset: – Det var helt grusomt. Jeg kan ikke beskrive det. *Altaposten*.

Larsen, H., & Quist, C. (2020). *Her går jordraset i Alta: – Jeg løp for livet*. Retrieved 12.01.2021 from: https://www.vg.no/nyheter/innenriks/i/wP1wEM/her-gaar-jordraset-i-alta-jeg-loep-for-livet

Leroueil, S. (2001). Natural slopes and cuts: Movement and failure mechanisms. *Geotechnique*, *51*(3), 197–243. https://doi.org/10.1680/geot.2001.51.3.197

Lin, H., Zhong, W., Xiong, W., & Tang, W. (2014). Slope stability analysis using limit equilibrium method in nonlinear criterion. *Scientific World Journal*.

Lunne, T., Robertson, P. K., & Powell, J. J. . (1997). *Cone Penetration Testing in Geotechnical Practice*. London, Blackie.

Mamen, J. (2020). Köppens klimaklassifikasjon . In *Store Norske Leksikon*. https://snl.no/Köppens_klimaklassifikasjon

Meteorologisk Institutt. (2020). *Norsk Klimaservicesenter*. https://seklima.met.no/observations/

Multiconsult. (2021). *Årsaksvurdering – Kvikkleireskredet ved Kråknes i Alta 3. juni 2020*. Nr.4/2021 Retrieved from: https://www.alta.kommune.no/getfile.php/4825994.1023.siqawqjblsziaw/NVE+Ekstern+Rapport+4+2021.pdf

NGF. (1994a). *Veiledning for utførelse av totalsodering*. Rev. nr. 1/2018. Retrieved from: www.ngf.no

NGF. (1994b). Veiledning for utførelse av trykksondering. Rev. nr 3/2010. Retrieved from: www.ngf.no

NGI. (2011). Kvikkleirekartlegging - Kartblad Alta. *Risiko for kvikkleireskred*. *https://www.nve.no/flaum-og-skred/kartlegging/faresonekart-kommuner/troms-og-finnmark/alta-kommune/kvikkleirerapporter-for-alta-kommune/*

NGI. (2021). *Kvikkleireskred i Norge*. Retrieved 01.09.2020 from https://www.ngi.no/Tjenester/Fagekspertise/Jordskred-og-leirskred/Kvikkleireskred-i-Norge

NGU. (2020a). *About the mapping service*. Retrieved 10.09.2020 from https://www.ngu.no/en/topic/about-mapping-service

NGU. (2020b). *InSAR Norway*. Retrieved 10.09.2020 from www.insar.ngu.no

NGU. (2020c). *Løsmassekart*. Retrieved from: http://geo.ngu.no/kart/losmasse_mobil/

Nichols, G. (2009). *Sedimentology and Stratigraphy* (2nd ed.). Wiley-Blackwell.

Norsk Klimaservicesenter. (2016). *Klimaprofil Finnmark -Et kunnskapsgrunnlag for klimatilpasning*.Retrieved from: https://cms.met.no/site/2/klimaservicesenteret/klimaprofiler/klimaprofil-finnmark/_attachment/12030?_ts=15d9d0f0e06

NVE. (2016). *Snøtaksering*. Retrieved 16.10.2020 from https://www.nve.no/hydrologi/sno/snotaksering/?ref=mainmenu

NVE. (2020). *Synes du det har vært mye snø i år?*. Retrieved 21.10.2020 from https://www.varsom.no/nytt/snorapporter-fra-nve/synes-du-det-har-vaert-mye-sno-i-ar/

NZGS. (2005). Field Description of Soil and Rock. NZ Geotechnical Society Inc. Retrieved from: https://fl-nzgs-media.s3.amazonaws.com/uploads/2016/06/Field-guide-sheet-description-of-soil-and-rock-2005.pdf

Olsen, L., Sveian, H., Ottesen, D., & Rise, L. (2013). Quaternary glaciations and their variations in Norway and on the Norwegian continental shelf. *Quaternary Geology of Norway*, 27–78.

Patton, H., Hubbard, A., Andreassen, K., Auriac, A., Whitehouse, P. L., Stroeven, A. P., Shackleton, C., Winsborrow, M., Heyman, J., & Hall, A. M. (2017). Deglaciation of the Eurasian ice sheet complex. *Quaternary Science Reviews*, *169*, 148–172. https://doi.org/10.1016/j.quascirev.2017.05.019

Pierson, T. C. (1983). Soil pipes and slope stability. *Quarterly Journal of Engineering Geology*, *16*(1), 1–11. https://doi.org/10.1144/gsl.qjeg.1983.016.01.01

Popescu, M. E. (2002). Landslide causal factors and landslide remediatial options. *3rd International Conference on Landslides, Slope Stability and Safety of Infra-Structures*,

1–21.

Rankka, K., Andersson-sköld, Y., Hultén, C., Larsson, R., Leroux, V., & Dahlin, T. (2004). Quick clay in Sweden. *Swedish Geotechnical Institute*, *65*, 148. http://www.swedgeo.se/upload/publikationer/Rapporter/pdf/SGI-R65.pdf

Reite, A. ., Sveian, H., & Erichsen, E. (1999). Trondheim fra istid til nåtid - landskapshistorie og løsmasser. In *Gråsteinen* (Vol. 5). Norges Geologiske Undersøkelse.

Roberts, D. (1973). *Hammerfest. Bergrunnskart Hammerfest 1:250 000*. Retrieved from: https://www.ngu.no/publikasjon/hammerfest-berggrunnskart-hammerfest-m-1250-000

Rocscience. (2001). Application of the Finite Element Method to Slope Stability. *Proceedings of the Institution of Civil Engineers*, *1*.

Rocscience. (2020). *Slide2 product sheet*. Retrieved from: https://www.rocscience.com/assets/resources/products/Slide2-Product-Sheet.pdf

Rocscience. (2021a). *Grid Search*. Retrieved from: https://www.rocscience.com/help/slide2/slide_model/surfaces/grid_search.htm

Rocscience. (2021b). *Strength Type*. Retrieved from: https://www.rocscience.com/help/slide2/slide_model/materials/strength_type.htm

Romundset, A., Bondevik, S., & Bennike, O. (2011). Postglacial uplift and relative sea level changes in Finnmark, northern Norway. Quaternary Science Reviews, 30(19–20), 2398–2421. https://doi.org/10.1016/j.quascirev.2011.06.007

Rosenqvist, I. T. (1953). Considerations on the sensitivity of Norwegian quick-clays. *Geotechnique*, *3*, 195–200. https://doi.org/https://doi.org/ 10.1680/geot.1953.3.5.195

Schanche, S. og Haugen, E. E. D. (2014a) Sikkerhet mot kvikkleireskred. (Veileder nr 7 1501- 0678). NVE.: http://publikasjoner.nve.no/veileder/2014/veileder2014_07.pdf

Skempton, A. W. (1964). Long-Term Stability of Clay Slopes. *Géotechnique*, *14*(2), 77–102. https://doi.org/10.1680/geot.1964.14.2.77

Sokalska, E., Devoli, G., Solberg, I.-L., Hansen, L., & Thakur, V. (2015). *Kvalitetskontroll, analyse og forslag til oppdatering av historiske kvikkleireskred og andre leirskred registrert i Nasjonal skredhendelsesdatabase (NSDB)*.

Statens vegvesen. (2005). *Håndbok 014 Laboratorieundersøkelser - Vedlegg 1 Jordartsklassifisering*. https://www.vegvesen.no/s/vegnormaler/hb/014/Kvalitetsikrede _filer/Vedlegg/VEDLEGG_1_april_2005.pdf

Stokes, C. R., Corner, G. D., Winsborrow, M. C. M., Husum, K., & Andreassen, K. (2014). Asynchronous response of marine-terminating outlet glaciers during deglaciation of the Fennoscandian ice sheet. *Geology*, 42(5), 455–458. https://doi.org/10.1130/G35299.1

Take, W. A., Bolton, M. D., Wong, P. C. P., & Yeung, F. J. (2004). Evaluation of landslide triggering mechanisms in model fill slopes. *Landslides*, *1*(3), 173–184. https://doi.org/10.1007/s10346-004-0025-1

Terlien, M. T. J. (1998). The determination of statistical and deterministic hydrological landslide-triggering thresholds. *Environmental Geology*, *35*(2–3), 124–130. https://doi.org/10.1007/s002540050299

Thakur, V., Grimstad, G., & Nordal, S. (2006). Instability in Soft Sensitive Clays. *Geohazards*, 43.

Van Den Eeckhaut, M., Poesen, J., & Hervás, J. (2013). Mass-Movement Causes: Overloading. *Treatise on Geomorphology*, *7*(200), 200–206. https://doi.org/10.1016/B978-0-12-374739-6.00165-2

Varnes, D. J. (1978). Slope movement types and processes. In *Landslides—Analysis and control* (pp. 11–33).

Vorren, T. O., & Mangerud, J. (2007). Istider kommer og går. In I. B. Ramberg, I. Bryhni, A. Nøttvedt, & K. Rangnes (Eds.), *Landet blir til: Norges geologi* (2nd ed., pp. 494–548).

Norsk Geologisk Forening (NGF).

Waldeland, M. J. (2020). ⟨10219825-RIG-RAP-001). *Datarapport - Geoteknisk grunnundersøkelse*. Multiconsult Norge AS.

Wiig, T., Strand, S.T., & Haugen, E.E.D. (2019) Sikkerhet mot kvikkleireskred (Veileder nr 1/2019). NVE
https://publikasjoner.nve.no/veileder/2019/veileder2019_01.pdf

Wood, D. M. (2004). *Geotechnical modelling*. Spon Press (Taylor and Francis Group), London.

Xgeo. (2020). *About Varsom Xgeo*.Retrieved: 14.11.2020 from:
http://www.xgeo.no/aboutXgeo.html?show=on

Zwaan, K.B. (1988). *Nordreisa. Berggrunnskart M 1:250 000; trykt i farger*.

Zwaan, Klaas Bouke, & Gautier, A. M. (1980). *1980: Alta and Gargia. Description of the geological maps (AMS-M711) 1834 1 and 1934 IV 1:50 000.* (Issue 357).

Appendix

Appendix **A**: Geotechnical data from ground investigation
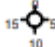
Appendix **B**: Material parameters by Multiconsult

Appendix **C**: Structural measurements

Appendix **D**: Seismic activity

A. Geotechnical data from ground investigation

If you have one or more appendixes you can add them here. Use the "Heading 1 without numbering" style at the start of each appendix.

BP.	Materiale	Vann-innhold	Udrenert skjær-fasthet	Omrørt skjær-fasthet	Plastisitets-indeks	Tegning-nr.
2	3-4 m: Leire	28-39 %	15-22 kPa	1,3 kPa	-	
	6-7 m: Leire	33-49 %	19-25 kPa	1,8-1,9 kPa	15 %	-200
	8-9 m: Siltig leire	28-35 %	16 kPa	0,8-1,4 kPa	-	-300
	9,5-10,5 m: Siltig leire	28-33 %	19-21 kPa	1,3-1,6 kPa	-	
4	2-3 m: Leire	36-44 %	10-14 kPa	1,2-1,4 kPa	-	
	6-7 m: Leire	29-48 %	12-20 kPa	1,2-1,8 kPa	26 %	
	8-9 m: Leire	22-42 %	11-23 kPa	0,8-1,2 kPa	-	-201
	10-11 m: Leire	26-33 %	10-13 kPa	0,4-0,9 kPa	15 %	-300
	12-13 m: Kvikkleire	29-39 %	16-23 kPa	0,2-0,3 kPa	-	
	14-15 m: Leire	32-44 %	11-22 kPa	0,4-0,7 kPa	8 %	
12	0-1 m: Grusig sand	6 %	-	-	-	
	1-2 m: Grusig, sandig materiale	8 %	-	-	-	
	2-3 m: Siltig, sandig leire	25 %	-	5 kPa	-	-202
	3-4 m: Siltig leire	25 %	-	2 kPa	-	-301
	4-5 m: Sandig, grusig, siltig leire	18 %	-	-	-	
	5-6 m: Grusig, sandig, siltig, leirig materiale	16 %	-	-	-	

PRØVESERIE — Borhull 2

Dybde (m)	Beskrivelse	Prøve	Test	Vanninnhold (%) og konsistensgrenser	ρ (g/cm³)	Porøsitet (%)	Organisk innhold (%)	Udrenert skjærfasthet (kPa)	S_t (-)
	kt. 8,59			10 20 30 40 50				10 20 30 40 50	
	LEIRE — sand- og siltlag, enkl.gruskorn	▨			1,92				16
5									
	LEIRE — sand- og siltlag, enkl.gruskorn	▨			1,95				10 / 11
	LEIRE, siltig — forstyrret, sand- og siltlag, enkl.gruskorn	▨	K		1,96			0,8	8
10	LEIRE, siltig — sand- og siltlag, enkl.gruskorn	▨			1,98			1,3	12 / 16
15									
20									

Symboler:

- ○ Vanninnhold
- ⊢ Plastisitetsindeks, Ip
- ▼ Omrørt konus
- ▽ Uomrørt konus
- Enaksialforsøk (strek angir aksiell tøyning (%) ved brudd)
- ρ = Densitet
- S_t = Sensitivitet
- T = Treaksialforsøk
- Ø = Ødometerforsøk
- K = Korngradering

ρ_s: 2,75 g/cm³
Grunnvannstand: m
Borbok: Digital
Lab-bok: Digital

Norges vassdrags- og energidirektorat
Ras Kråkeneset
Dato: 2020-06-25

Konstr./Tegnet:	Kontrollert:	Godkjent:
TEREZK	MARTM	BGJ
Oppdragsnummer:	Tegningsnr.:	Rev. nr.:
10219825	RIG-TEG-200	00

Multiconsult
www.multiconsult.no

Borehole log — Dybde (m) / Beskrivelse / kt. 3,17 / Prøve / Test / Vanninnhold (%) og konsistensgrenser / ρ (g/cm³) / Porøsitet (%) / Organisk innhold (%) / Udrenert skjærfasthet (kPa) / S_t (-)

Dybde (m)	Beskrivelse	Prøve	Test	ρ (g/cm³)	Udrenert skjærfasthet	S_t (-)
	LEIRE — sand- og siltlag			1,91	1,2	7 / 10
5						
	LEIRE — sand- og siltlag, enkl. gruskorn		K	1,97	1,2	17 / 11
	LEIRE — sand- og siltlag, enkl. gruskorn		T	1,91	0,8 / 1,2	14 / 15
10	LEIRE — siltlag, enkl. gruskorn		Ø	1,94	0,9 / 0,4	11 / 29
	KVIKKLEIRE — enkl. gruskorn		K Ø	1,95	0,3 / 0,2	49
	LEIRE — sand- og siltlag, enkl. gruskorn		T	1,97	0,4 / 0,7	26 / 21
15						
20						

Symboler:

Enaksialforsøk (strek angir aksiell tøyning (%) ved brudd)

- O Vanninnhold
- H Plastisitetsindeks, Ip
- ▼ Omrørt konus
- ▽ Uomrørt konus
- ρ = Densitet
- S_t = Sensitivitet
- T = Treaksialforsøk
- Ø = Ødometerforsøk
- K = Korngradering

ρs: 2,75 g/cm³
Grunnvannstand: m
Borbok: Digital
Lab-bok: Digital

PRØVESERIE

Borhull: 4

Norges vassdrags- og energidirektorat

Ras Kråkeneset

Dato: 2020-06-25

Multiconsult
www.multiconsult.no

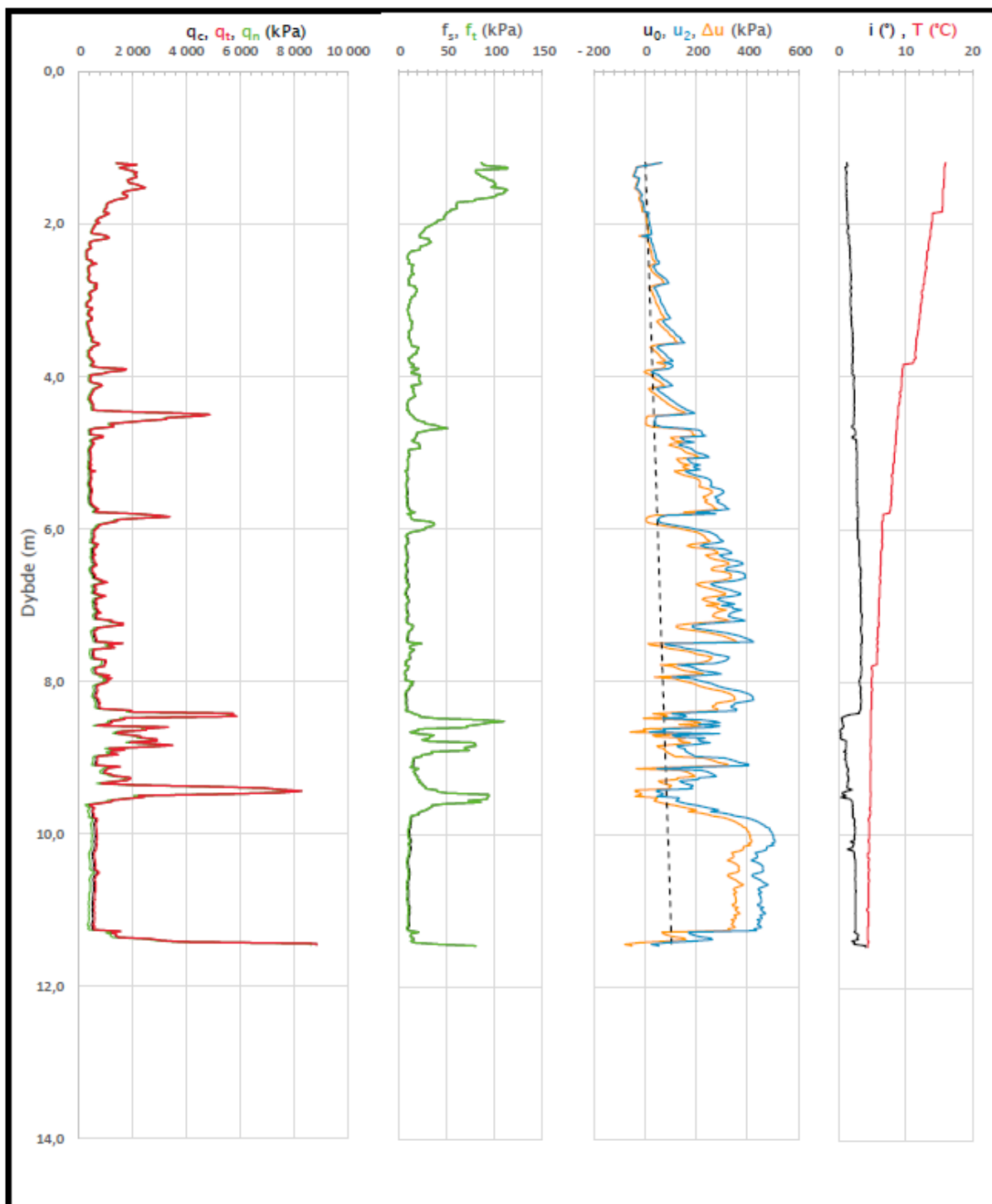| Konstr./Tegnet:	Kontrollert:	Godkjent:
TEREZK	MARTM	BGJ
Oppdragsnummer: 10219825	Tegningsnr.: RIG-TEG-201	Rev. nr.: 00

103

Dybde (m)	Beskrivelse	Prøve	Test	Vanninnhold (%) og konsistensgrenser	ρ (g/cm³)	Porøsitet (%)	Organisk innhold (%)	Udrenert skjærfasthet (kPa)	S_t (-)
	kt. 18,99			10 20 30 40 50				10 20 30 40 50	
	SAND, grusig			o (10)					
	MATERIALE, grusig, sandig		K	o (10)					
	LEIRE, siltig, sandig enkl.gruskorn		K	o (25)				▼ (30)	
	LEIRE, siltig enkl.sand- og gruskorn			o (25)				▼ (25)	
5	LEIRE, sandig, grusig, siltig		K	o (15)					
	MATERIALE, grusig, sandig, siltig, leirig		K	o (15)					
10									
15									
20									

Symboler:

$_{15}\!-\!\!\!\!\overset{8}{\underset{10}{\diamond}}\!\!\!\!-_{5}$ Enaksialforsøk (strek angir aksiell tøyning (%) ved brudd)

o   Vanninnhold   ▼   Omrørt konus ρ = Densitet   T = Treaksialforsøk ρ_s: 2,75 g/cm³

⊢—⊣   Plastisitetsindeks, Ip   ▽   Uomrørt konus S_t = Sensitivitet   Ø = Ødometerforsøk   Grunnvannstand: m

     K = Korngradering   Borbok: Digital

     Lab-bok: Digital

PRØVESERIE	Borhull:	12

Norges vassdrags- og energidirektorat   Dato: 2020-06-25

Ras Kråkeneset
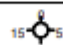
Multiconsult www.multiconsult.no	Konstr./Tegnet: TEREZK	Kontrollert: MARTM	Godkjent: BGJ
	Oppdragsnummer: 10219825	Tegningsnr.: RIG-TEG-202	Rev. nr.: 00

Prosjekt			Prosjektnummer: 10219825 Rapportnummer: RIG-RAP-001		Borhull	Kote +8,59
RAS KRÅKNESET						2
Innhold					Sondenummer	
Måledata og korrigerte måleverdier					4827	
Multiconsult	Tegnet MAJ	Kontrollert BGJ		Godkjent BGJ	Anvend.klasse	1
	Utførende Multiconsult	Dato sondering 10.06.2020		Revisjon Rev. dato	RIG-TEG	500.3

Z:\O10219\10219825-01\10219825-01-03 ARBEIDSOMRAADE\10219825-01 RIG\10219825-01-07 FELT- OG LABREGISTRERINGER\Felt\BP. 2   CPTu v.2019.05
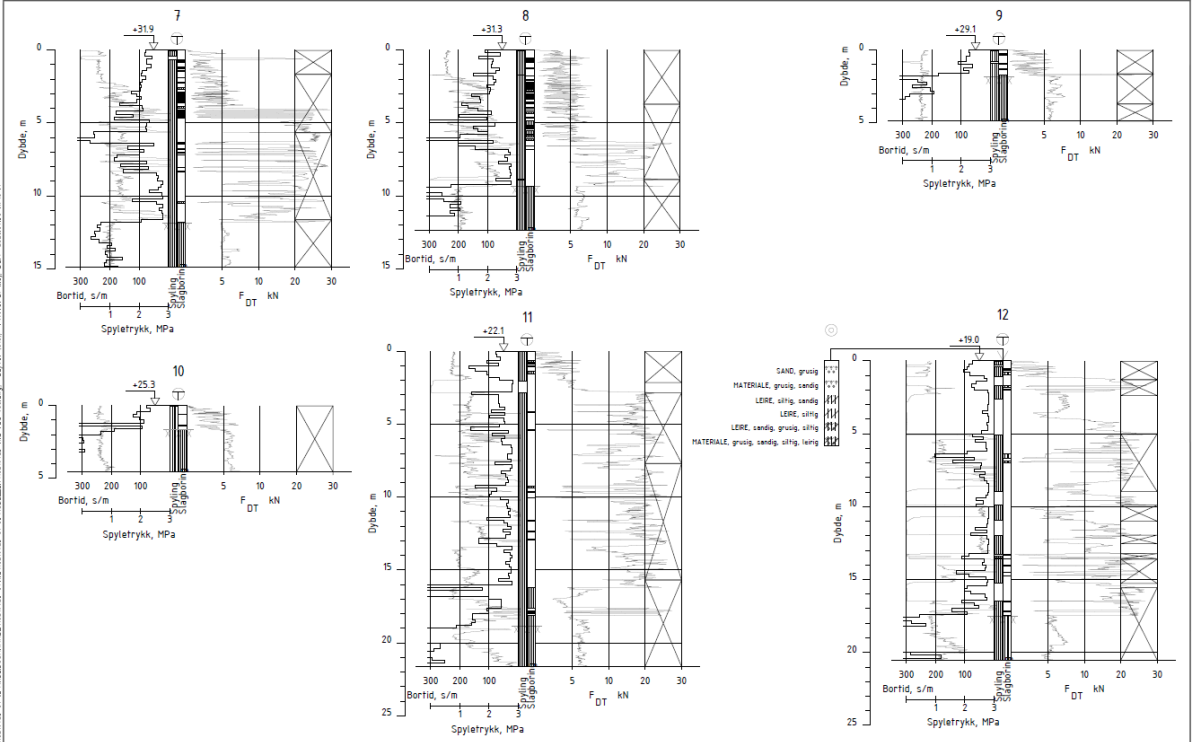
105

Profil A-A

Profil B-B

							NORGES VASSDRAG- OG ENERGIDIREKTORAT	Status –	Fag RIG	Original format A3	Dato 2020-07-28
							RAS KRÅKNESET	Konstr./Tegnet MAJ	Kontrollert BGJ	Godkjent BGJ	Målestokk 1:400
						Multiconsult	PROFIL A OG B	Oppdragsnr.	Tegningsnr.		
x	Beskrivelse		Endr.liste	Dato		www.multiconsult.no		10219825	RIG-TEG-600		Rev. –
Rev.					Tegn. Kontr. Godkj.						

Soil boring logs / totalsonderinger — boreholes 7, 8, 9, 10, 11, 12

Borehole 7: +31.9
Borehole 8: +31.3
Borehole 9: +29.1
Borehole 10: +25.3
Borehole 11: +22.1
Borehole 12: +19.0

Legend:
- SAND, grusig
- MATERIALE, grusig, sandig
- LEIRE, siltig, sandig
- LEIRE, siltig
- LEIRE, sandig, grusig, siltig
- MATERIALE, grusig, sandig, siltig, leirig

Axis labels: Dybde, m; Bortid, s/m; Spyletrykk, MPa; Spyling / Slagboring; F_DT, kN

				NORGES VASSDRAG- OG ENERGIDIREKTORAT	Status –	Fag RIG	Original format A3	Dato 2020-07-28
			Multiconsult	RAS KRÅKNESET	Konstr./Tegnet M.AJ	Kontrollert BGJ	Godkjent BGJ	Målestokk 1:200
x	Beskrivelse	Endr.liste Dato	www.multiconsult.no	TOTALSONDERINGER BP.7-12	Oppdragsnr. 10219825	Tegningsnr. RIG-TEG-601		Rev. –

108

B. Material parameters by Multiconsult

Matreialtype: Leire
Material modell: NGI-ADP

Parameter [enhet]	Verdier for zonene gitt i Figur 16								
	1	2	3	4	5	6	7	8	9
γ_{unsat} [kN/m³]	19	19	19	19	19	19	19	19	19
γ_{sat}	19	19	19	19	19	19	19	19	19
G_{ur}/s_u^A [-]	500	500	500	500	500	500	500	500	500
γ_f^C [%]	1,5	1,5	1,5	1,5	1,5	1,5	1,5	1,5	1,5
γ_f^E [%]	4	4	4	4	4	4	4	4	4
γ_f^{DSS} [%]	2,1	2,1	2,1	2,1	2,1	2,1	2,1	2,1	2,1
$s_{u\,ref}^A$ [kPa]	45	40	30	30	25	25	17	17	17
$s_u^{C,TX}/s_u^A$	0,99	0,99	0,99	0,99	0,99	0,99	0,99	0,99	0,99
y_{ref} [m]	10	7,5	5	3	1	-3	-8,5	-15,5	-22,5
$s_{u\,inc}^A$ [kPa/m]	1,5	1,5	1,5	1,2	1,6	1,6	2,1	2,1	2,1
s_u^P/s_u^A [-]	0,37	0,37	0,37	0,37	0,37	0,37	0,37	0,37	0,37
τ_0/s_u^A [-]	0,7	0,7	0,7	0,7	0,7	0,7	0,7	0,7	0,7
s_u^{DSS}/s_u^A	0,66	0,66	0,66	0,66	0,66	0,66	0,66	0,66	0,66
ν_{ref} [-]	0,495	0,495	0,495	0,495	0,495	0,495	0,495	0,495	0,495
K_0 [-]	0,7	0,7	0,7	0,7	0,7	0,7	0,7	0,7	0,7

Matreialtype: Vannførendelag
Materiallmodell: Hardenng Soil

Parameter [enhet]	Verdier
γ_{unsat} [kN/m³]	19
E_{50}^{ref} [kPa]	35000
E_{oed}^{ref} [kPa]	35000
E_{ur}^{ref} [kPa]	105000
c' [kPa]	3
φ' [°]	30
y [°]	0
K_0 [-]	0,73
OCR [-]	1,9

Matreialtype: Friskjosnmasser og fylling
Material modell: Mohr-Couloub

Parameter [enhet]	Verdier
γ_{unsat} [kN/m³]	18,8
E' [kPa]	50000
ν' [-]	0,2
c' [kPa]	10
φ' [°]	38
y [°]	0
K_0	0,38

Matreialtype: «Fjell»
Materiallmodell: Linear elastic

Parameter [enhet]	Verdier
γ_{unsat} [kN/m³]	25
E [kPa]	500000
ν' [-]	0,3
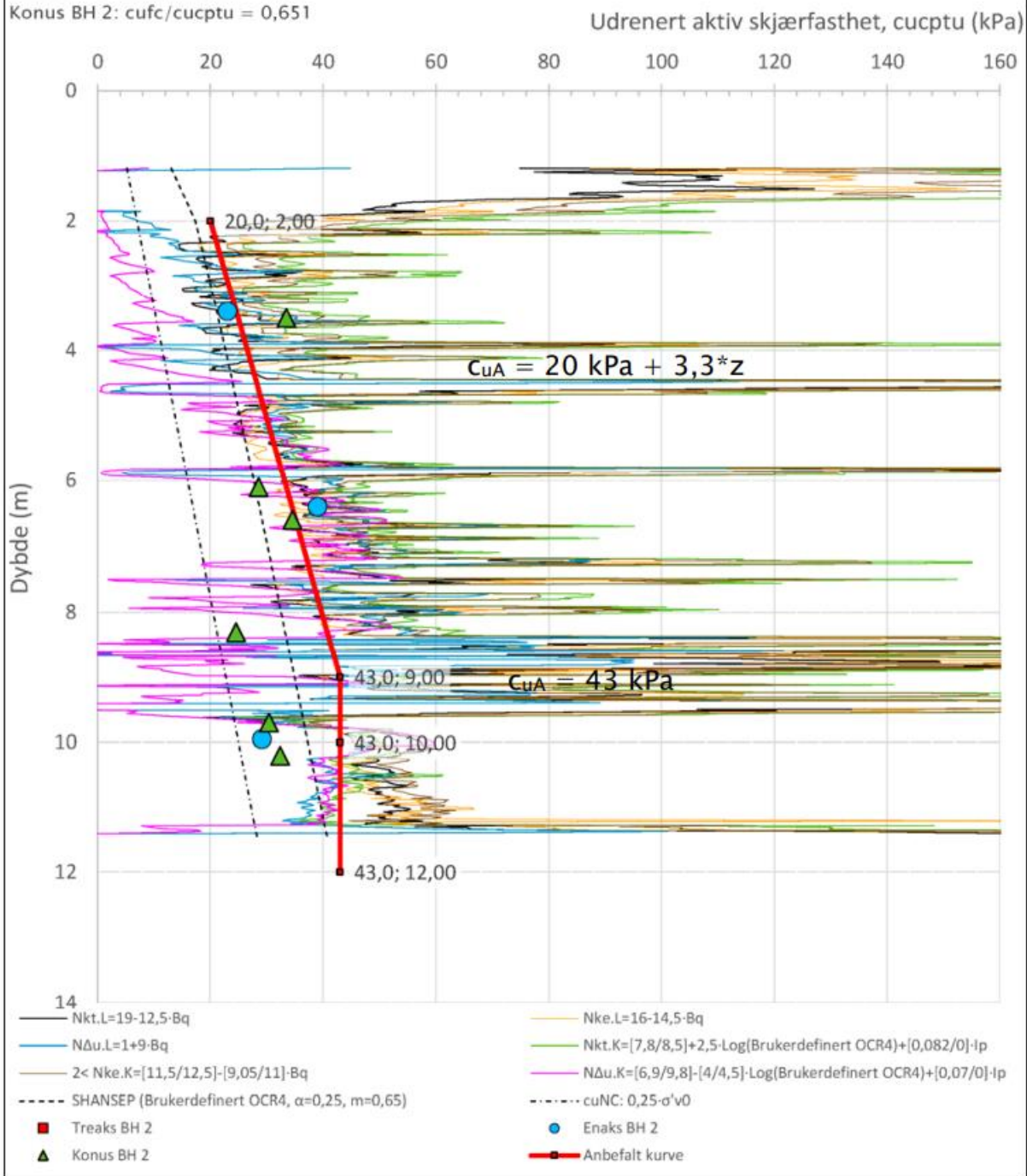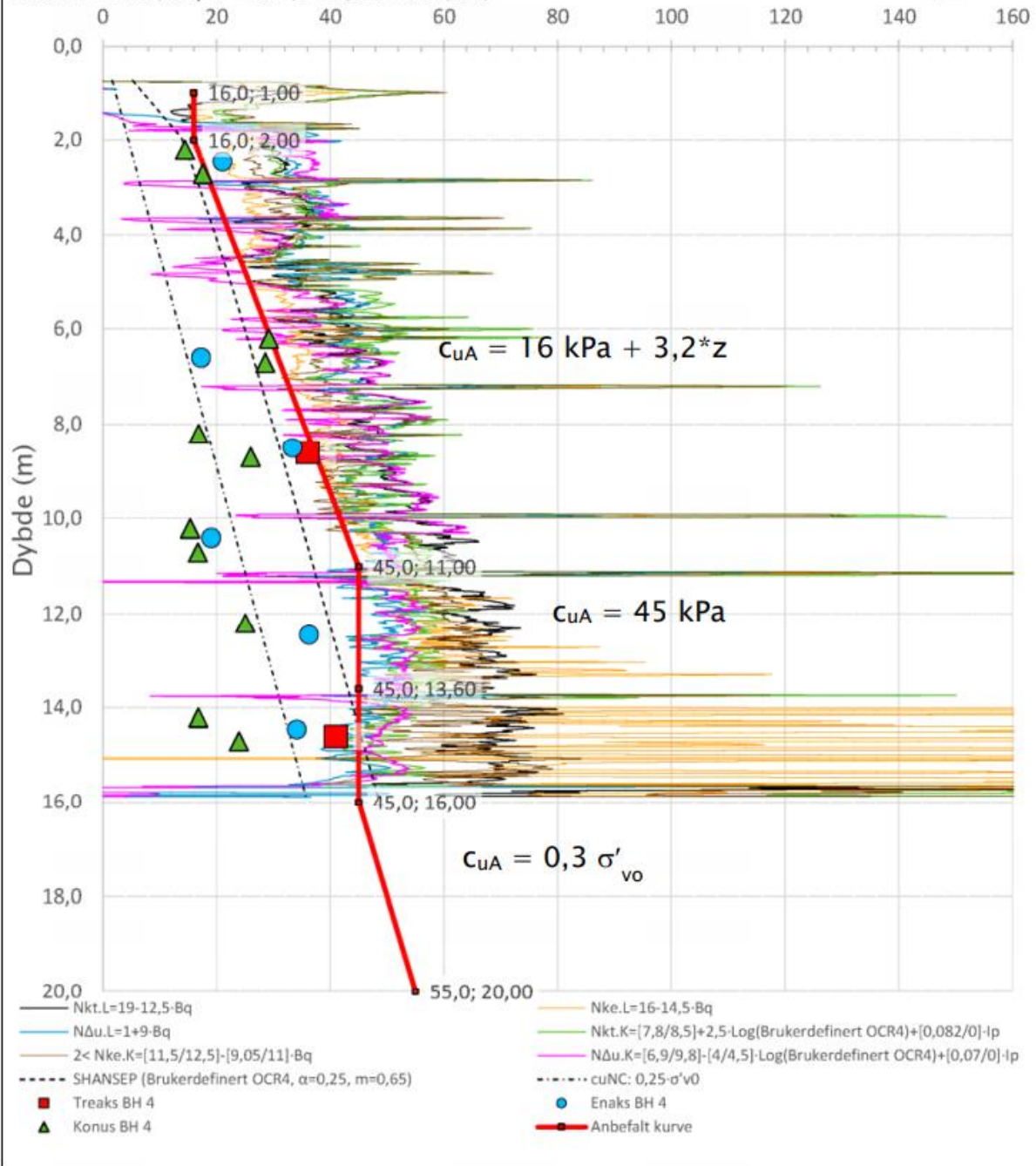
C. Structural measurements

Chart of bedrock dip directions

Quantitative Chart of Processed Strike (Right)
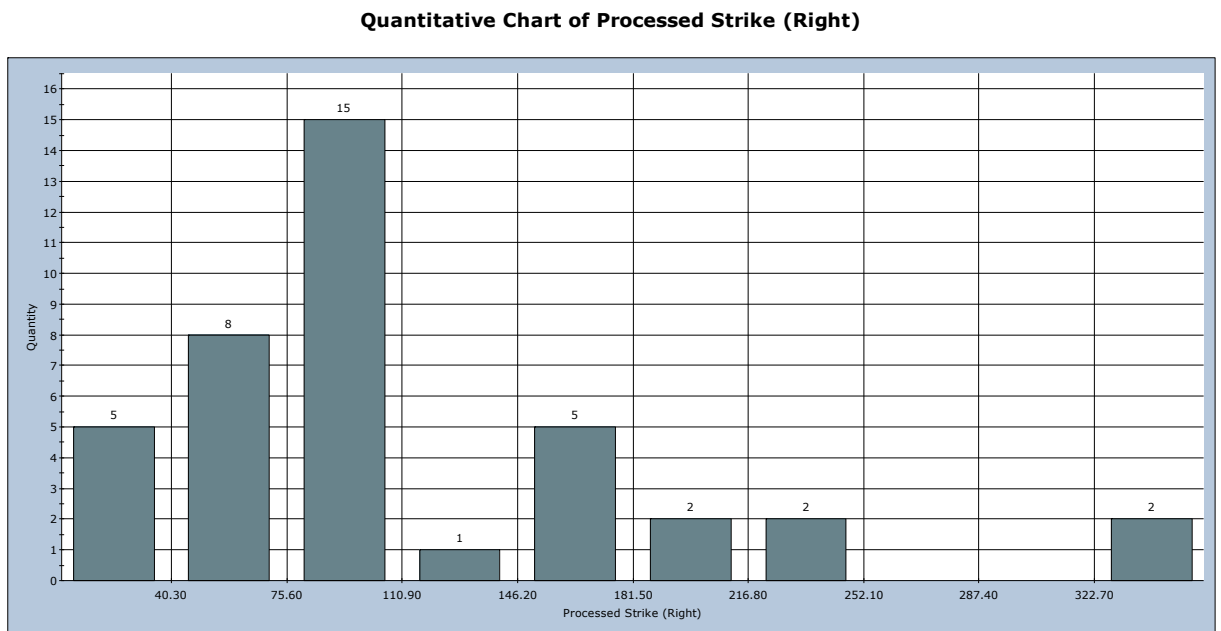
D. Seismic activity

Table of seismic activity registered in Northern Norway in 2020-2021 (source: jordskjelv.no)

Origin time	Lat	Lon	Depth	Mag	Area
2021-03-14 13:45:34	69.875	20.306	10	1.48	NORTHERN NORWAY
2021-01-27 05:04:26	69.196	23.494	10	1.32	NORTHERN NORWAY
2020-10-04 10:55:10	70.244	21.119	2	1.68	NORTHERN NORWAY
2020-09-28 13:59:39	69.198	25.284	30	1.03	NORTHERN NORWAY
2020-07-28 04:04:36	69.625	25.789	13	2.25	NORTHERN NORWAY
2020-06-08 11:18:21	69.443	24.122	0	1.83	NORTHERN NORWAY
2020-05-24 17:21:30	68.899	22.374	0	1.38	FINLAND
2020-04-19 08:44:39	69.874	25.689	13	1.38	NORTHERN NORWAY
2020-03-21 02:47:04	69.347	24.031	10	1.16	NORTHERN NORWAY
2020-01-27 01:04:45	69.312	23.918	22	1.37	NORTHERN NORWAY